EFFECT OF LOW TEMPERATURE CARBURIZATION ON THE MECHANICAL BEHAVIOR OF GASEOUS HYDROGEN-CHARGED 316L STAINLESS STEEL

By

DANQI WANG

Submitted in partial fulfillment of the requirements

For the degree of Master of Science

Thesis Advisor: Dr. Arthur A Heuer

DEPARTMENT OF MATERIAL SCIENCE AND ENGINEERING

CASE WESTERN RESERVE UNIVERSITY

May 2011

CASE WESTERN RESERVE UNIVERSITY

SCHOOL OF GRADUATE STUDIES

We hereby approve the thesis/dissertation of

Danqi Wang

candidate for the Master of Science degree *.

(signed) A H Heuer

(chair of the committee)

J J Lewandowski

G M Michal

(date) 12-17-2010

*We also certify that written approval has been obtained for any proprietary material contained therein.

Dedicated to my beloved parents, Hongping Wang and Qiuyue Shan and my girlfriend Xiaoyan Wang

Contents

List of Tables

Lists of Figures

Acknowledgements

I would like to gratefully acknowledge the guidance and insight of my thesis advisor, Dr. Arthur H Heuer, and the faculty of Case Western Reserve University who collaborated on this project: Dr. John J Lewandowski, Dr. Gary M Michal and Dr. Hal Khan. I would also like thank for Mr. Christopher Tuma for his technical support on mechanical tests, Dr. Avisha Amir for the OIM observation and Dr. David Hovis for laser confocal microscope training. The low temperature carburization process by Swagelok Company and high temperature gaseous hydrogen charging by Sandia National labs are appreciated.

Effect of Low Temperature Carburization on the Mechanical Behavior of Gaseous Hydrogen Charged 316L Stainless Steel

Abstract

By

Danqi Wang

The mechanical behavior of hydrogen-charged 316L stainless steel has been studied in samples containing sharp fatigue-induced pre-cracks, and compared with material that had been carburized at low temperatures following pre-cracking. The hydrogen charging involved exposure to high pressure (~138 MPa) H_2 at 573 K for 24 days.

Non-treated samples either stayed elastic in low stress intensity range or exhibited plasticity at the crack tip at high range; no hydrogen-induced cracking could be observed. On the carburized sample, however, the main crack extended during loading. The variation of crack depth along the crack was verified and reveals that the crack becomes shallower as it approached the newly extended crack tip. The threshold stress intensity factor for the hardened case, K_{th}, is calculated based on this observation. Plastic zone evolution at the crack tip suggests the presence of hydrogen facilitates the motion of dislocations at the room temperature.

1. Introduction

As economy develops, people attach more and more attention to the environment sustainability. Fossil fuel being the cornerstone of the 20th century economy boost brings a non-negligible challenge to human race: huge amount of CO_2 and sulfur are emitted into the air due to the burning of coal, petroleum and natural gas. All kinds of complications came along with this reckless emission, most frequently mentioned is the greenhouse effect. Clean energy has drawn the attention worldwide, as people realized how vulnerable the environment becomes when economy develops.

Clean energy can be defined as the zero or nearly zero emission of greenhouse gases and atmospheric pollutants. Clean energy generally falls into three categories: nuclear, hydrogen and renewable energy (wind, wave, solar and etc.). Each of them has their own advantages. Hydrogen is highly energy efficient, no pollution emitted so it is a promising energy source. On this planet, hydrogen is in the greatest quantities in water. Nowadays most hydrogen is produced by fossil fuel or water electrolyze.

As a substitute for fossil fuel, hydrogen has already involved in some transportation and energy industries, like hybrid vehicle which has quite high MPG (mile per gallon). But problems came with industrialization as well. The common containers of hydrogen in industry and practical applications are made of steel. The deleterious effect of hydrogen on steel is well established. The adsorption, desorption and permeation of hydrogen into alloy container is problematic, yet possible hydrogen-introduced embrittlement make it worse [1, 2, 3]. For the high strength steel, the threshold of hydrogen-induced cracking is inversely related with the yield strength [4]. Austenitic stainless steel is a better choice for hydrogen storage because of its combination of strength and ductility. What is more important is the low diffusivity of hydrogen in austenitic stainless steel which is promising for the low susceptibility to hydrogen. Though better than carbon and high strength steel, it is still not as ideal as expected. Due to the extraordinary effect of carburization on several aspect of mechanical behavior, in this study, the effect of carburization on the mechanical behavior of hydrogen-charged stainless steel was investigated.

2. Background

2.1 Physical properties of 316L stainless steel

316L austenitic stainless steel has a lower carbon content compared to AISI 316 stainless steel. Because of lower carbon content, 316L stainless steel is resistance to sensitization which is due to the grain boundary carbide precipitation. As a trade off, the yield strength and ultimate tensile strength of 316L stainless steel are lower than that of 316 stainless steel.

The chemical compositions of 304, 316 and 316L are listed in Table 2- 1. Nickel is added to stabilize the austenite phase from transforming to martensite phase, but more nickel content also means higher price. The addition of molybdenum can improve the overall corrosion resistance, especially pitting and crevice corrosion in chloride-containing environments. It is also reported that nitrogen can improve the tensile and fatigue properties of austenitic stainless steel at room temperature and 600°C [5].

Table 2- 1 Chemical composition of 304, 316 and 316L stainless steel [6]

	wt%	C	Cr	Ni	Mo	N	Mn	Si	P	S
304	Max	0.08	20	10.5	-	0.1	2.0	0.75	0.045	0.03
	Min	-	18	8	-	-	-	-	-	-
316	Max	0.08	18	14	3	0.1	2	0.75	0.045	0.03
	Min	-	16	10	2	-	0.04	-	-	-
316L	Max	0.03	18	14	3	0.1	2	0.75	0.045	0.03
	Min	-	16	10	2	-	0.04	-	-	-

Due to its excellent corrosion resistance, 316L type stainless steel is a widely used material in industry. Another advantage of 316L stainless steel is its outstanding ductility which enables easy fabrication and machining, but its application is limited by its low strength. Table 2- 2 summarizes some mechanical properties of 304, 316 and 316L stainless steel. 316L stainless steel has a lower yield strength and tensile strength. Considered relatively poor mechanical performance, people tried extensive surface hardening techniques to make it more durable in practical applications. Shot peening is one of the traditional industrial ways. Carburization and nitridation are prevalent currently.

Table 2- 2 Mechanical properties of 304, 316 and 316L stainless steels

Grade	Elastic modulus (GPa)	Tensile strength (MPa)	Yield strength (MPa)	Hardness (Rockwell B)	Elongation (%) min
304	193	520	210	92	45
316	193	515	205	95	40
316L	193	485	170	95	40

2.2 Stress Intensity Factor (K)

Stress intensity factor is used in fracture mechanics to characterize the severity of stress near the crack tip caused by the remote load. If stress intensity is the same at the crack tip in different samples, it means that the stress fields around tips are identical, regardless of the geometries of the cracked samples. The stress intensity factor for general cases is defined as [7]:

$$K = Y\sigma\sqrt{\pi a} \tag{2. 1}$$

where Y is the dimensionless parameter depending on the specimen geometry and crack shape, σ is the applied stress, either remotely or on the crack and a is the total crack length.

There are various kinds of critical stress intensity factors. Fracture stress intensity signifies the highest stress intensity material can tolerate and it is a common way to describe the toughness of the sample. Threshold stress intensity is the critical stress intensity under which no cracking will happen and it is an important parameter for fatigue crack initiation and other cracking behaviors.

In this study, wedge open loading (WOL) specimens were utilized to investigate the effect of carburization on hydrogen-induced cracking behavior. Fig. 2- 1 is the schematic of the WOL sample [8].

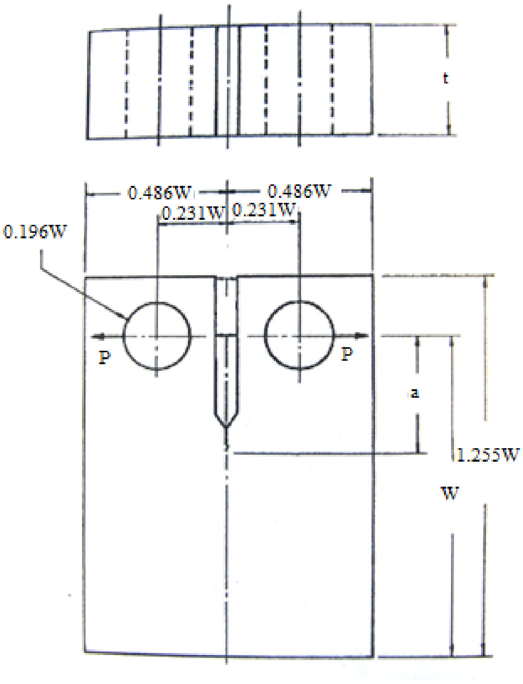

Fig. 2- 1 The dimensions of WOL specimens

The modified stress intensity factor for WOL specimen can be expressed by equation 2. 2 [8]:

$$K = \left(\frac{P}{tW^{\frac{1}{2}}}\right)\left(\frac{(2+\alpha)\left(K_0+K_1\alpha+K_2\alpha^2+K_3\alpha^3+K_4\alpha^4+K_5\alpha^5\right)}{(1-\alpha)^{\frac{3}{2}}}\right) \qquad (2.\,2)$$

where P is the applied load, W is the width, α is the normalized crack length α=a/W, a is the crack length, t is the sample thickness and K_i (i=0, 1, 2, 3, 4, 5) are the stress intensity coefficients that are listed in the table below. This expression is valid for 0.2 ≤a/W≤1.0 and the accuracy is ±0.5%.

Table 2- 3 Stress intensity coefficients for WOL sample

Symbol	K_0	K_1	K_2	K_3	K_4	K_5
Coefficient	0.8072	8.858	-30.23	41.088	-24.15	4.951

2.3 Crack surface displacement modes

Generally, there are three typical crack surface displacement modes: mode Ⅰ- the crack opening mode, mode Ⅱ- the forward shear mode and mode Ⅲ-the parallel shear mode. Mode Ⅰ is the most severe mode among these three, so most toughness and fatigue tests are done in this way. It refers to a tensile stress applied in the Y direction which is normal to the crack surface. The critical fracture stress intensity factor is designated as K_{IC}. Mode Ⅱ is the mode where a shear stress is applied normal to the leading edge of the crack, but in the plane of the crack. Mode Ⅲ is for shearing stress applied parallel to the leading edge of the crack. Figure below shows the sketches of these typical surface displacement modes [7]. Some tests are also done in the condition of mixed modes, like mode Ⅰ/Ⅱ and mode Ⅰ/Ⅲ.

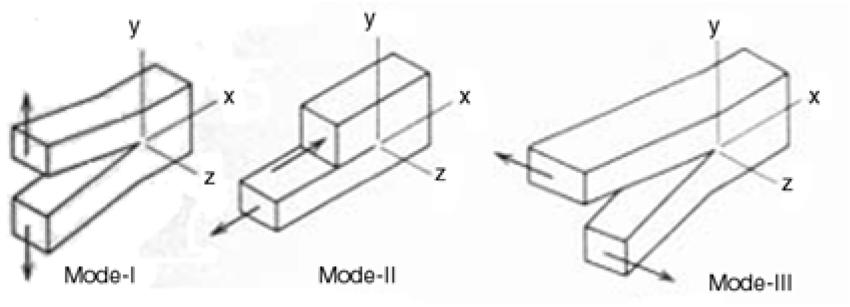

Fig. 2- 2 Schematic of typical crack surface displacement modes

2.4 Plasticity at crack tip

Plasticity is inevitable at the crack tip. Only the plastic zone size differs when different stress intensity achieved at the crack tip. For high strength material, the plastic zone is small and it is relatively large for low strength material. Plastic zone is considered as one way to measure the material resistance against the driving force. Plastic zone is efficient to dissipate the energy i.e. absorb more energy before failure. Many inherent brittle materials, like ceramics, are extremely strong, but brittle and whose plastic zone size is very small.

The plastic zone size is very important for the structural component design. If plastic zone size is small compared with the component, the component tends to behave or fail in brittle way. So material with small plastic zone size, like ceramic or metallic glass, is not a good candidate for large structural applications, like a bridge. Therefore, if plastic zone size is relatively large, then it is beneficial for plastic deformation, which will absorb much more energy before its failure and consequently higher toughness. What is more important is that this kind of failure will not be catastrophic, thus much safer for everyday use.

Plastic zone size can be estimated by Irwin approach [7]:

$$r_p = \frac{1}{2\pi}\left(\frac{K}{\sigma_{ys}}\right)^2 \quad \text{(for plane stress)} \qquad (2.3.1)$$

$$r_p = \frac{1}{6\pi}\left(\frac{K}{\sigma_{ys}}\right)^2 \quad \text{(for plane strain)} \qquad (2.3.2)$$

where r_p is the plastic zone size, and σ_{ys} is the 0.2% offset yield strength, K is the applied stress intensity factor. It can be easily seen that material with high yield strength usually has small plastic zone size compared with low strength material.

Compared with plane stress condition, plane strain condition is more severe. The material in the center is constrained by the surrounding material and thus cannot be freely deformed. The criterion to determine the plane strain condition is: the sample thickness (B) must equal or exceed 2.5 $(K/\sigma_{ys})^2$. High strength material is easier to reach plane strain condition, i. e. thinner material required. In this study, applied K is around 40 MPa√m and the yield strength is 170 MPa which is pretty low. So the approximate critical thickness for plane strain is around 50 mm, which is almost one order of magnitude higher than the sample thickness in this study (6.4 mm). Therefore, the sample configuration used in this study is in plane stress condition and plastic zone size follows the equation 2. 3. 1. For carburization layer, whose strength is around 2000 MPa [9], taken residual stress as yield strength in the case, the calculated thickness required for plane strain condition is 400 μm. This is still way larger than the case thickness, which is usually around 25 μm after a typical carburization process [9]. The whole sample is in plane stress condition no matter if it is carburized or not.

2.5 Residual stress

Residual stress is a stress existing in the bulk material in the absence of any external stress applied. It could be either tensile or compressive. It is mainly introduced by plastic deformation . Generally, area previously plastically deformed by tension will have residual compressive stress when external stress is removed. Likewise, region deformed by compression usually exhibits residual tension stress when free of loading. This can be visualized as plastic deformed area prevents the adjacent region to recover fully and elastically so residual stress is introduced. In the carburization case, high local plastic strain is present due to the misfit between the interstitial carbon atoms and interstitial sites. The high carbon content brought in by the process also accounts for the high local plastic strain. The carbon atoms expand the lattice plastically and the core material withholds its free expansion. Therefore the residual compressive stress is introduced in the surface by supersaturated carbon atoms.

A favorable compressive residual stress is regarded as one of the best ways to improve the material performance. The stress intensity from residual stress will offset some driving force stress intensity, mitigating the effective stress intensity at a crack tip. This beneficial effect from residual stress can be simplified by the principle of superposition [10] (details refer to section 2.7.1).

$$K_{eff} = K_{app} + K_{res} \tag{2.4}$$

where K_{app} is the applied stress intensity and K_{res} is the stress intensity contributed by residual stress. K_{res} is negative when residual stress is compressive. It is straightforward that when the effective stress intensity is reduced better performance can be expected.

2.6 Crack tip opening displacement (CTOD)

The initial observation of Wells [10] led to the concept of crack tip opening displacement (δ). In his experiments, some materials were too tough to be described by linear elastic fracture mechanics (LEFM). The plasticity at the crack tip dominated the test. The crack faces moved apart prior to the fracture and plastic deformation blunted an initially sharp crack. The degree of crack blunting increases proportionally to the toughness of the material.

Nowadays, CTOD is another way to characterize the toughness of the materials. The definition of CTOD is that an initially sharp crack blunts by plastic deformation, resulting in a finite displacement (δ) at the original crack tip as illustrated by Fig. 2- 3.

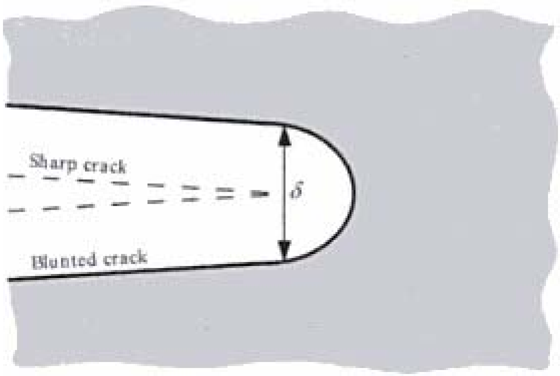

Fig. 2- 3 Schematic of CTOD

In the regime of small-scale-yielding, adopted Irwin's [10] postulation of crack-tip plasticity, the CTOD can be estimated by solving the displacement at the physical crack tip, assuming an effective crack length of $a+r_y$, where r_y is the Irwin plastic zone correction, expressed as equation 2. 3. The displacement u_y at the effective crack tip based on Irwin's postulation can be expressed as

$$u_y = \frac{4}{E'} K_I \sqrt{\frac{r_y}{2\pi}} \qquad (2.5.1)$$

where E’ is the effective Young’s modulus. E’ equals to E under the plane stress condition and to E/(1-ν^2) under plane strain condition, where ν is the Poisson ratio. Then the expression for CTOD can be finalized as equation 2. 5. 2.

$$\delta = 2u_y = \frac{4}{\pi} \frac{K_I^2}{\sigma_{ys} E'} \qquad (2.5.2)$$

Further development of the CTOD theory is the strip-yield model, which assumes plane stress condition and a non-hardening material. The actual relationship between CTOD and K depends on stress state and strain hardening. The more general form for this relationship can be displayed as equation 2. 6. 1

$$\delta = \frac{4}{\pi} \frac{K_I^2}{m \sigma_{ys} E} \qquad (2.6.1)$$

where m is a dimensionless constant that approximately 1.0 for plane stress condition and 2.0 for plane strain condition. As for the samples employed in this study, equation 2. 6. 2 is an appropriate expression for CTOD and K relationship.

$$\delta = \frac{4}{\pi} \frac{K_I^2}{\sigma_{ys} E} \qquad (2.6.2)$$

Due to the practical difficulty to measure CTOD value directly, the hinge model is adopted to acquire the CTOD value. The CTOD can be calculated by assuming that the two sample halves are rigid and rotate about a hinge point, as illustrated in Fig. 2- 4.

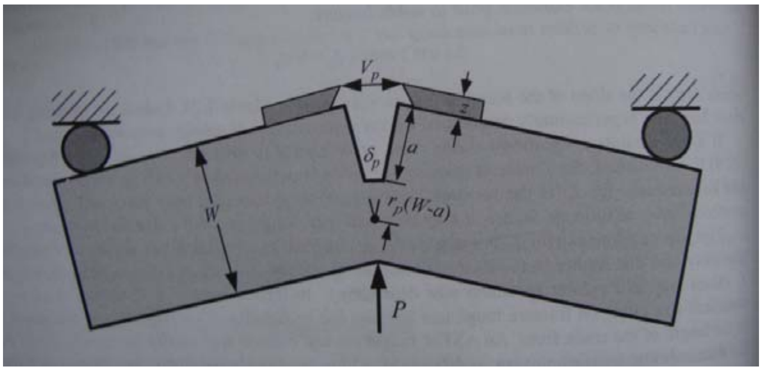

Fig. 2- 4 Hinge model for plastic displacements in a single edge bending specimen

From the geometric relationship between the hinge point, crack tip and front face, equation 2. 7. 1 can be established:

$$\frac{\delta_p}{r_p(w-a)} = \frac{V_p}{r_p(W-a)+a+z} \qquad (2.7.1)$$

where V_p is the displacement at front face, z is the thickness of the wedge. r_p is the rotational factor, which defines the location of the hinge point. Rearranging the equation 2. 7. 1, equation 2. 7. 2 can be obtained

$$\delta_p = \frac{r_p(W-a)\,V_p}{(r_p(W-a)+a+z)} \qquad (2.7.2)$$

The polynomial expression for the axis of rotation in the range $0.2 \le a/W \le 1.0$ is given by [11]

$$\frac{x_0}{W} = 0.408778 - 1.52443\left(\frac{a}{W}\right) + 9.04028\left(\frac{a}{W}\right)^2 - 17.3354\left(\frac{a}{W}\right)^3 + 15.9708\left(\frac{a}{W}\right)^4 - 5.56415 \qquad (2.8)$$

This hinge model is not accurate when displacement is primarily elastic, but it works well when plastic deformation dominates. The total displacement is divided into two parts: one is the elastic part and the other is the plastic one. In a standard load-displacement curve, the amount of these two parts can be actually measured from the curve. Fig. 2- 5 exhibits the principles of this idea.

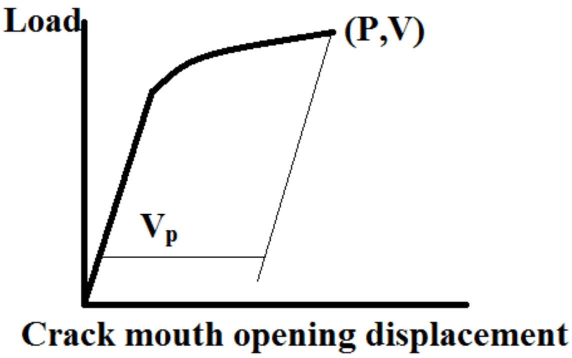

Fig. 2- 5 Load-COD curve

In the loading portion, the plasticity follows the initial elastic linear part. By assuming the crack does not propagate, linear portion of the curve should be parallel to the unloading part. The distance between the loading and unloading portions defines the plastic COD. In this study, plastic COD is taken from the COD value of the unloading line at 100 lb, because the clip gauge is zeroed at the beginning of the test at 100 lb. Equations 2. 6. 2 and 2. 7. 2 considered, calculation of CTOD can be completed now as:

$$\delta_{total} = \delta_{el}+\delta_{pl} = \frac{4}{\pi}\frac{K_I^2}{\sigma_{ys}E} + \frac{r_p(W-a)\,V_p}{(r_p(W-a)\,+a+z)} \qquad (2.\,9)$$

One thing should be noted is that, for linear elastic conditions ($V_p \approx 0$), equation 2. 9 will simplify to equation 2. 6. 2 that applies to small-scale yielding result; otherwise, when $V \approx V_p$, the hinge model dominates as equation 2. 7. 2.

2.7 Weight function

The concept of weight function, or alternatively influence function, or Green's function, was first introduced by Bueckner [12] based on analytical function representation of elastic fields for isotropic materials. The stress intensity factor due to an arbitrary set of applied loads can be obtained by integrating over crack length a product of these loads with the weight function m(α, x) of the cracked body:

$$K=\sqrt{W}\int_0^a \sigma(x)m(\alpha,x)dx \qquad (2.\,10)$$

where α and x are the non-dimensional crack length and coordinate, respectively, defined by $\alpha=a/W$ and $x=X/W$. Rice [13] on the other hand derived the same equation and demonstrated that the weight function is a universal function for a cracked body of any given geometry and composition, regardless of the detailed way in which the body is loaded.

2.7.1 Superposition principle

Although stress intensity factors for any load case can be determined by using the generalized weight function approach (details in [14]), the practical application of these generalized equations often encounter difficulties. This is due to the application of generalized equation requires not only the knowledge of the reference stress intensity factor $K^{(1)}(A)$, but also other quantities that are not easily determined like boundary conditions. The limitations of these generalized equations can be overcome by using the superposition principle of linear elastic fracture mechanics. The essence of superposition principles is to transform the generalized equation which requires complete elastic solutions to some equivalent expressions which requires much less knowledge of the reference crack problem.

Consider a crack-free body which is subjected to prescribed tractions T_i over the boundary C_T and to prescribed displacements U_i over the boundary C_U; in addition it may contain a self-equilibrating internal stress system σ_{int} sketched in Fig. 2- 6 (a). On the line MN, there will be a stress distribution $\sigma(X)$ resulting from the loads on the boundary and internal stress systems. If a crack is now introduced along MN, and at the same time a traction $-\sigma(X)$ is applied on its faces, as shown in (b), it will remain perfectly closed with the stress intensity factor $K_{(b)}=0$. The stress distribution in the entire body prior to the introduction of the crack is not disturbed. Therefore, the cases in (a) and (b) are exactly the same. Since the body is within the linear elastic regime, the case (b) can be decomposed into two cases presented in Fig. 2- 6 (c) and (d). In all the cases, the boundaries C_T and C_U are kept the same, but the tractions T_i on C_T and displacements U_i on C_U are different: in (d) both T_i and U_i are zero over their respective boundaries. Because $K_{(c)}+K_{(d)}=K_{(b)}=0$, so $K_{(c)}=-K_{(d)}$. Finally, if the sign of the crack face traction is reverse, (e), $K_{(c)}=K_{(d)}$ can be achieved.

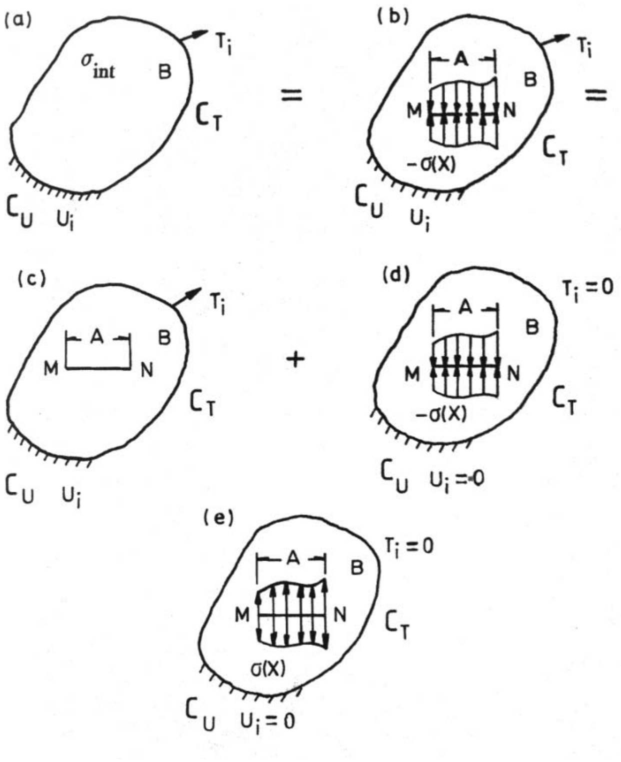

Fig. 2- 6 Superposition principle for stress intensity factors in LEFM

2.7.2 Simple-form generalized weight function

By using the superposition principles, the generalized weigh function equation can be significantly simplified for mixed boundary condition. With the non-dimensional quantities: $x=X/W$, $\alpha=a/W$, $u_r(\alpha, x)=U_r(a, X)/W$, and $f_r(a)=K_r(a)/(\sigma\sqrt{\pi aW})$, equation (2. 11) can be obtained,

$$K=f\sigma\sqrt{(\pi aW)},\ f=\int_0^a \frac{\sigma(x)}{\sigma}\frac{m(\alpha,x)}{\sqrt{\pi a}}dx \qquad (2.\ 11)$$

where m(α, x) is the weight function, shown in equation (2. 12)

$$m(\alpha, x) = \frac{E'}{f_r(\alpha)\sigma\sqrt{\pi a}} \frac{\partial u_r(\alpha, x)}{\partial \alpha} \qquad (2.12)$$

where E’ is the effective modulus as previously stated in equation 2. 5. 1. The weight function m(α, x) is determined from a reference load case whose geometry, including the boundary composition of C_T and C_U , is the same as the new load case for which the stress intensity factor is to be determined. The strength of the weight function method is the separation of the two factors on which the stress intensity factor depends, namely, the crack line stress σ(x) and the cracked geometry. Once determined, the weight function can be used unlimitedly.

2.7.3 Weight function for WOL

For specific sample geometry, knowledge of the reference stress intensity factor solution and some crack opening conditions allow a number of coefficients to be determined. For WOL sample, displacements at certain locations can be known [11]. WOL sample is single-edged plate and its L/W is 0.96 as shown in Fig. 2- 1. The weight function for a plate with L/W≥1 is given in equation (2. 13) [14],

$$h = \sqrt{2/\pi a}\, \frac{1}{\sqrt{1-\rho}} \left[1 + \sum_{\nu\mu} \frac{A_{\nu\mu}\alpha^{\mu}}{(1-\alpha)^{\frac{3}{2}}} (1-\rho)^{\nu+1}\right] \qquad (2.13)$$

where $\rho=x/a$, $A_{\nu\mu}$ are the fitting coefficients listed below in Table 2- 4. Since L/W in WOL specimen is close enough to one, so in this study it is treated as unity. With the coefficients in the Table 2- 4 and the stress on the crack line, the stress intensity factor in WOL can be readily calculated.

Table 2- 4 Weight function fitting coefficient for single-edged plate

ν/μ	0	1	2	3	4
0	2.673	-8.604	20.621	-14.635	0.477
1	-3.557	24.9726	-53.398	50.707	-11.837
2	1.23	-8.411	16.957	-12.157	-0.94
3	-0.157	0.954	-1.284	-0.393	1.655

2.7.4 Application of weight function

Wight function was applied to the center cracked rectangular specimen [15], detail configurations shown in Fig. 2- 7 (a). To simplify the calculation of stress intensity contributed from residual stress, K_{res}, a rectangular distribution is used to approximate the actual residual stress as illustrated by dash line in (b). Equation used to calculate K_{res} is derived for center cracked rectangular specimen specifically.

$$K_{res}=\int_{-a}^{a}\sigma_{res}(x)\left[\frac{2\sin\frac{\pi(a+x)}{W}}{W\sin\frac{2\pi a}{W}\sin\frac{\pi(a-x)}{W}}\right]^{1/2} \qquad (2.14)$$

where a is the crack half-length, W is plate width, x is the distance from the plate centerline, and σ_{res} is the residual stress introduced by welding. Consequently, the variation of K_{res} with x can be calculated and shown in (c). The result was further utilized to predict the crack growth behavior of the sample.

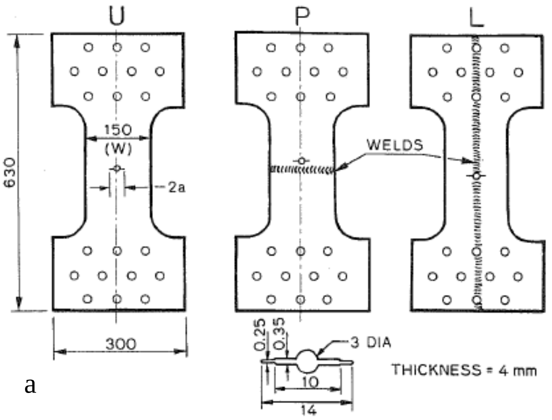

a

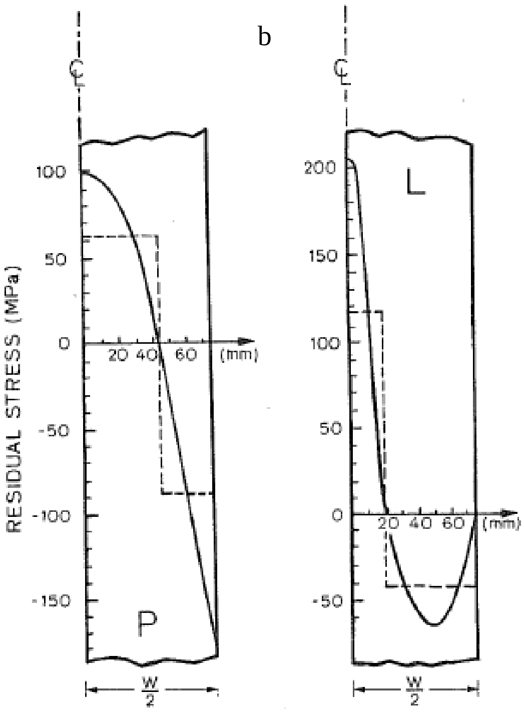

b

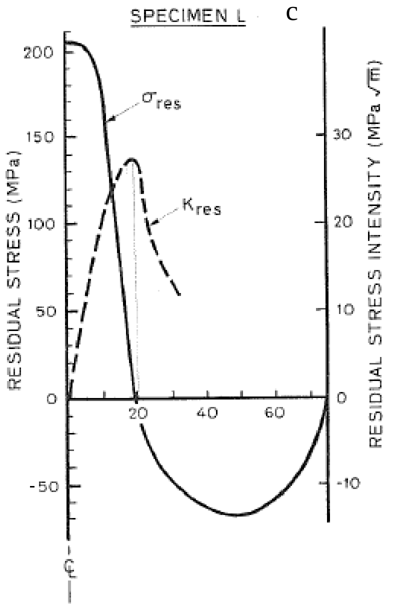

Fig. 2- 7 Weight function applied to residual stress intensity factor calculation. (a) center-cracked rectangular specimen dimension, (b) initial residual stress normal to the plane of crack, (c) residual stress and residual stress intensity distribution for L-type specimens.

Another analytical model of weight function applied to the residual stress in the case-hardened steel is discussed by Kim [16]. In his study, a single-edge-notched specimen was used and K_{res} was calculated according to equation 2. 15,

$$K_I = \int_0^a \frac{2\sigma_r dc}{\sqrt{\pi a}} F\left(\frac{c}{a}, \frac{a}{W}\right) = \int_0^1 2\sqrt{\frac{a}{\pi}}\sigma_r F\left(\frac{c}{a}, \frac{a}{W}\right) d\left(\frac{c}{a}\right) \tag{2. 15}$$

where W, a, c and σ_r represent specimen width, crack length, distance from the specimen face on the crack side to the crack tip and residual stress, respectively. The stress intensity from residual stress is calculated consequently. Following analysis on the cracking threshold ΔK_{th} substantiates the beneficial influence of residual compressive residual stress within the case. In Fig. 2- 8, two situations of residual stress were postulated as displayed at the upper left corner. The effective stress intensity was further calculated by superposition principle as shown in equation 2. 4. In this study, similar idea is adopted to calculate the effective stress intensity.

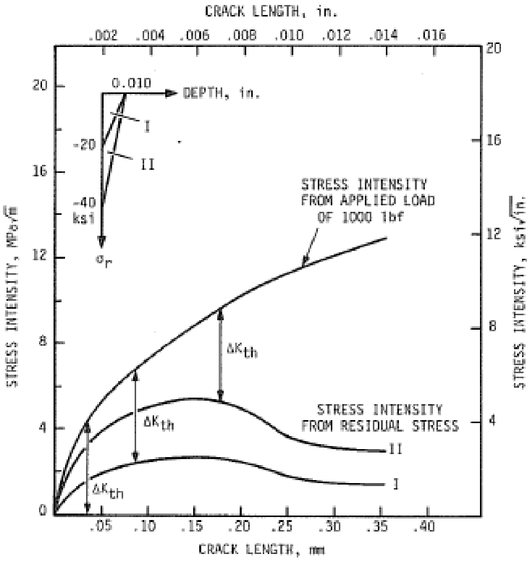

Fig. 2- 8 Stress intensity profiles due to applied load and two residual stress profiles

2.8 Low temperature carburization

The carburization process is comprised of two activation steps and two carburization steps as manifested in Fig. 2- 9 [17]. The purpose of an activation step is to remove the chromium oxide passive film on the very surface. This is accomplished by HCl gas at 250 °C. After activation, 3 hour carburization was followed at 470 °C. The carburization species were CO, H_2 and N_2. Then a second 3 hour activation step was followed in case of repassivation of stainless steel during first carburization step. Final carburization step was a long process to achieve final carbon content.

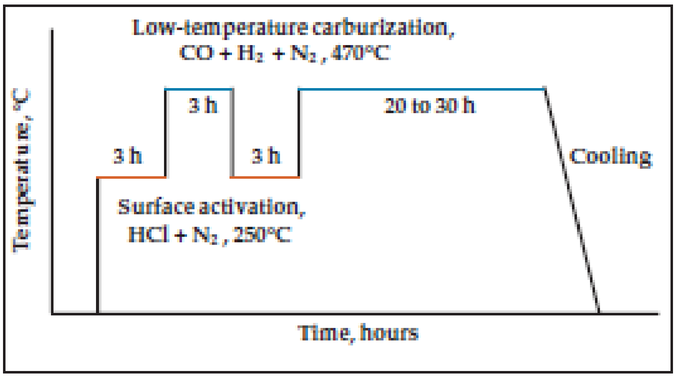

Fig. 2- 9 Schematic of a typical low temperature carburization treatment

In a traditional carburization process, the achieved carbon concentration in 316L is limited to small content attributed to the carbide formation. In low temperature carburization process, the temperature (~470 °C) is only around half of that in traditional process (>900 °C), which effectively prohibits carbide formation by paraequilibrium.

Therefore, after this carburization process, an extremely high carbon content can be achieved (~15 at%). The surface hardness also proliferates. The combined profile of HV hardness and carbon concentration is shown in Fig. 2- 10 [9]. On the very surface, the carbon content is up to 15 at% and falls gradually to zero as moves into the core. The case extends around 25 um, which can be verified by metallography as well (Fig. 2- 11 [18]). The hardness is a function of carbon content and so its profile is similar to that of carbon. The residual stress as a function of depth is calculated by XRD results that are shown in Fig. 2- 12 (a) [19]. The calculation is done based on the lattice expansion and corresponding peak shift observed in the XRD pattern. The residual compressive stress is more than 2 GPa after the treatment [9], as illustrated in Fig. 2- 12 (b). The merit of this process is that though the hardness soars above 1200 HV, it does not sacrifice the ductility much and corrosion resistance. In this case, the corrosion resistance of 316L after carburization is even better than that of non-treated sample [20].

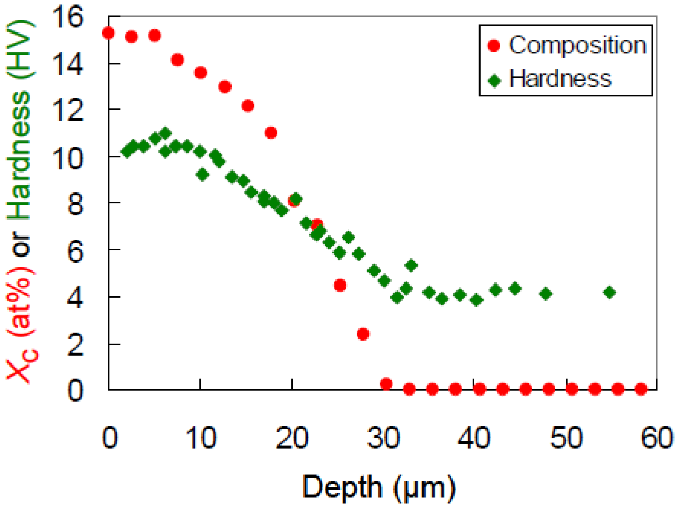

Fig. 2- 10 Vicker’s hardness and carbon concentration depth profiles

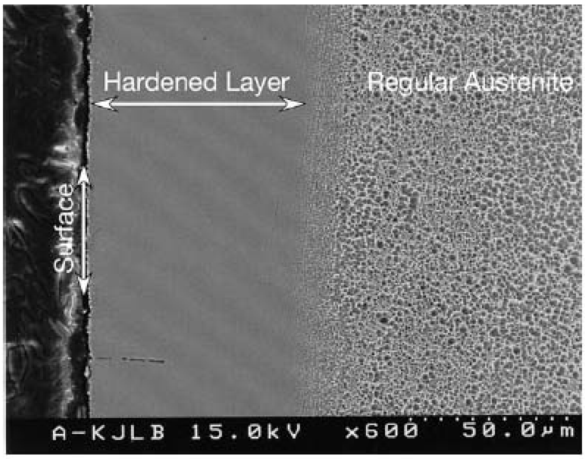

Fig. 2- 11 Cross-section SEM image of a low-temperature carburized 316 austenitic stainless steel specimen

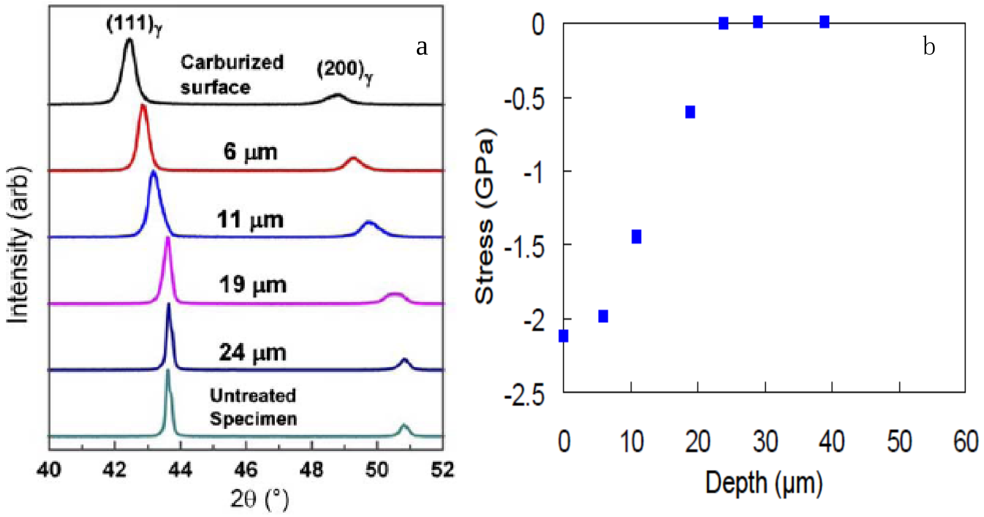

Fig. 2- 12 (a) XRD scans for a carburized specimen, carburized specimen with 6, 11, 19 and 24 μm of the case removed by electro-polishing and an untreated sample and (b) residual stress profile of carburized 316L stainless steel.

The stress-strain curves of 316L in Fig. 2- 13 indicate there is no loss of ductility. Three curves are non-treated (NT), carburization treated (C) and heat treated (HT) respectively [9]. No distinguishable difference in ductility may be owing to the fact that the case depth is only 25 um, which is less than 1% area fraction of tested material. But by comparing these three curves, little increases in yield strength and ultimate tensile strength (UTS) are observed in CT and HT samples. It can be because of the heat treatment during the process.

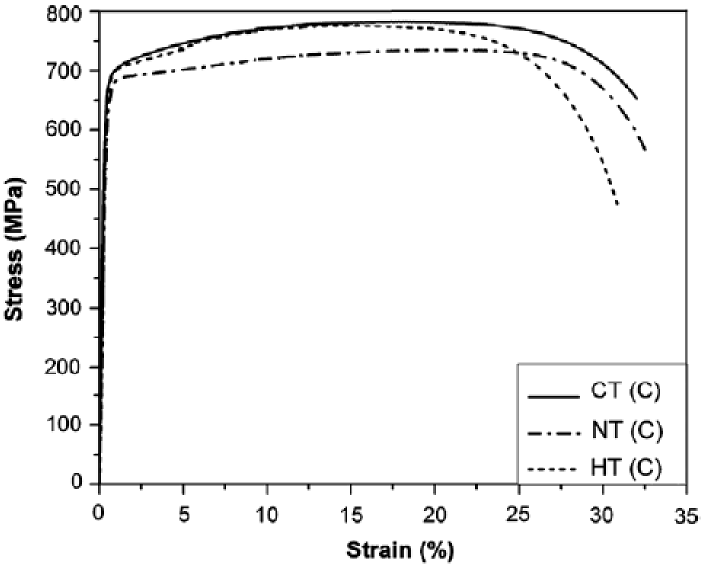

Fig. 2- 13 Stress-strain plot of one CT, NT and HT 316 stainless steel samples

The more practical interest of carburization is the improved fatigue and wear properties. The high cycle fatigue limit of 316L increases from 200 MPa to 325 MPa after one cycle of carburization process [9]. In Fig. 2- 14, fatigue results of various times carburization are also available. However, there is no further improvement of fatigue limit after first time carburization.

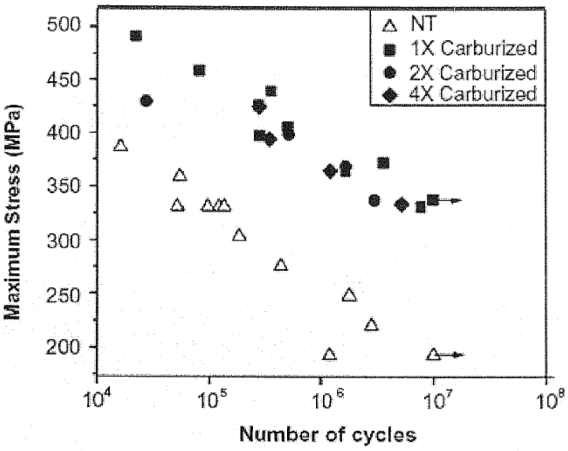

Fig. 2- 14 S-N curves for NT and various times low-temperature carburized 316L stainless steel

The fatigue crack growth rate (FCGR) behavior of 316L was also taken care of. The threshold of stress intensity factor was summarized in Table 2- 5 [21]. The improvement of threshold is more than 20%, which results from the heat treatment and carburized case. Not only the threshold increases after carburization, the FCGR of carburized sample is also several factors lower than that of non-treated and heat-treated samples in the lower stress intensity range. They converge at higher stress intensity end, as displayed in Fig. 2- 15.

Table 2- 5 Fatigue crack growth threshold of NT, HT and CT 316L stainless steel and its improvements

	NT	HT	CT
ΔK_{th} (MPa√m)	8.1±0.3	9.1±0.3	10.0±0.3
ΔK_{th} improvement (%)	0	12	23

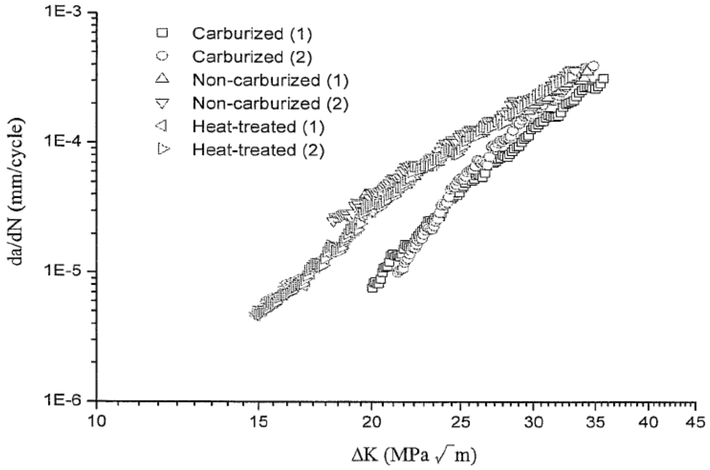

Fig. 2- 15 Variation of fatigue crack growth rate (da/dN) with stress intensity factor range (ΔK)

There is also a significant improvement of wear property after carburization. The difference in the wear rate is nearly an order of magnitude between NT and CT samples under three sliding conditions displayed in Fig. 2- 16 [22].

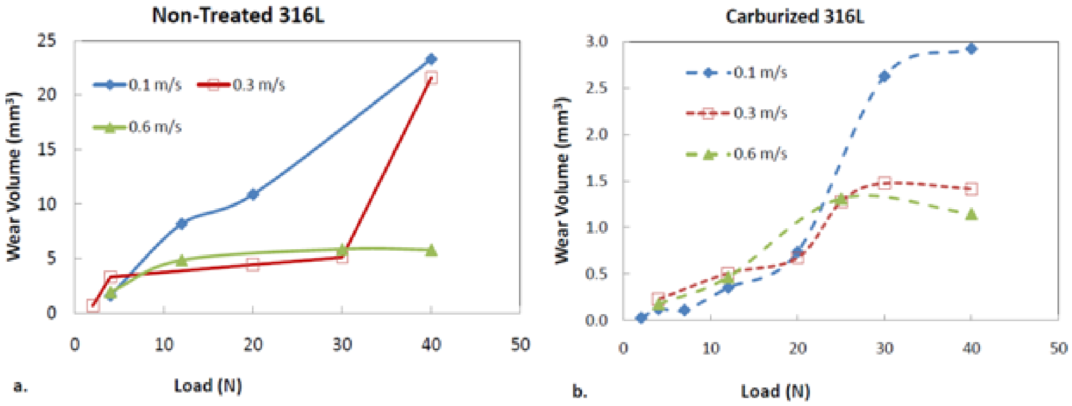

Fig. 2- 16 Pin-on-disk test results comparing (a) non-treated 316L stainless steel and (b) carburized 316L stainless steel

2.9 Hydrogen embrittlement

2.9.1 Hydrogen embrittlement (HE) characterization

Extensive experiments have been done on the hydrogen effect on stainless steel. Hydrogen embrittlement severity is usually characterized by the reduction area (RA) of the tensile specimens, the higher the better. In some cases, relative reduction area (RRA) is used, which is defined as reduction area of hydrogen-affected sample divided by reduction area of hydrogen free sample [23]. If RRA equals to unity, it means hydrogen cannot degrade sample property. Elongation is also used to characterize the HE [24, 25]. The reason to use reduction area or elongation is that yield strength is not much affected by hydrogen and the same to UTS. This is illustrated in Fig. 2-17 (a) and (b) [26]. In (a), it can be seen that under four different charging conditions the UTS are nearly the same. Actually, yield strength increases a little bit because of solid solution strengthening mechanism as more hydrogen atoms enter. However, the normal strain drops significantly from 0.34 in air (free of hydrogen) to lower than 0.1. The corresponding RA of these total five conditions is plotted in (b). RA for in air test nearly approaches unity, which suggests this 23Cr-5Ni-3Mo duplex stainless steel could be really ductile. For most severe condition, RA is around 0.1, which is almost an order of magnitude lower than RA in air. Therefore from this point of view, RA is more sensitive and thus a better way to evaluate the degree of hydrogen embrittlement.

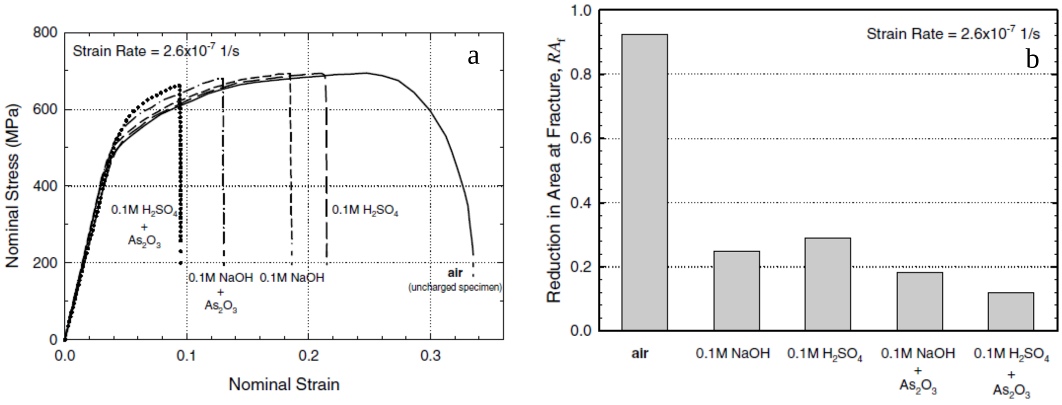

Fig. 2- 17 Stress-strain behavior of 23Cr-5Ni-3Mo duplex stainless steel specimens cathodic charged at 20 mA/cm^2, pre-charging for two weeks. (a) stress-strain in air and charged in various solutions, (b) reduction in area at fracture

A common way to carry out the hydrogen affected tensile test is slow strain rate test (SSRT), as tests in Fig. 2- 17 above are done at the strain rate 2.6×10^{-7}/s. The effect of strain rate has been studied elsewhere as well [24, 27]. Slower strain rate often gives a lower strain to failure. But the slowest strain rate does not necessarily correspond to the lowest strain to fracture as shown in Table 2- 6. There is some most damaging strain rate for the test. This is related to the transportation and saturation of hydrogen. Generally, there are two hydrogen transportation models in steel, lattice diffusion and dislocation sweeping diffusion. Though evidences for each of the theory are available, the lattice diffusion model is more favorable [29, 30]. In lattice diffusion model, the diffusion driving force is the stress state and hydrogen concentration gradient. Many experimental results support lattice diffusion model. Hydrogen embrittlement test carried out under mode Ⅲ shows little embrittlement whereas severe embrittlement occurs in mode Ⅰ test, implying stress-state (triaxial stress) plays a more important role than dislocation [31]. In another study, the hydrogen affected area (from fractographic study) exceeds the area where dislocation is mobile, indicating lattice diffusion is dominant [30]. In Fig. 2- 17, though yield strength does not affected much by solute hydrogen, slight increase of yield strength in steel is still distinguishable. This solute hardening mechanism suggests hydrogen is more effective at dragging the dislocation, instead of move with dislocations. Though hydrogen dislocation diffusion is real, it may not be a critical step for hydrogen embrittlement. Instead, stress state, hydrogen content and susceptible phase are necessary for hydrogen embrittlement taking place [30, 32].

Table 2- 6 Result of Hydrogen embrittlement during slow strain rate test of AISI 316L [28]

AISI 316L	$\dot{\varepsilon}=7\times10^{-7}\ s^{-1}$	$\dot{\varepsilon}=1\times10^{-6}\ s^{-1}$	$\dot{\varepsilon}=5\times10^{-6}\ s^{-1}$
Strain to fracture	20%	13%	15%
Test duration (h)	80	22	9
Average crack propagation rate ($10^{-10}ms^{-1}$)	5	15	28
Crack depth (10^{-6} m)	140	120	90
Depth theoretically covered by H_2 (SSRT duration +24h precharging) (10^{-6}m)	50	30	27

Typical fracture mode of SSRT is shown below (Fig. 2- 18 (a)). During cathodic charging, the outer shell (periphery) usually exhibits brittle fracture mode [24, 28]. However, in the center where in the presence of lower or no hydrogen, it is ductile mode, which is microvoid coalescence (MVC). The other areas are still failed by MVC mode but the dimple sizes decrease from center to outer area that beneath the brittle fracture ring. A fractography picture (Fig. 2- 18 (b)) enunciates this very well that brittle fracture dominates the outer surface while inner area behaves dimple failure. Some brittle secondary cracking was also reported in the hydrogen affected zone [28].

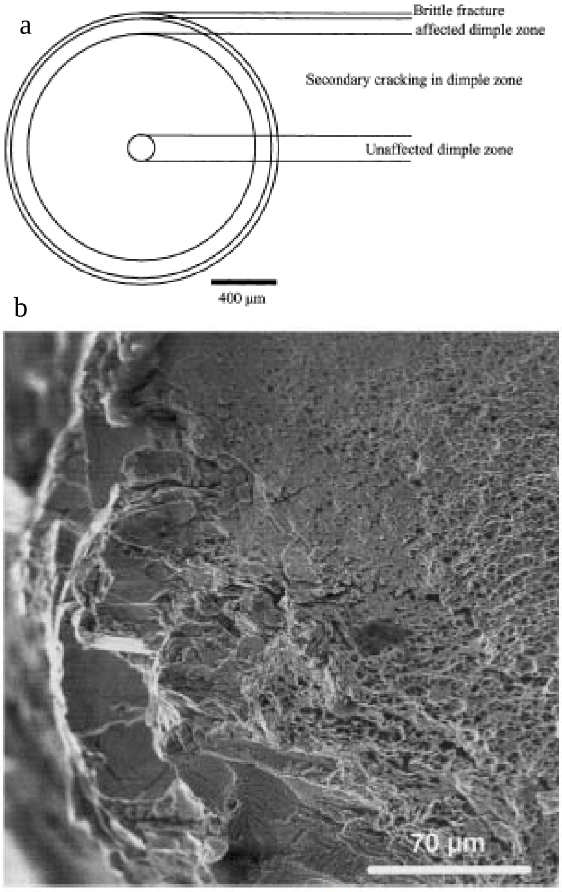

Fig. 2- 18 (a) Schematic of typical fracture surface obtained after HE SSRT, cathodic charging on type 316L, (b) transition between brittle and ductile fractrure. Cathodic charging during SSRT, cathodic polarization 100 mA/cm^2, strain rate 10^{-6}/s, strain to fracture 13%.

2.9.2 Hydrogen charging method

There are two conventional ways employed to introduce hydrogen into material. One is cathodic charging and the other one is gaseous hydrogen charging. These two methods per se stem from the practical applications. Cathodic charging is more like the situation of the pipeline which is protected by cathodic current. The by-product of this process is hydrogen atoms which will make pipeline more susceptible to cracking. Similar situation happens in fuel cell. High pressure gaseous hydrogen charging is more related to the hydrogen storage. Though hydrogen is much easier to store compared with electricity, the hydrogen permeation and embrittlement of container are still very annoying.

Cathodic charging is carried out in the solution, which typically includes hydrogen source and recombination antidote. There are various kinds of hydrogen sources, like sulphuric acid (H_2SO_4), sodium hydroxide (NaOH), magnesium chloride ($MgCl_2$) and et al [33]. Sodium arsenite ($NaAsO_2$) is a common recombination antidote, which inhibits the hydrogen atoms from recombining to molecular and maximizes the hydrogen atom concentration. So with sodium arsenite, the embrittlement effect is outstanding. As in Fig. 2- 17, sample tested with the presence of sodium arsenite fails at a much lower strain [26, 34]. During the charging process, certain cathodic potential is applied and a constant current is maintained. Different cathodic charging conditions [33] will of course achieve different hydrogen concentration at the end of the process. The cathodic charging is perceived as the most severe charging due to the high local stress, which results from large hydrogen atom concentration gradient on the very surface. This large concentration gradient introduced by cathodic charging makes it difficult to achieve a homogeneous hydrogen distribution in material.

Gaseous charging is usually under high temperature (>573 K) in order to facilitate the dissociation of the hydrogen molecular in the first place. In contrast with large hydrogen concentration gradient formed during cathodic charging, gaseous charging at high temperature is expected to lead to a more uniform concentration in the samples. In this study, in order to obtain hydrogen saturated sample through the whole thickness, hydrogen charging process is carried out in 138 MPa gaseous hydrogen at 573 K for 24 days [35].

Phase transformation nearly always accompanies with hydrogen charging process of austenitic stainless steel. But the content and the final present phase depend on the stability of the stainless steel. Extra peaks usually show up in the XRD patterns during charging process. γ* and ε are common phases, where γ* is the expanded austenite and ε is hcp martensite [36]. γ* phase is called expanded γ phase (~5% greater) due to the solid solution of hydrogen [37]. γ* phase is ferromagnetic with Curie temperature below 273K [38]. ε phase is hcp martensite. The combination of hydrogen itself and stress arose from hydrogen gradient facilitates the formation of ε phase [37]. The mount of ε phase increases with increasing charging time [38]. During the charging process, XRD peak broadening is observed, which is due to the nonuniform hydrogen distribution [36]. It is stated critical charging conditions is required for phase transformation and surface cracking in 304 stainless steel [39]. Concomitant presence of a high hydrogen concentration and stress is required to initiate the phase transformation. So sufficient time and charging current density are needed to achieve critical hydrogen concentration and stress as driving force for the transformation.

During aging, outgassing happens. γ* peak converges with γ [36]. Amount of ε phase reduces, while α’ appears in 304 unstable stainless steel. However, in more stable 310 stainless steel, during the aging, the ε phase fully reverses to γ phase, as shown in Fig. 2- 19 below [38]. There is even no phase transformation in the high pressure charging process for 310 stainless steel. Whereas, ε phase appears in 304 stainless steel under the same gaseous charging condition [40]. This is alluding the cathodic charging is actually more severe than high pressure gaseous charging.

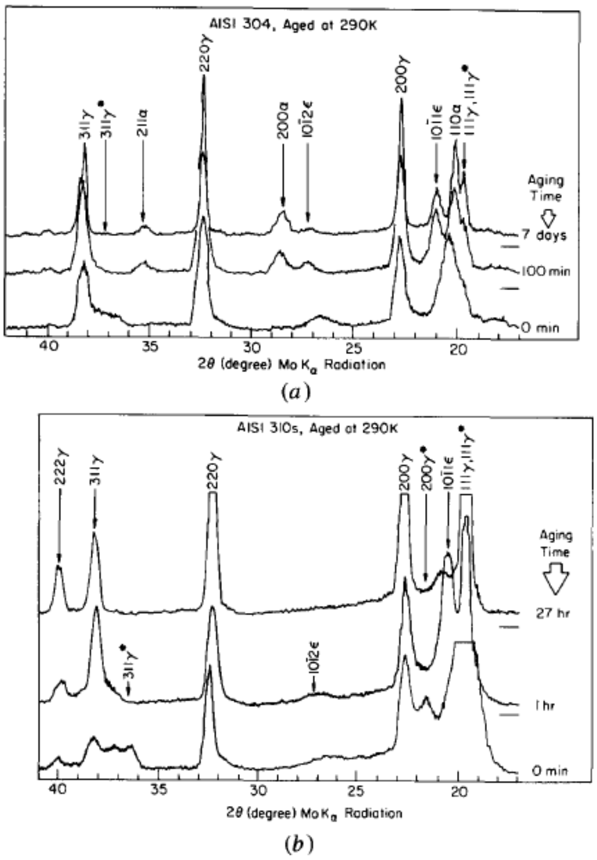

Fig. 2- 19 XRD patterns taken at 200 K after aging at 290 K for the indicated time. (a) AISI 304, charged at 298 K, 20 h, 0.5 A/cm^2. Mo K radiation. (b)310 HP charged at 298 K, 12 h, 1 A/cm^2. Mo K radiation.

Surface cracks usually first appear at aging stage. As hydrogen leaves the surface, the compressive stress formed during charging turns into tensile stress on the surface. This high tensile stress can either facilitate the formation of surface crack and or promote the phase transformation from ε-->α’. But it is still not clear whether the ε-->α’ is the consequence or cause of surface cracking. But in Yang’s study, the observation is if no martensite transformation detected then there is no surface cracking occurs [39].

As for 316L stainless steel, its stability should be between the 304 and 310 stainless steel owning to the Ni content. Under cathodic charging and aging process, phase transformation is observed in 316 stainless steel that ε and α’ are both identified but peaks are pretty small, which is illustrated in Fig. 2- 20 below [36]. Under gaseous charging condition, as stated beforehand, which is not as severe as cathodic changing, 316L can be stable. Moreover, no phase transformation observed in high pressure (up to 7 GPa, 350 °C, 24 h) hydrogen charging in 310 stainless steel [40]. Therefore, it is reasonable to predict no phase transformation ever happened on 316L stainless steel during the high pressure charging in this study. Even it happens, it can fully reverse the transformation during the aging. However, this prediction needs further proof and will be addressed later.

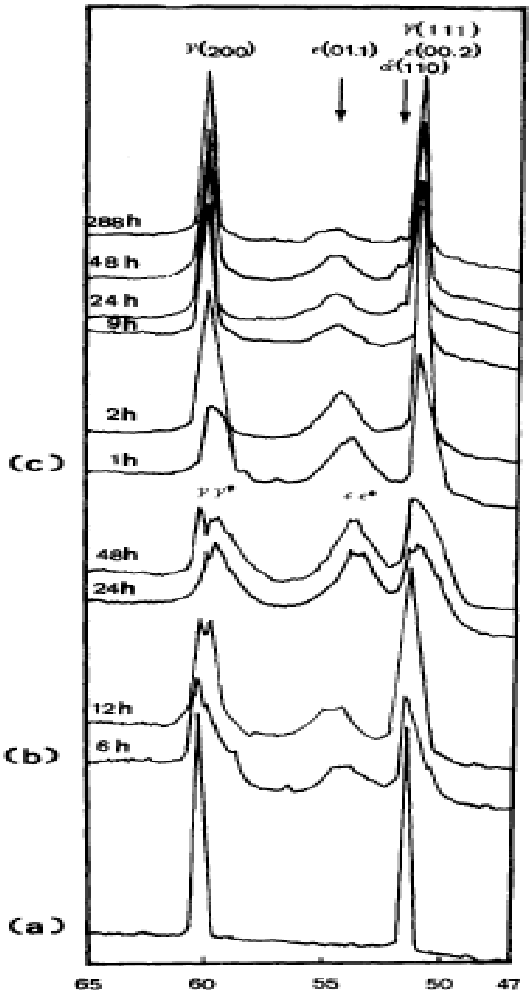

Fig. 2- 20 XRD patterns of 316 stainless steel: (a) uncharged, (b) after cathodic charging of 6, 12, 24 and 48 h (diffractograms were taken immediately after charging) and (c) after aging times of 1, 2, 9, 48 and 288 h (originally 48 h cathodically charged).

2.9.3 Hydrogen embrittlement mechanism

Macroscopic observations have confirmed that solute hydrogen can reduce the ductility and change the fracture mode from ductile (MVC) to brittle (intergranular or transgranular). Microscopic observations in stainless steel reveal that solute hydrogen can increase the mobility of dislocations and the propensity for planar slip and slip localization [24, 41, 42, 43, 44, 45].

The most popular mechanisms proposed to explain the effects associated with hydrogen embrittlement include hydrogen reducing the strength of atomic bonds (HEDE), which facilitates bond breakage [43, 45]; hydrogen shielding dislocations from interactions with other elastic obstacles [42], which allows dislocations to move at lower stresses; hydrogen reducing the stacking-fault energy (HELP) [41, 44], which decreases the tendency for cross-slip by increasing the separation distance between partials and stabilizing the edge component of dislocation. These mechanisms can operate in one system simultaneously. HEDE derives primarily from the conventional mechanical test. In situ environmental TEM observation gave rise to HELP and dislocation interactions theories. It is widely accepted that hydrogen dislocation interaction is prelude of embrittlement.

HEDE model is quite straightforward that, based on the mechanical experimental data, decrease in cohesive energy induced by hydrogen atoms is an “obvious” cause for embrittlement. In the HEDE model, hydrogen accumulates at trapping sites such as cracks or interfaces, and reduces the bond strength, i.e. grain boundary or cleavage plane cohesion so the cracking threshold is reduced. In other words, hydrogen decreases the energy barrier for grain boundary or cleavage plane decohesion. Supporting experiments show directly that, for example, the crack tip opening angle (CTOA) in stressed Fe–3wt.%Si and nickel single crystal decreases progressively with increasing hydrogen pressure (Fig. 2- 21) [43]. This can only be explained by a mixture of slip and bond breaking, as the latter increases with increasing pressure.

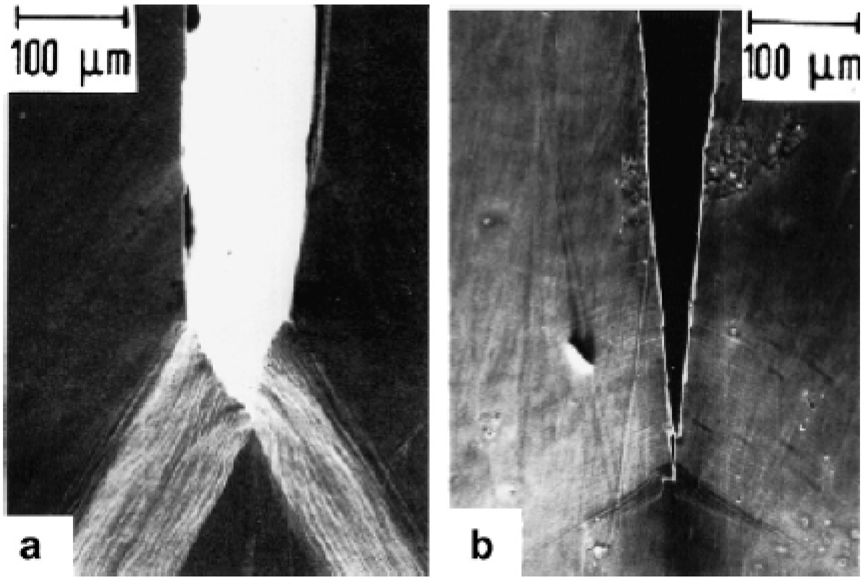

Fig. 2- 21 Hydrogen effect on the crack tip opening angle (a) vacuum, (b) hydrogen atmosphere

The susceptibility to hydrogen is confirmed in most metals and alloys, typically and macroscopically, from the view of HEDE, can be accentuated by the following factors [45],

multiaxial situations (with crack tip or thickness effects of plane strain vs. plane stress),
opening crack mode dominance, increasing yield strength, increasing hydrogen pressure or internal concentration,
increasing grain boundary segregation of metalloids,
decreasing elastic modulus.

The first tends to increase the concentration of hydrogen atoms at the crack tip, while others are believed to decrease the fracture threshold stress intensity.

Even though it cannot be denied that there is observation of brittle fracture surface on ductile FCC structure material (316L single crystal), HEDE alone seems to be insufficient to take the full responsibility of hydrogen-induced cracking. It is acceptable and reasonable for BCC material, which inherently experiences a ductile to brittle transition (DBT) at low temperature and of course the brittle cleavage mode dominates. However, this is not the case for FCC systems which possess numerous dislocation sources and therefore can be easily activated at any stress level and temperature. At room temperature for a FCC system like austenitic stainless steel in order to activate cleavage fracture, a larger than 80% decrease of local cracking threshold is required before any significant dislocation activity. This decrease is just too large to be real. So the HELP on the other hand focuses on the localized plasticity at the crack tip prevails nowadays [24].

HELP model focuses on microscopic unpinning of dislocations from their barriers and reduced stacking fault energy. Consequently, the presence of solid solution hydrogen enhanced dislocation mobility and localized deformation. Supporting evidences related to dislocation mostly come from in situ TEM work, which contributes a lot on the HELP theory development. But the area is always confined at the crack tip region due to the nature of TEM.

Fig. 2- 22 is a piece of in situ TEM work showing the introduction of hydrogen did weaken the interaction between dislocations, i.e. the reduction of separation distance. This further leads to the enhanced dislocation mobility [42].

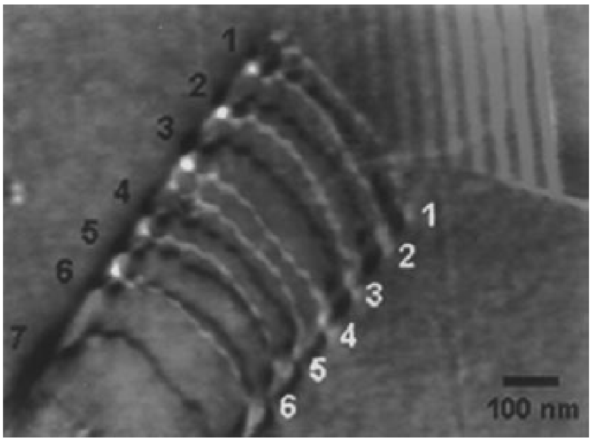

Fig. 2- 22 Composite image formed by superimposing an image from a pileup of dislocations against a grain boundary in vacuum (black number and dislocation line) and an image taken from the same pileup at constant stress, after introduction of 95 torr of hydrogen gas in the environment cell (white number and dislocation lines)

Besides TEM results, one kind of experimental evidence for HELP mechanism is the higher and further spaced slip step after hydrogen charging. In Altstetter’s paper [44], detailed hydrogen effect on 310 stainless steel was investigated. The increasing step height and separation distance of slip bands with increasing hydrogen content imply the slip localization as displayed in Fig. 2- 23. Theoretical aspect considered, the increasing separation of slip bands indicates the low SFE induced by hydrogen. Hydrogen separates the edge component and screw component further apart and makes it difficult to cross slip thus promotes the planar slip and further local plasticity enhanced. Another set of nanoindentation tests drew similar conclusion, as illustrated in Fig. 2- 24 [41]. Hydrogen increases the step height and separation space around the indentation.

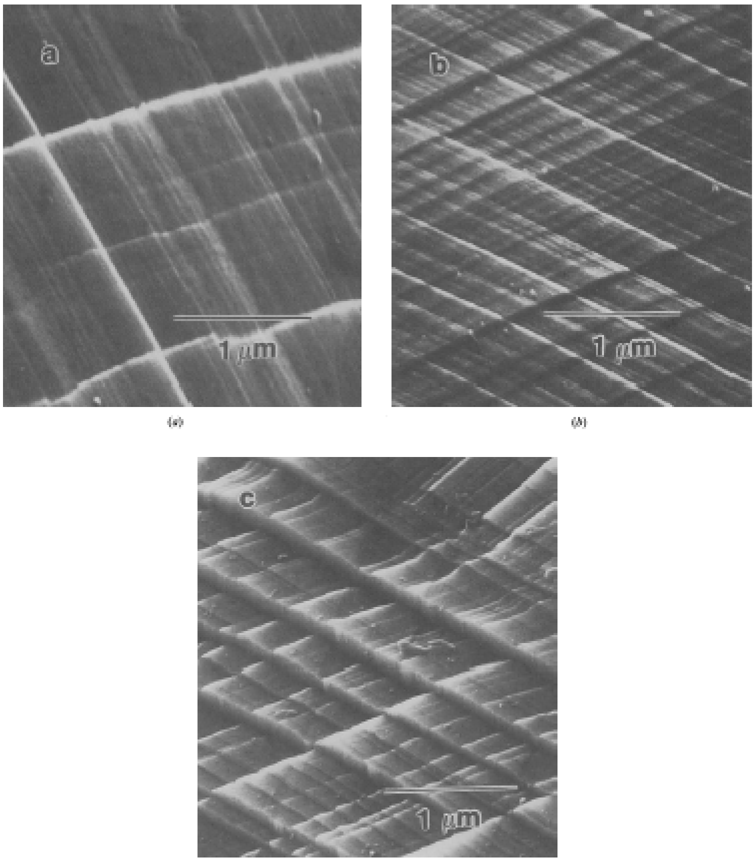

Fig. 2- 23 Side surfaces of 310s specimens tensile tested to failure at 295K and at a strain rate of 5×10^{-5}/s: (a) 0 at pct H, (b) 0.18 at pct H and (c) 2.7 at pct H

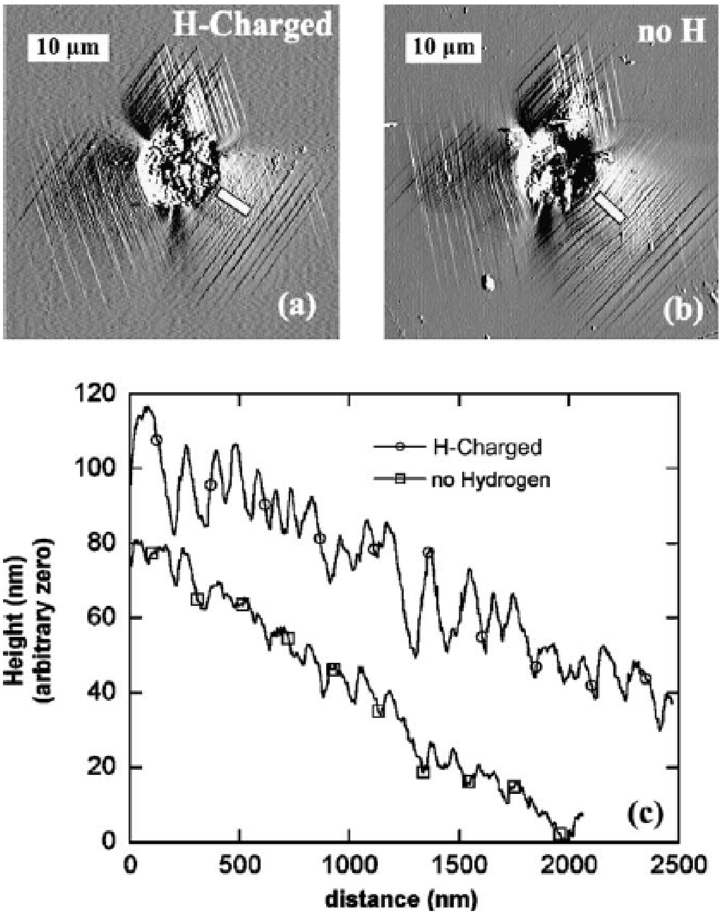

Fig. 2- 24 Derivative AFM images of 250 mN indentations made in the same grain of 21-6-9 stainless steel (a) after charging to 1.4 at. % hydrogen and (b) before charging. Cross sections generated from corresponding topographic images from the region marked with the white bar are shown in (c)

Another type of test is the relaxation test [44]. Stress relaxation is the time-dependent decrease in stress at constant temperature and displacement. The decrease in stress is the result of dislocation motion activated over local barriers. The assumption in the test is the dislocation density in the sample with and without hydrogen is the same. The change of stress and strain-rate over time is displayed in the Fig. 2- 25. It is obvious that the relaxation rate in the sample with hydrogen is much higher than that in the one without. It is tentative to suggest that the hydrogen can unpin the dislocation from local barrier that increases the mobility of dislocation. Table 2- 7 below summarizes and compared the process and interaction involved in HEDE and HELP.

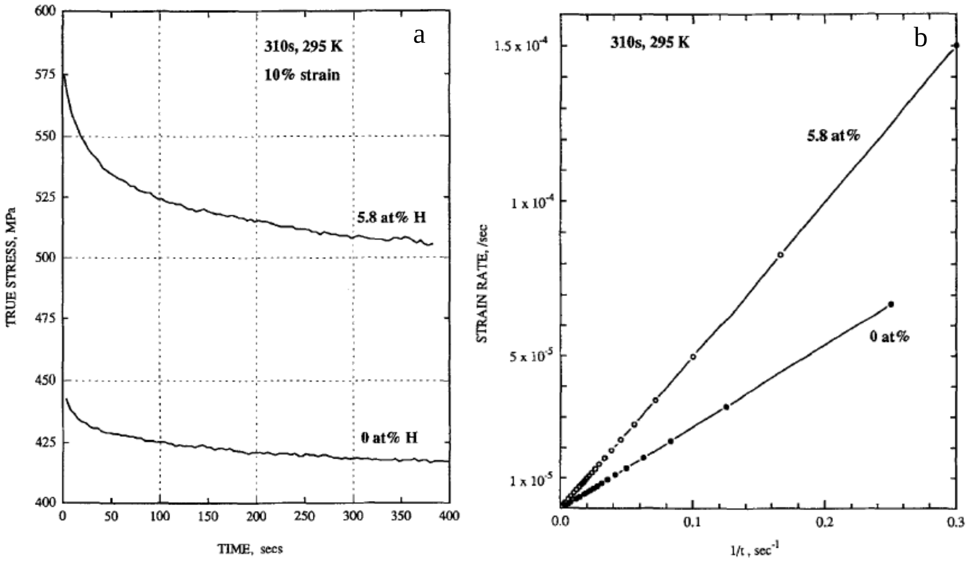

Fig. 2- 25 Stress relaxation tests on 310s specimens containing 0 and 5.5 at% hydrogen. (a) stress-time plot for specimens (b) plastic strain rate vs 1/t, during stress relaxation at 295 K

Table 2- 7 Processes involved in hydrogen transport and interaction for microscopic failure modes

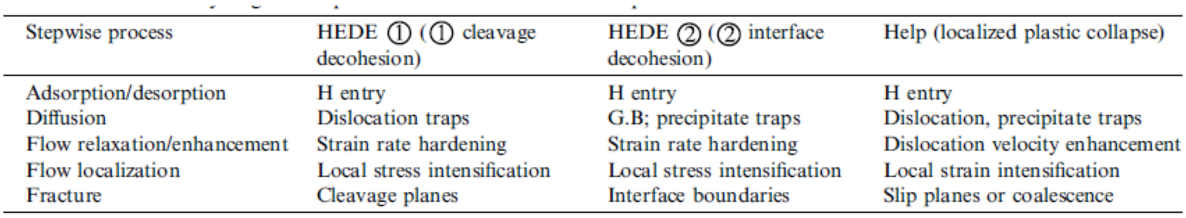

Stepwise process	HEDE ① (① cleavage decohesion)	HEDE ② (② interface decohesion)	Help (localized plastic collapse)
Adsorption/desorption	H entry	H entry	H entry
Diffusion	Dislocation traps	G.B; precipitate traps	Dislocation, precipitate traps
Flow relaxation/enhancement	Strain rate hardening	Strain rate hardening	Dislocation velocity enhancement
Flow localization	Local stress intensification	Local stress intensification	Local strain intensification
Fracture	Cleavage planes	Interface boundaries	Slip planes or coalescence

The HELP and HEDE can be related by considering the critical stress for dislocation emission and cleavage [45]. Fig. 2- 26 elucidates the principles. For the sample free of hydrogen, the loading path will intersect with dislocation emission prior to cleavage. If hydrogen incorporates, it brings down the critical cleavage stress. Ultimately, critical cleavage stress will be lower than the dislocation emission stress, and the HEDE dominates. But for FCC systems, because dislocation nucleation is much easier, it is too difficult to lower the cleavage stress to critical dislocation emission stress. Therefore in most FCC system cases, HELP dominates.

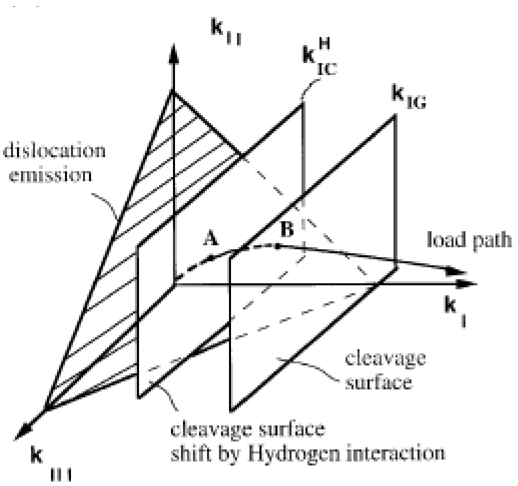

Fig. 2- 26 Schematic of relationship between HEDE and HELP

One common way to investigate dislocation nucleation for hydrogen embrittlement is nanoindentation. Typical loading-displacement curve is shown in Fig. 2- 27. There is usually a pop-in load signifying the onset of plasticity, i.e. dislocation nucleation. The required load for anodic is higher than that for cathodic, suggesting the sample is more susceptible to cathodic potential for this particular case which is copper.

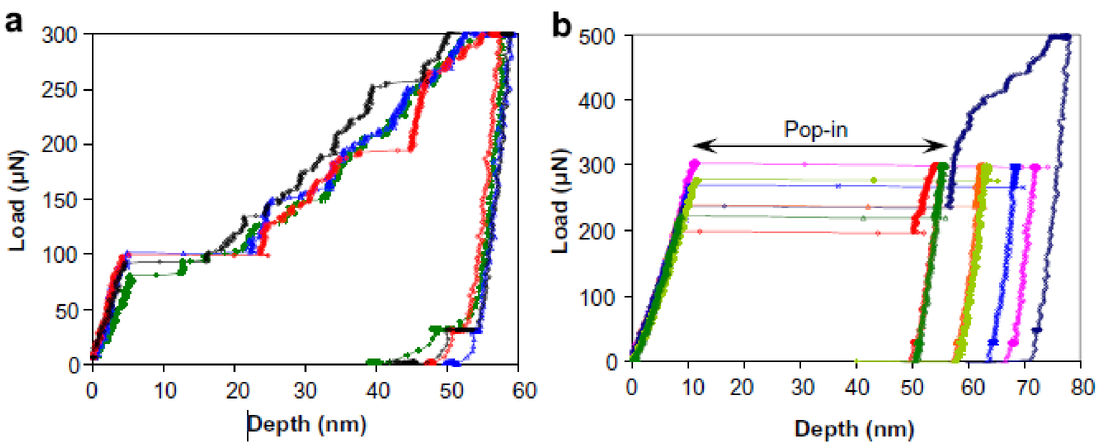

Fig. 2- 27 Load-displacement curves for nickel at cathodic potentials (a), and anodic potentials (b) (repeated to check reproducibility)

The critical homogeneous nucleation stress can be calculated. The resulting critical shear stress is related with shear modulus and SFE as illustrated in the Fig. 2- 28. In the figure, the line fulfills the relationship between the shear modulus and SFE. If the SFE is high (0.22 J/m^2), the reduction of shear modulus is obtained (61 GPa). The reduction in the elastic modulus is equal to the reduction of the strength of the interatomic bonds assumed in the HEDE model [43]. On the other hand, if the shear modulus stays high (78 GPa), SFE will decrease correspondingly to 0.17 J/m^2, which will alter the dissociation of partial dislocation and increase the separation of the partials. This implies an increase of activation energy for cross slip, in other word planar slip is promoted by incorporation of hydrogen. This localized slip supports the HELP mechanism.

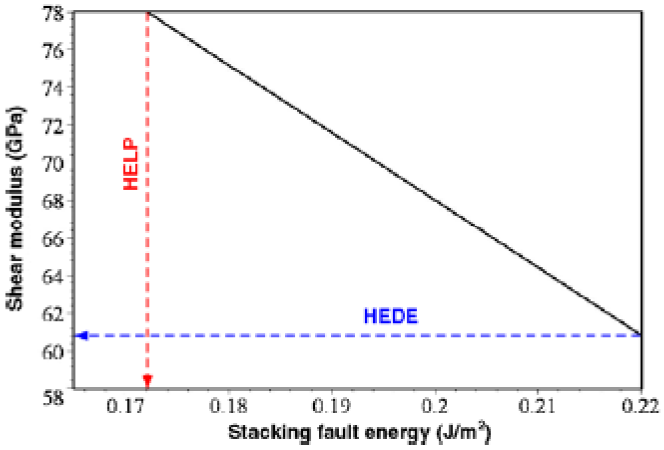

Fig. 2- 28 Possible changes in shear modulus and SFE due to hydrogen for overcoming the homogenous dislocation nucleation energy barrier.

Based on the knowledge of hydrogen embrittlement, the alloy design is advised, because it is the most controllable factor. Alloy composition influences, at least, two important characteristics of austenitic stainless steels: (i) slip planarity and (ii) phase stability. Both the low SFE and strain-induced martensite would exacerbate hydrogen embrittlement. Solute hydrogen was able to stabilize edge segments of dislocations which inhibited, or even stopped dislocations from cross-slipping (equivalent to decrease of SFE). Removal of hydrogen from the sample allowed the cross-slip to continue [46]. In contrast, high SFE implies great tendency to cross slip and high resistivity to planar slip so to hydrogen embrittlement. Phase stability is also an important indicator for hydrogen embrittlement resistivity. Once the strain-induced martensite forms, it behaves as a highway for hydrogen diffusion [47]. The diffusion rate of hydrogen in martensite is orders of magnitude higher than that in austenite. Point can be demonstrated in the Fig. 2- 29. For 304 stainless steel, the hydrogen penetration depth is much higher in the pre-strained sample than that of the pristine one. The hydrogen goes even deeper, as more pre-strain the material went through. For 316 and 310 stainless steel, the hydrogen penetration depth stays relatively the same, irrespective of pre-strain level, which is certainly due to the stability of austenite phase. Nevertheless, what’s more important is martensite as distorted BCC structure is inherently more susceptible to hydrogen. This phase transformation aggravates the embrittlement.

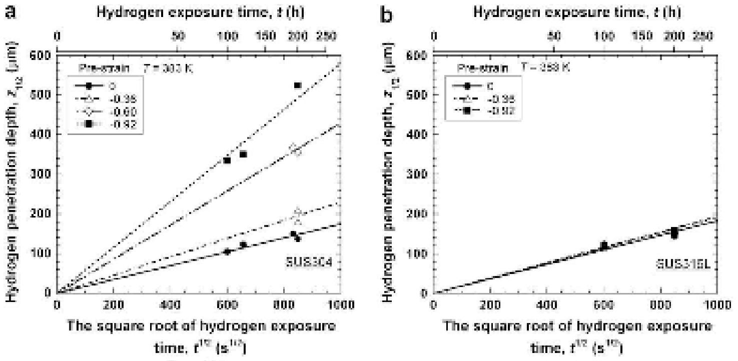

Type 304 Type 316L

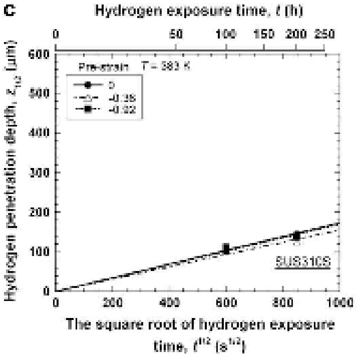

Type 310S

Fig. 2- 29 Relationships of hydrogen penetration depth with hydrogen exposure time as a function of the degree of pre-strain for type 304, 316L and 310S stainless steel

Nickel comes into vision because it can increase the SFE, which counterbalance the detrimental effect from hydrogen. The addition of nickel also stabilizes the austenite phase in the stainless steel enhancing the resistivity of alloy to hydrogen [27]. No other common alloy element can do them simultaneously.

Caskey [48] is actually first reported the strong dependence on nickel content level of the degree of the austenitic stainless steel hydrogen embrittlement. The resistance of hydrogen embrittlement increases substantially from 8% (RRA=20%) to 12% (RRA=90%) Ni content but the scatter of these data point (at 12 wt% Ni) is relatively large as presented below (Fig. 2- 30). Once it comes close to 13%, it seems the stainless steel become immune to hydrogen (RRA=1). The large scatter of RRA at 12% nickel content is probably attributed to the macro segregation of nickel during the processing [49]. Area with low nickel content will transform to martensite under the strain and thus a much higher diffusion rate achieved. Less tensile reduction can be expected in this area. While for nickel up to 13%, the variability of tensile data seems to diminish which can be due to the enough nickel content to distribute evenly and prohibit the local embrittlement mentioned before. Unfortunately, the cost of material also increases as more Ni added in the alloy. So people engaged in finding substitute to nickel in order to reduce cost.

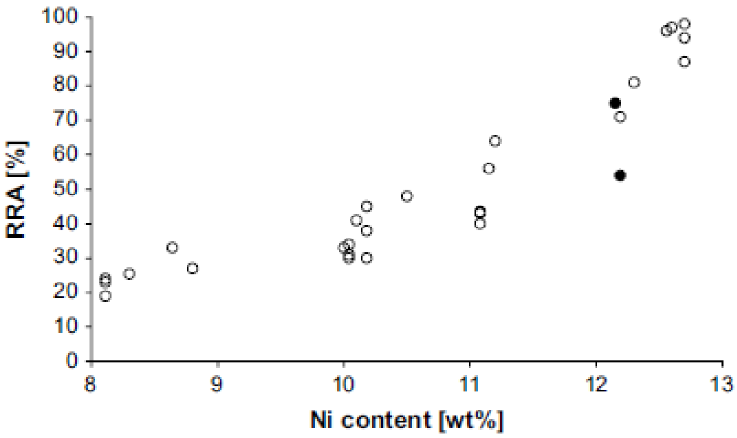

Fig. 2- 30 RRA values of austenitic stainless steels with different Ni content

What is worthwhile to mention is the hydrogen embrittlement is actually also a function of temperature, as shown in Fig. 2- 31. Except 310, in which there is huge amount of Ni, all the other type stainless steels experience a minimum ductility around 200 K [1].

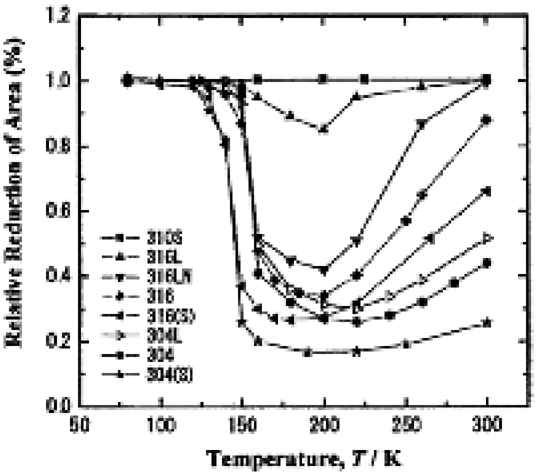

Fig. 2- 31 Relative reduction of area for various austenitic stainless steel tensile tested at 10 bar

2.9.4 Hydrogen induced cracking threshold

Other than RA, hydrogen induced cracking behavior is also extensively studied in the area of steel [4, 50, 51, 52, 53, 54]. For this kind of experiments, cracking threshold and stable cracking propagation velocity are the criterions employed to characterize the embrittlement. Fig. 2- 32 [55] is a schematic of typical experimental curve. There are usually three crack growth regions. At higher K end, where K is large and approaches the K_{IC}， the crack grows very fast and tends to be unstable before ultimately fractures. The intermediate region is stable growth region where the crack growth velocity stays nearly the same. When K is even lower, the crack growth velocity descends rapidly and essentially terminates at some threshold value (K_{th}). K_{th} is usually defined as at which stress intensity level the crack growth velocity is less than 10^{-10} m/s. Threshold is often considered to be more substantial parameter because it signifies the initiation of the crack. Thus more studies focused on threshold value investigation. Several factors can influence the threshold value, like yield strength, H_2 pressure and temperature, among which yield strength seems to be the most influential factor.

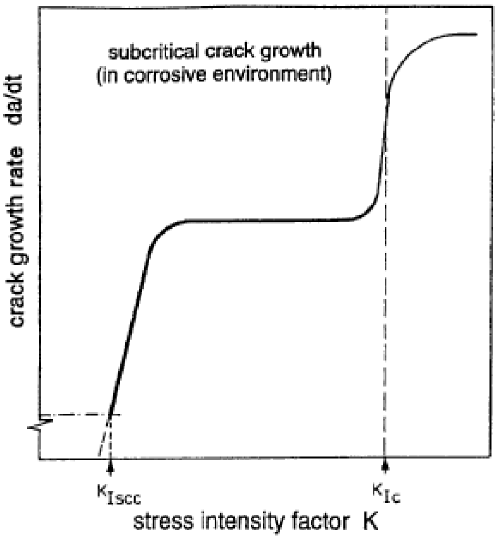

Fig. 2- 32 Schematic diagram showing the relationship between the stress intensity factor and the crack growth rate da/dt

Perng and Altstetter [50] studied the cracking extension velocity and threshold of austenitic stainless steel (301 and 310) and ferritic stainless steel (AL 29-4-2). The composition of these three stainless steels is listed in Table 2- 8. In their study, no slow crack growth was ever observed in 310 stainless steel, while 301 is more susceptible to hydrogen embrittlement and has higher cracking velocity than AL 29-4-2. The relatively high velocity in 301 stainless steel is due to the fast hydrogen transport through the stress-induced α’ martensite at the crack tip and low escape rate of hydrogen through the γ phase in the surrounding region. So faster hydrogen accumulation is expected in 301 stainless steel, leading to the observed high cracking velocity.

Table 2- 8 Chemical composition (wt pct) of the AISI 301, 310 and AL 29-4-2 [50]

Material	C	Mn	P	S	Si	Cr	Ni	Mo	N	Cu	O	H
AISI 301	0.082	1.29	0.023	0.012	0.49	17.05	7.17	-	0.056	0.20	0.0079	1.1×10^{-4}
AISI 310	0.054	1.90	0.022	0.004	0.65	24.76	19.55	0.11	0.049	0.17	-	-
AL 29-4-2	0.0029	0.10	0.01	0.009	0.10	29.5	2.23	3.93	0.012	-	-	-

Effect of yield strength

The general trend for yield strength dependent cracking threshold is illustrated by Fig. 2- 33 [52]. As the yield strength decreases, the threshold actually increases and time to failure prolongs as well. Detail studies have been done in this area. Different yield strengths were achieved through different heat treatments for the same material, like B2, B6 and B7, compositions of which are summarized in Table 2- 9 [4]. The test results for K_{IC} and K_{th} for all these three steels are exhibited in Fig. 2- 34. All the tests are done in 0.11 MPa H_2 at 296 K. In all of three series steels, K_{IC} and K_{th} descend as yield strength rise. The threshold decrease is reasonable, because as the strength goes up the material itself tends to be brittle.

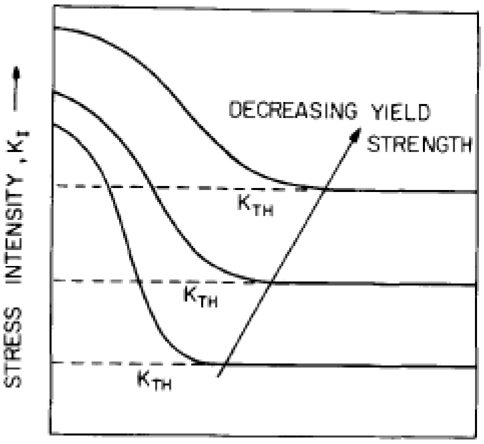

Fig. 2- 33 Schematic depicting threshold stress intensities for three different yield strength steels

Table 2- 9 Chemical compostion (wt%) of B2, B6 and B7

Steel	C	Mn	Si	P	S	Ni	Cu	Cr	Mo	Al	V	Co
B2	0.39	0.68	0.08	0.009	0.016	1.72	-	0.73	0.22	0.046	0.05	0.04
B7	0.37	0.007	0.002	0.003	0.003	1.82	0.002	0.81	0.25	<0.001		
B6	0.37	0.72	0.32	0.003	0.005	1.8	-	0.75	0.26	-		

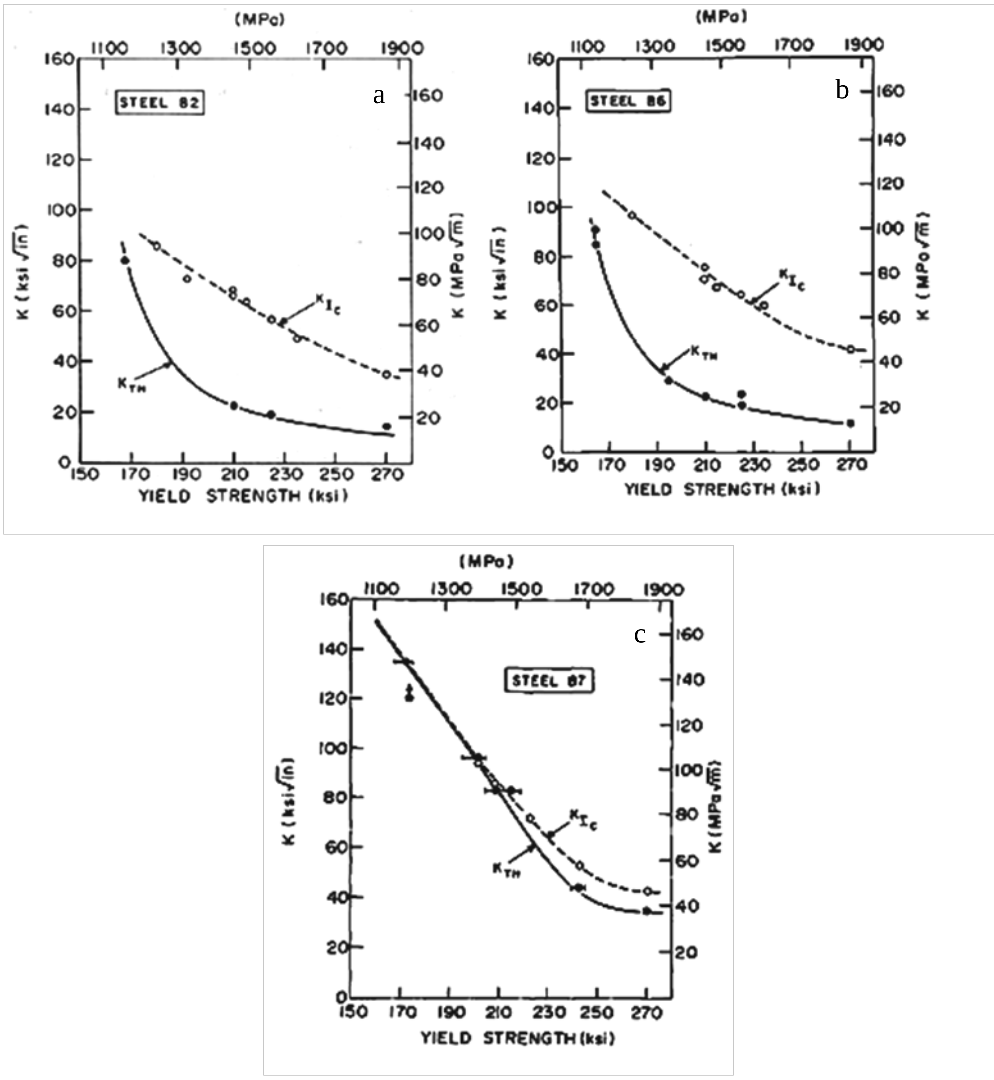

Fig. 2- 34 Variation of K_{IC} and K_{th} in 0.11 MPa H_2 at 296 K with different yield strengths, (a) B2, (b) B6 and (c) B7

Similar tests were carried out on various kinds of stainless steels. Perra [56] did sustained-load cracking test on austenitic steels in high pressure gaseous hydrogen (100 MPa and 200 MPa). Compositions and properties of tested alloys were listed below in Table 2- 10 and Table 2- 11. All theses seven alloys studied are austenitic and 316 is drawn special attention because of the similarity to the material used in this study.

Table 2- 10 Alloy composition used in sustained load testing (wt pct)

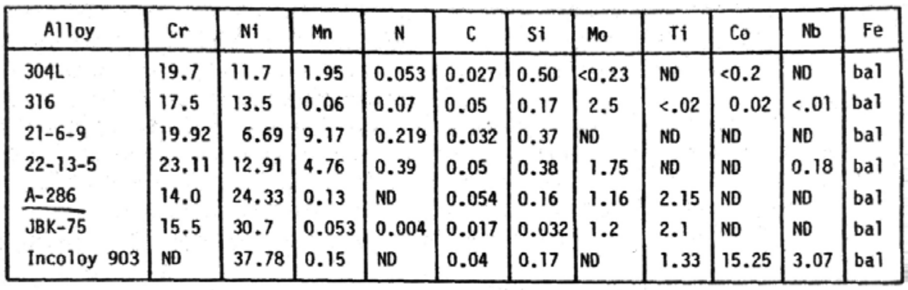

Alloy	Cr	Ni	Mn	N	C	Si	Mo	Ti	Co	Nb	Fe
304L	19.7	11.7	1.95	0.053	0.027	0.50	<0.23	ND	<0.2	ND	bal
316	17.5	13.5	0.06	0.07	0.05	0.17	2.5	<.02	0.02	<.01	bal
21-6-9	19.92	6.69	9.17	0.219	0.032	0.37	ND	ND	ND	ND	bal
22-13-5	23.11	12.91	4.76	0.39	0.05	0.38	1.75	ND	ND	0.18	bal
A-286	14.0	24.33	0.13	ND	0.054	0.16	1.16	2.15	ND	ND	bal
JBK-75	15.5	30.7	0.053	0.004	0.017	0.032	1.2	2.1	ND	ND	bal
Incoloy 903	ND	37.78	0.15	ND	0.04	0.17	ND	1.33	15.25	3.07	bal

(1) ND = Not Determined

Table 2- 11 Strengthening treatments studied and associated form temperature tensile properties

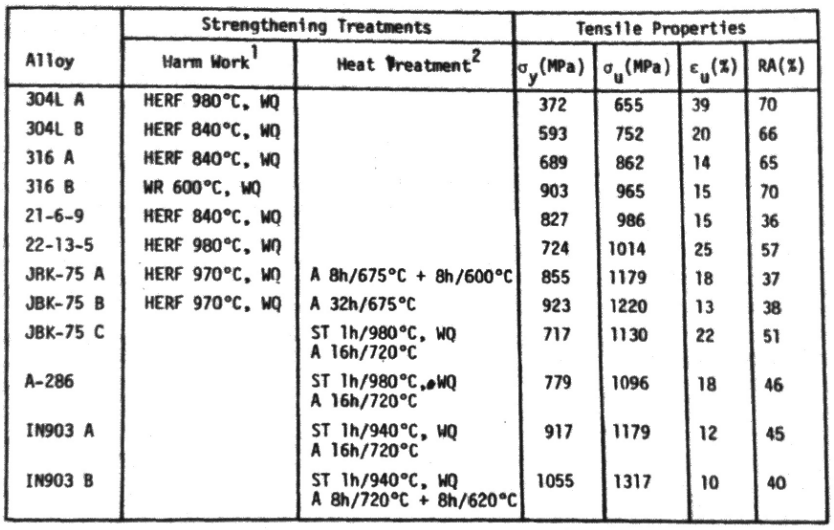

Alloy	Strengthening Treatments		Tensile Properties			
	Harm Work[1]	Heat Treatment[2]	σ_y(MPa)	σ_u(MPa)	ϵ_u(%)	RA(%)
304L A	HERF 980°C, WQ		372	655	39	70
304L B	HERF 840°C, WQ		593	752	20	66
316 A	HERF 840°C, WQ		689	862	14	65
316 B	WR 600°C, WQ		903	965	15	70
21-6-9	HERF 840°C, WQ		827	986	15	36
22-13-5	HERF 980°C, WQ		724	1014	25	57
JBK-75 A	HERF 970°C, WQ	A 8h/675°C + 8h/600°C	855	1179	18	37
JBK-75 B	HERF 970°C, WQ	A 32h/675°C	923	1220	13	38
JBK-75 C		ST 1h/980°C, WQ A 16h/720°C	717	1130	22	51
A-286		ST 1h/980°C, WQ A 16h/720°C	779	1096	18	46
IN903 A		ST 1h/940°C, WQ A 16h/720°C	917	1179	12	45
IN903 B		ST 1h/940°C, WQ A 8h/720°C + 8h/620°C	1055	1317	10	40

1. HERF = High Energy Rate Forged. WR = Warm Rolled. WQ = Water Quenched.
2. ST = Solution Treated. A = Aged.

Two tests were done on 316 stainless steel of the same composition, but one with 689 MPa yield strength (316A) and the other with 903 MPa (316B). What surprising but reasonable is that, as indicated in Table 2- 12, cracking threshold for 316B is 99 MPa. However, no crack initiation noted for 316A under 100 MPa gaseous hydrogen. Similar observation happens in JBK-75 A and JBK-75 B and In 903A and In 903 B. Lower threshold for higher strength rule is followed. JBK-75 C is anomalously low because of the presence of second-phase precipitates on grain boundaries. On the basis of the conclusion from the same study, 316L used in this study, with yield strength of

170 MPa, should never crack.

Table 2- 12 Threshold stress intensity values for steels exposed to 100 and 200 MPa hydrogen gas

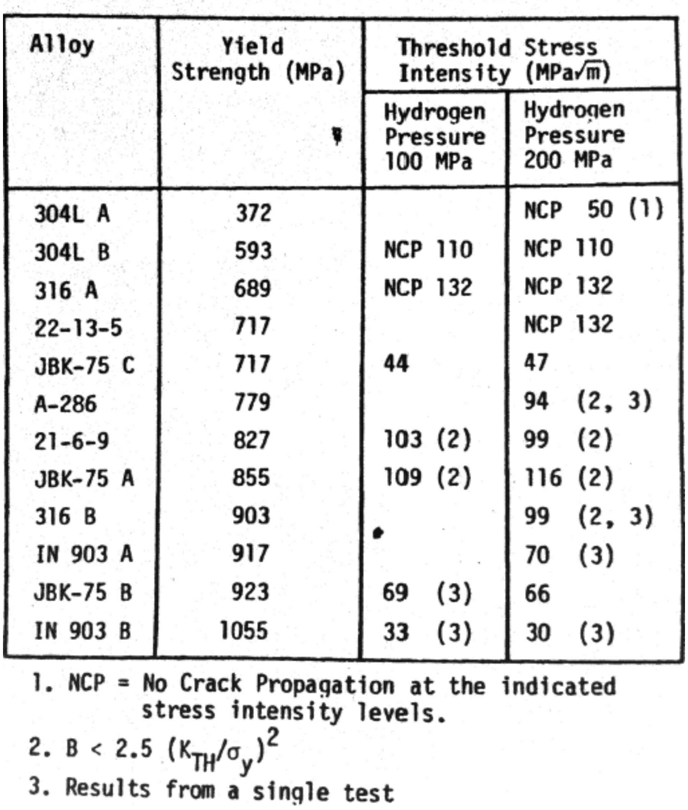

Alloy	Yield Strength (MPa)	Threshold Stress Intensity (MPa$\sqrt{m}$)	
		Hydrogen Pressure 100 MPa	Hydrogen Pressure 200 MPa
304L A	372		NCP 50 (1)
304L B	593	NCP 110	NCP 110
316 A	689	NCP 132	NCP 132
22-13-5	717		NCP 132
JBK-75 C	717	44	47
A-286	779		94 (2, 3)
21-6-9	827	103 (2)	99 (2)
JBK-75 A	855	109 (2)	116 (2)
316 B	903		99 (2, 3)
IN 903 A	917		70 (3)
JBK-75 B	923	69 (3)	66
IN 903 B	1055	33 (3)	30 (3)

1. NCP = No Crack Propagation at the indicated stress intensity levels.
2. $B < 2.5 (K_{TH}/\sigma_y)^2$
3. Results from a single test

With the noted exceptions, the threshold results of the austenitic steels observed tend to fall within a single broad band as illustrated in Fig. 2- 35. A common feature of the alloys within the band is that the fracture path is intergranular and no significant second-phase precipitation is observable at the grain boundaries within the resolution of TEM. This band probably sets the upper limit of to the resistance of austenitic steels in gaseous hydrogen, unless the grain boundary properties improved.

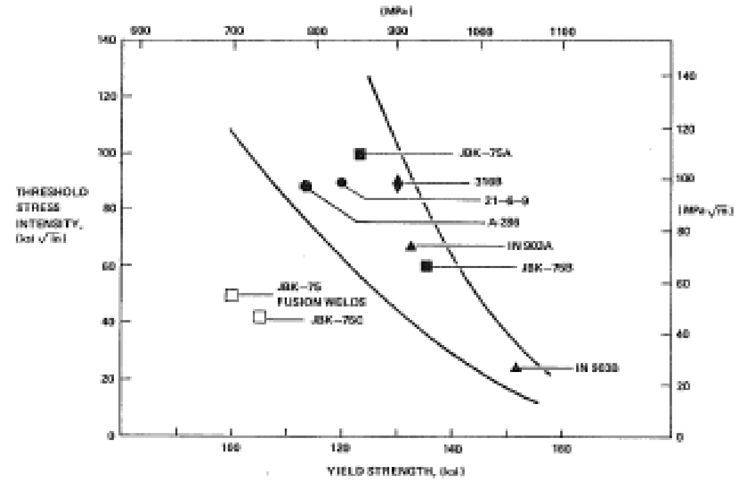

Fig. 2- 35 Materials with higher yield strengths generally possess lower threshold stress intensity values. The exceptions to this trend illustrate the importance of local microstructure along the crack path in determining crack propagation resistance

Besides above mentioned cracking threshold study on 316 stainless steel, other results are still available. At thickness of 1.55 mm, K_{th} of 316L stainless steel (no yield strength information available) is 38.5 $\mathrm{MPa}\sqrt{m}$ under cathodic charging condition [53]. Another study observed threshold larger than 77 $\mathrm{MPa}\sqrt{m}$ at 207 MPa gaseous hydrogen test condition for forged 316 stainless steel [57].

Effect of hydrogen pressure

A hydrogen pressure dependent behavior is observed in 4340 steel [4]. In Fig. 2- 36 thresholds go down gradually as pressure varies from 0.027 MPa to 0.21 MPa. Though this hydrogen pressure is still low compared with high pressure hydrogen, the curve tends to be really flat at the tail, implying weak dependence on hydrogen pressure at high pressure range. Similar threshold dependence on pressure was studied elsewhere [50]. In Fig. 2- 37, thresholds of AISI 301 and AL 29-4-2 decrease with the increasing hydrogen pressure as well. But in the real high pressure condition, like in Perra's study [56], the threshold seems to be independent of hydrogen pressure, as shown in Table 2- 12 above. The 100 MPa and 200 MPa pressure do not make much difference but essentially the same to the threshold.

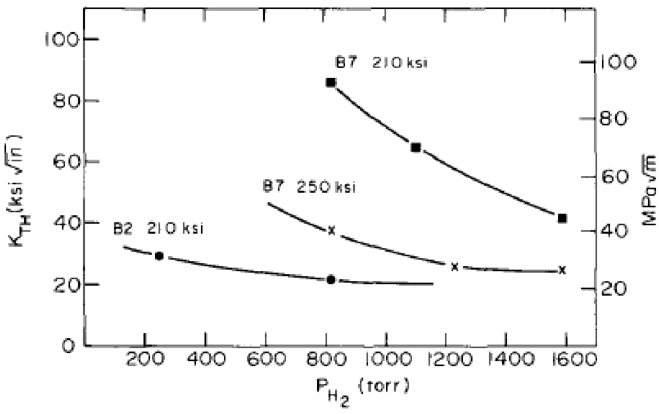

Fig. 2- 36 Variation of K_{th} with hydrogen pressure at 296 K for commercial steel B2 and B7 at two yield strength levels

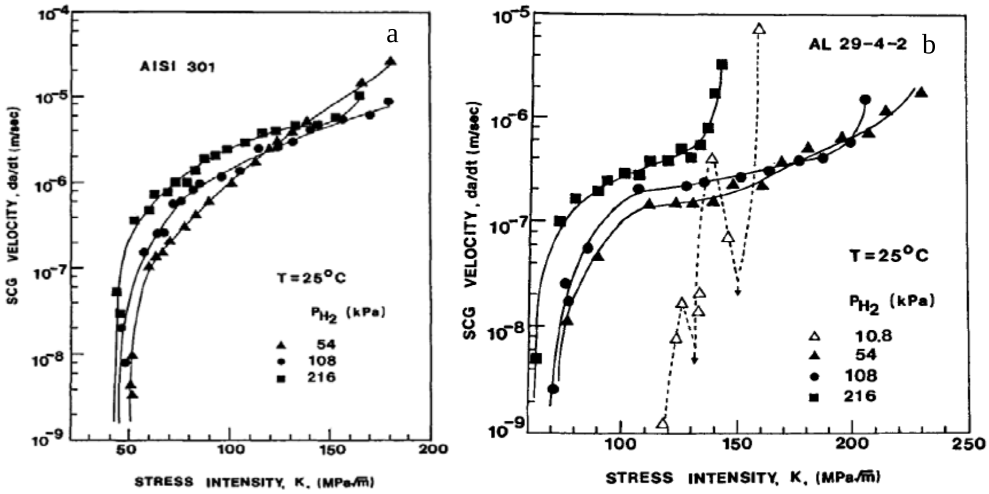

Fig. 2- 37 Crack growth rate of AISI 301 (a) and AL 29-4-2 (b) tested at 25 °C and various pressures of hydrogen gas

Possible explanation of these observations is the hydrogen traps that serve as embrittlement sites. At low pressure condition, when pressure goes up, more and more absorbed hydrogen atoms occupy the hydrogen traps and thus deteriorate the resistance to the embrittlement. Nevertheless, when pressure is really high, like 100 MPa or 200 MPa, the hydrogen trap sites will be saturated by hydrogen atoms and thus steels behave as if independent of hydrogen pressure.

Effect of temperature

Temperature is another active factor that influences embrittlement significantly. As shown previously (in Fig. 2- 31), the RA values of most stainless steels experience a minimum around 200 K, implying the hydrogen embrittlement is indeed a function of temperature. However, if only within 100 K range around room temperature considered, the influence of temperature is minor.

IG vs threshold

Intergranular (IG) is the usual fracture mode in ferritic steel and transgranular is the dominant mode for stainless steel. IG mostly happens in the case of weakened grain boundary as the preferential crack path. IG is mainly due to the segregation of phosphors and sulphur on the grain boundary. The relationship between IG percent and threshold for 4340 is summarized in Fig. 2- 38 (a) and it is almost linear. IG percent is plotted against the composition (Mn, Si, P and S) in Fig. 2- 38 (b) as well. Mn and Si are included since they are believed to promote the segregation P and S on grain boundaries. It is clear IG fracture mode is due to the detrimental segregation of impurities on the grain boundaries. IG fracture can be a sign of embrittlement. Once it appears on fracture surface, the threshold is compromised.

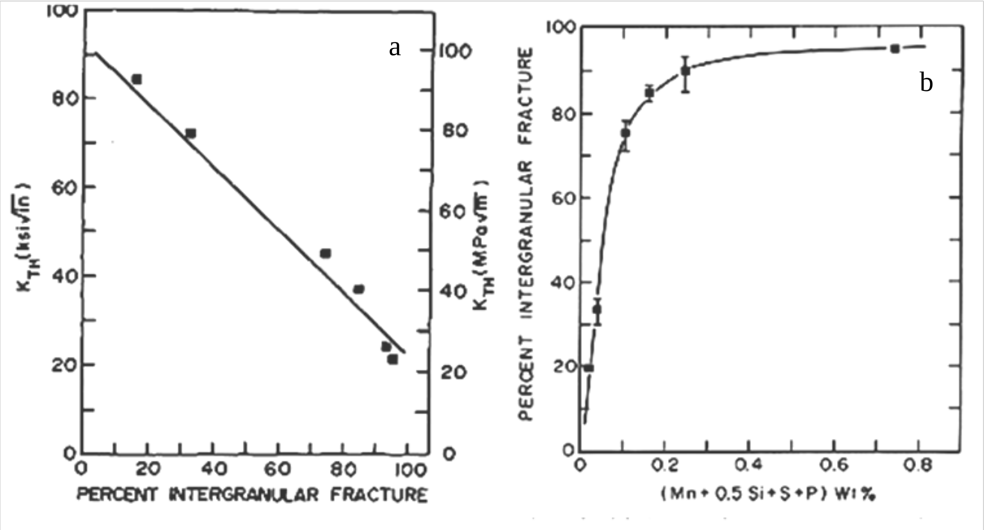

Fig. 2- 38 (a) Relationship between K_{th} and corresponding percent intergranular fracture in steels, (b) correlation between the increase in percent intergranular fracture with the composition parameter in the specimens

3. Tests

3.1 Specimen preparation

In this study, all 316L stainless steels were provided and carburized by Swagelok Company. Specimens were first cut from the same batch of 316L and machined into the WOL configuration [11]. Specifications of WOL samples used in this study are shown in Fig. 3- 1. After machining, six samples were pre-cracked, in order to eliminate or minimize the effect of machining notch. The 2 mm long pre-crack was introduced by high cycle fatigue under constant stress intensity condition (~20 MPa$\sqrt{}$m and r_p ~ 2.2 mm). Then samples were sent out to Swagelok Company and three of them went through the LTCSS treatment. Hydrogen charging process was followed by Sandia Corp. and performed in 138 MPa gaseous hydrogen at 573 K for 24 days, for which the equilibrium hydrogen content is predicted to be ~148 wppm (parts per million hydrogen by weight) [35]. This charging condition was sufficient for specimens of this thickness to become uniformly saturated by hydrogen. After charging, samples were delivered and then reserved in the freezer for further usage. The loss of hydrogen is negligible at room temperature [35] and so keeping the samples in freezer is appropriate.

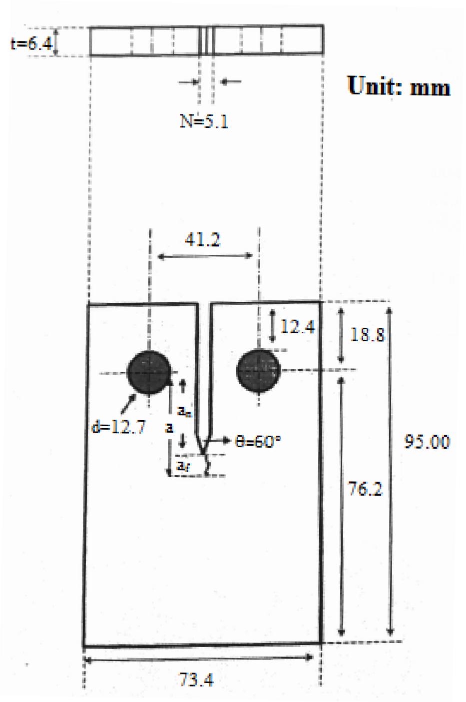

Note 1 – Dimensions are in millimeters

Note 2 – Figure is not drawn by scale

Note 3 – Recommended thickness: $W/20 \leq B \leq W/4$

Note 4 – $a = a_n + a_f$, where a_n, 33.8 mm, is the machined notch and a_f is the fatigue crack length

Fig. 3- 1 Specifications of WOL specimen of this study

3.2 Testing apparatus

Equipments utilized in the test consist of a hydraulic power supply (Fig. 3- 2), a horizontal fatigue testing machine MTS 450.2 (Fig. 3- 3). The data was acquired by software, Labview 6.1. Specimens were mounted on the machine by a pair of grips in the horizontal way as illustrated in Fig. 3- 4. The operation system is able to control the test in three different modes: displacement control, load control and COD control.

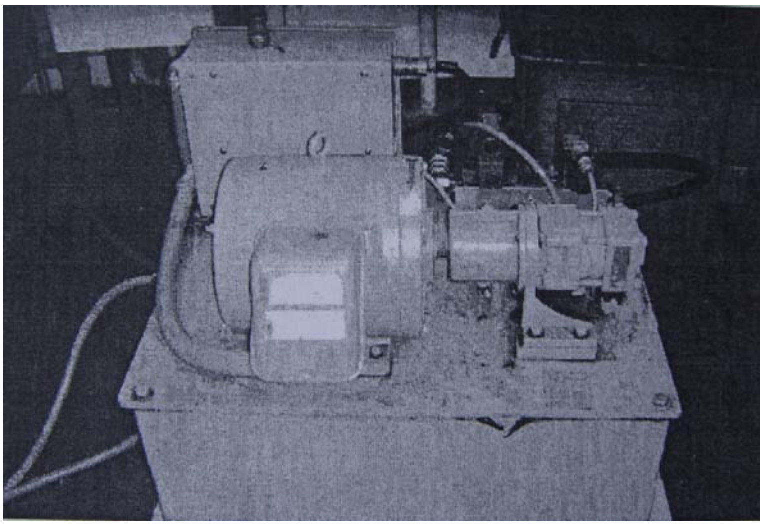

Fig. 3- 2 Hydraulic power supply has greater flexibility than mechanical and electrical systems and can produce more power than other systems of equal size

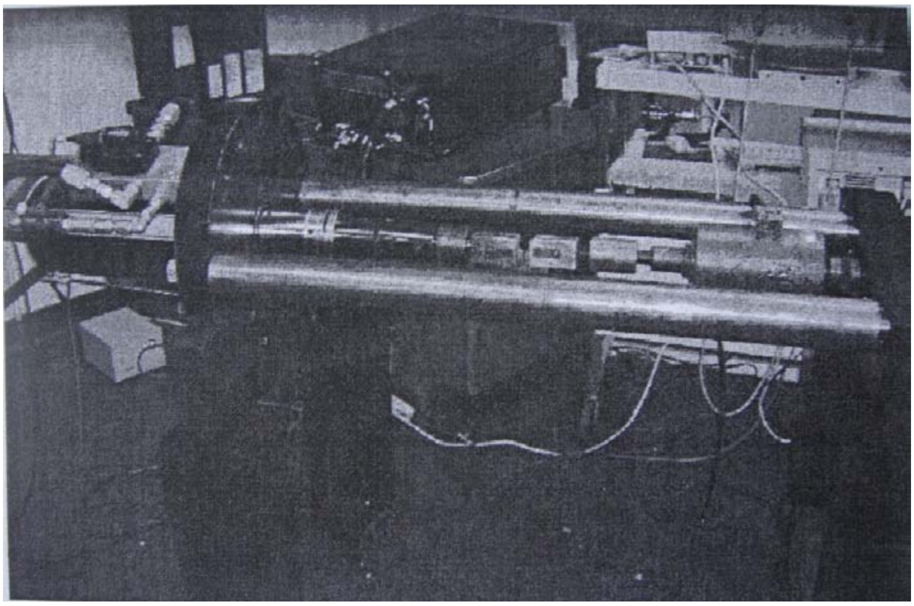

Fig. 3- 3 Horizontal fatigue testing machine MTS 450.2

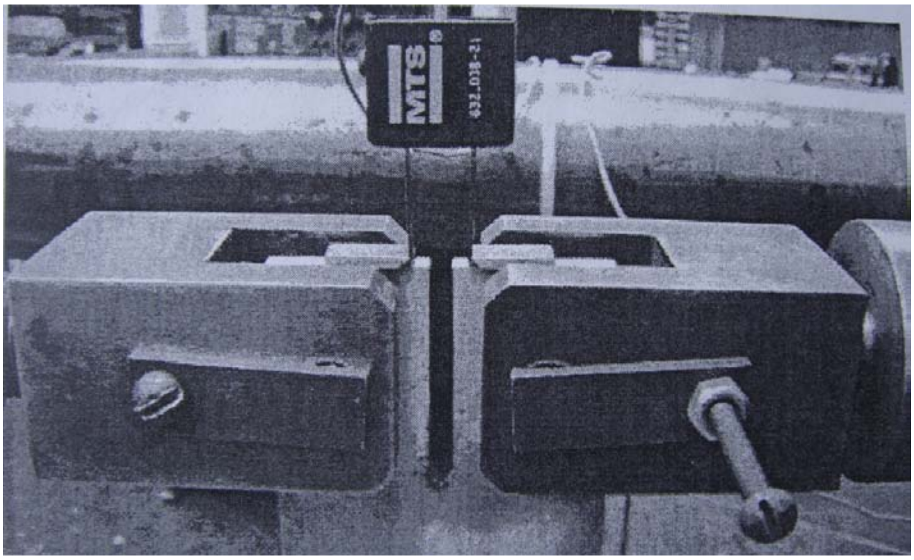

Fig. 3- 4 A WOL sample was mounted on loading cell by a pair of grips

3.3 Wedge test

In order to apply a sustained load on the sample when it is removed from the machine, a wedge with certain thickness is required. With the help of wedge, the observations of possible crack propagation and plastic zone evolution over time can be realized. Fig. 3- 5 is a sketch of wedge put in the WOL sample. The design of a wedge must ensure proper thickness (B) and length (L), which applies a proper load at the load line (LL). The fabrication tolerance for wedge is 0.0005”, which sets the limitation of our design. Wedge design details will be addressed later. Before any practical design, several other issues which the design is based on must be dealt with.

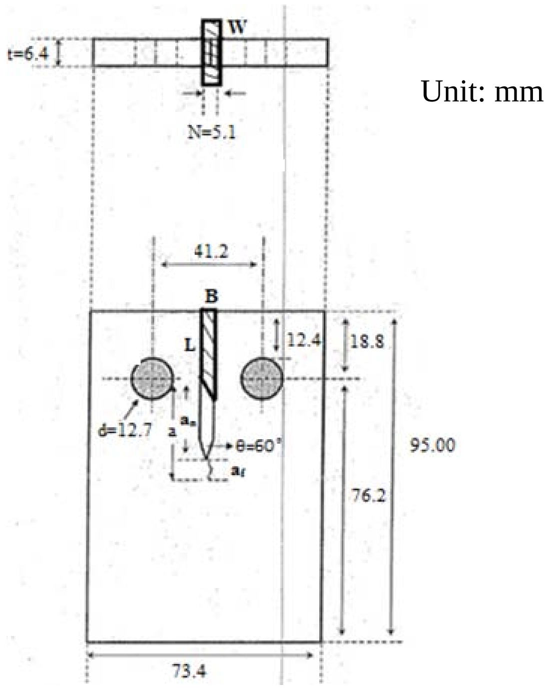

Fig. 3- 5 Sketch of wedge in the WOL sample

3.3.1 Compliance

Compliance is defined as how compliant the sample is and it is the reciprocal of the stiffness. Mathematically compliance equals to crack opening displacement over load. Data acquired by software after one test is the plot of load (lb) vs COD (inch) in a 2D x-y system. The slope of loading and unloading curve defines the stiffness of the sample, so the compliance is readily available. If the crack propagates during the test, the compliance of the sample will increase, i.e. the sample stiffness decays. In other words, lower load is needed for specimen to achieve the same COD, or under the same load, the COD received is larger. The reason is straightforward: when crack propagates there is less intact material left ahead of the crack thus the resistance of the sample to the external load becomes weaker.

The significance of the compliance is that it provides a mechanical way to determine the crack length. It gives an average crack length through the thickness of the sample, in the light of the crack tip through the thickness is usually curved, as can be seen in Fig. 3- 6. So instead of only observing the crack on the very surface, quantification of the overall crack length is possible.

However, before taking it for granted, the accuracy of this method must be verified. Sample CT6 was precracked by fatigue then carburized. It was tested in the corrosion fatigue condition (in 3.5wt% NaCl solution) previously. The crack propagated in the solution can be easily identified by the brown color on the fracture surface. Before being torn apart, the sample experienced several fatigue sessions and detailed fatigue parameters were summarized in the Table 3- 1. After each fatigue session, a complete P vs COD curve (including loading and unloading portions) was recorded. All the curves were used to compare the calculated crack length by compliance method with the actual crack length read on the fracture surface.

Table 3- 1 Different tests on CT6 before final failure

	Method	K_i (MPa√m)	K_f (MPa√m)
Corrosion fatigue	Constant load	14.7	20.7
Loading practice	COD control	29.7	51.4
Fatigue	K decreasing	27.3	16.7
Fatigue	K constant	27.3	27.3
Fatigue	K decreasing	27.3	15.0

After final fracture, a photo was taken for CT6 fracture surface along with a ruler as a reference scale (Fig. 3- 6). Due to the curvature of the crack tip, which can be confirmed easily, five straight red lines were drawn on the fracture surface, in order to get an average crack length. One in the middle of the fracture surface and two on the very surface of each side, last two were in the middle of the first three lines. The length is measured by the software ImageJ and the scale bar is taken from the ruler. One straight short line was draw to signify the intersection of the red lines and the curve of each crack tip. All the crack length readings were summarized in the Table 3- 2. This method works pretty accurately, as the error is less than 1% for all the five crack length checked. But the error when a/W is larger than 0.75 becomes larger than that otherwise. This may indicate the accuracy is better when the crack length is shorter. However, the inherent shortcoming is that the sensitivity of this method is still low. Though the 1% error sounds good, it is still around 0.5 mm difference between calculation and actual crack length. If the crack propagation is small, like 0.2 mm, then this method is not reliable.

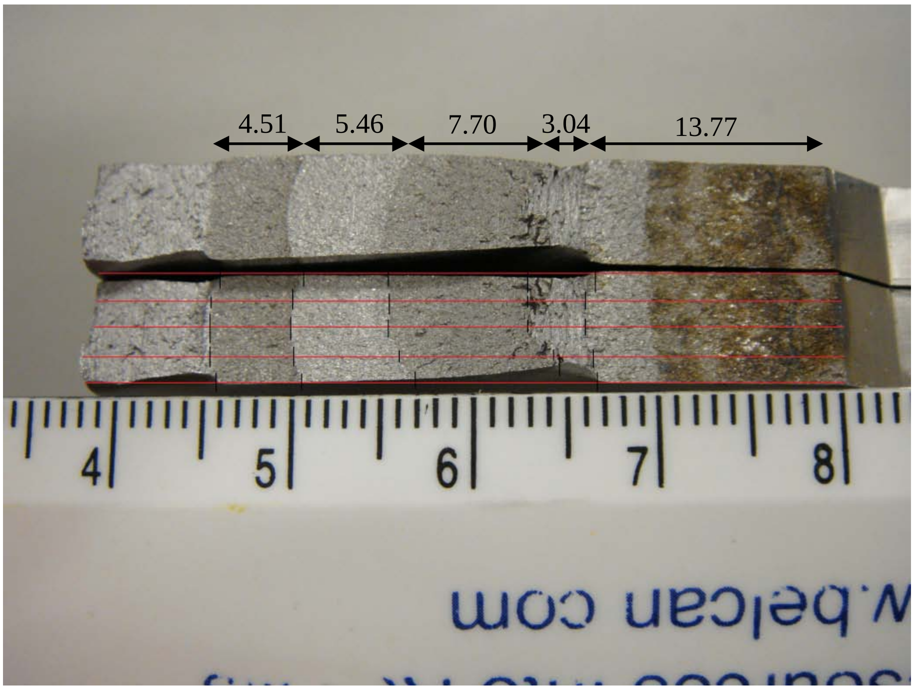

Fig. 3- 6 Fracture surface of sample CT6 with scale (unit: mm)

Table 3- 2 Crack length summary on CT6

Line	Length of each crack tip (mm)				
1	13.35	17.08	24.7	29.41	33.84
2	14.00	17.19	24.76	30.11	34.49
3	14.05	17.18	24.86	30.27	34.65
4	13.78	16.86	24.49	30.22	34.81
5	13.68	15.73	23.73	29.84	34.54
avg	13.77	16.81	24.51	29.97	34.47
cal	13.7	16.92	25	30.57	35.08
a/W	0.618	0.658	0.759	0.830	0.889
Error %	-0.10	0.21	0.84	0.94	0.89

Error=$(a_{cal}-a_{avg})/(a_{notch}+a_{avg})\times 100\%$, a_{notch} =33.8 mm

The details of complicance method is as follows [58]. First the slope of the loading and unloading portions are recorded. Because of the presence of the plasticity, the curve of load vs COD will not be linear especially for the high-load end of loading part and low-load end of unloading part. So the plastic part of the curve must be eliminated. The slope of the loading part is obtained by the linear fitting of the first half of loading data and the slope of the unloading part is obtained by fitting the first half of unloading data linearly, so as to eliminate the influence of the possible plasticity. However, there is still difference between the loading and unloading slope.

A complete trial loading-unloading cycle was recorded to confirm this. The sample CT6 with 48.7 mm crack length was loaded up to 900lb and stress intensity at the crack tip is 37.8 MPa√m. There is no significant plastic deformation at the crack tip (r_p~7 mm for bulk material) and neither load-displacement curve tends to curve much, as shown in Fig. 3- 7 (a) below. All the data points acquired seem to be in a line and the linear fitting slope from the whole loading range is 53337, which is P/COD. If the linear fittings were done separately on two halves, there is difference between the slopes as illustrated in Fig. 3- 7 (b) and (c). Fig. 3- 7 (b) is the loading portion from 0lb to 450lb and the fitting slope is 54725, while the data above 450lb gives a lower slope 52384. The overall slope lies in the middle and is close to the average of the two portions. Though no evident curvature of the loading plot, the slope of upper portion tends to be lower than that of initial loading portion, indicating the presence of plasticity at the crack tip, since there is always plasticity at the crack tip no matter what the stress intensity is.

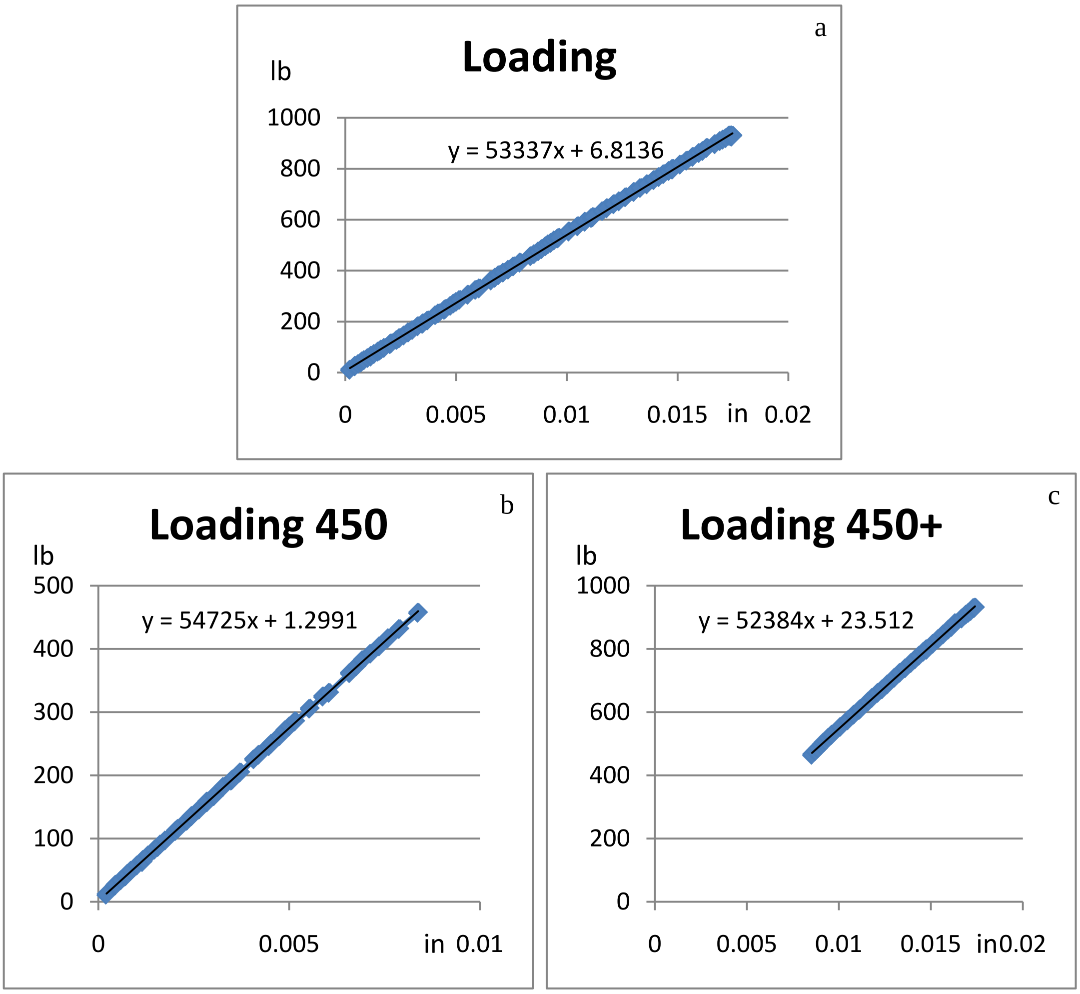

Fig. 3- 7 Load profile of CT6. (a) whole loading profile, (b) lower loading part from 0 to 450 lb, (c) upper loading part from 450 to 900 lb

Then the unloading part of the sample was analyzed as well. The overall slope is 54034 which is in the middle of upper unloading part 54824 and 52781 of lower unloading part. The upper unloading portion is stiffer than the lower one. What is more important is upper unloading portion gives a higher slope than lower loading portion. Therefore, in further calculation, the slope from upper unloading portion is consistantly used. The residual COD due to plasticity is calculated by the linear fitting equation in order to calibrate the true COD during the test. The calculation from the loading portion is taken as a reference in case there is significant crack growth during the test.

The recipocal of the slope multiplied by the thickness and Young's modulus of the sample defines the normalized compliance of the specimen. Equation (3.1) relates the normalized crack length to the elastic normalized compliance for WOL specimen at the front face [11].

$$a/W = C_0 + C_1 U_x + C_2 (U_x)^2 + C_3 (U_x)^3 + C_4 (U_x)^4 + C_5 (U_x)^5 \tag{3.1}$$

where

$$U_x = f\left(\frac{BEV_x}{P}\right)$$

$\left(\frac{BEV_x}{P}\right)$ is the normalized compliance and C are the regression coefficients for X=-0.25 (front face) listed in Table 3- 3. The transfer function f is employed to facilitate fitting a wide range of compliance values corresponding to $0.2 \leq a/W \leq 0.975$. The optimum fit was suggested as following function:

$$U_x = \frac{1}{\left(\frac{BEV_x}{P}\right)^{1/2} + 1} \tag{3.2}$$

The predicted a/W values from the previous equations are within ±0.0005 of the actual values.

Table 3- 3 Coefficients for crack length calculation

Symbol	C_0	C_1	C_2	C_3	C_4	C_5
Coefficient	1.0021	-4.9472	35.749	-649.85	4110.9	-8410.8

3.3.2 COD calculation

Crack opening displacement calculation was carried out first before wedge fabrication. In order to determine the wedge thickness, target COD at the load line must be taken into consideration. It is necessary to know the accuracy of the method in order to design the wedge.

If COD can be estimated accurately enough, then the stress intensity at the crack tip can be known. The relationship between COD and stress intensity can be derived from equation (2. 2) and (3.1). Stress intensity is a function of load and crack length. Load and COD are connected with each other by normalized compliance, while compliance is a function of crack length given by equation 3.3. The fitting constants of equation 3.3 for different locations on WOL sample are summarized in Table 3- 4 [11]. Therefore, according to the target stress intensity and known crack length, normalized compliance and load can be calculated, and then target COD is obtained. Reverse previous calculations, actual stress intensity with certain wedge thickness can be known. Therefore, The accuracy of COD calculation of given target K is important for wedge thickness design.

$$\frac{BEV_x}{P} = \left(1-\frac{X/W}{a/W}\right)\left(\frac{1+a/W}{1-a/W}\right)^2\left[b_0+b_1(a/W)+b_2(a/W)^2+b_3(a/W)^3+b_4(a/W)^4+b_5(a/W)^5+b_6(a/W)^6+b_8(a/W)^8\right] \qquad (3.3)$$

Table 3- 4 Constants for wide range elastic compliance expressions for WOL specimen

X/W	b_0	b_1	b_2	b_3	b_4	b_5	b_6	b_8
0 (LL)	0.63670	41.438	-181.26	527.8	-992.19	1029.5	-468.52	46.596
-0.2549	4.3838	-37.588	359.68	-1319.5	2506.8	-2577.0	1203.5	-136.40

Since both load and COD can be obtained from our software, the accuracy of this COD calculation can be compared with the actual data. However, in this study the COD calculation can only be verified indirectly. The COD for the wedge design is at load line, yet COD can be obtained from the sample is at front face. The locations of COD measured and applied are different so the coefficients for calculations cannot be the same but the general idea stays. Sample CT5 (only carburized) is used in this inspection. Two locations were used, -0.2549 is the nominal position of front face and -0.2795 is taken knife edge thickness (2.5 mm) into consideration.

Results in Table 3- 5 clarify the difference between acquired COD and calculated values that the difference is quite small with the absence of serious plasticity. The difference further decreases as knife edge thickness is taken into account. Besides, the verification tests are done in other samples and the results are similar. If stress intensity is high enough at the crack tip, the calculated values deviate from the linear elastic regime due to the pronounced plastic deformation. The acquired COD is always larger than calculated data due to the presence of plasticity. In this study, target stress intensity is around 40 $\text{MPa}\sqrt{\text{m}}$ and the plasticity at crack tip is appreciable. The stress intensity calculation is done by removing the plastic COD from the total COD, ensuring the equations applied to elastic regime are still valid.

Table 3- 5 COD calculation on CT5

Load lb	COD ”	X/W=-0.2549*	Calculated COD ”	%**	X/W=-0.2795*	Calculated COD ”	%**
93.7	0.00175	125.45	0.00170	-3.0	128.00	0.00173	-1.1
94.6	0.00175		0.00172	-2.1		0.0018	-0.1
578.3	0.01067		0.01049	-1.7		0.01070	0.25
590.2	0.01087		0.01070	-1.6		0.01092	0.43
598.4	0.01102		0.01085	-1.6		0.01107	0.44
605.5	0.01116		0.01098	-1.7		0.01120	0.35
899.4	0.01682		0.01631	-3.1		0.01664	-1.1
901.8	0.01686		0.01635	-3.0		0.01668	-1.1
901.2	0.01686		0.01634	-3.1		0.01667	-1.1

*Calculated normalized compliance at certain position

**Error=(CODcal-CODmeasure)/CODcal

All in all, the result indicates the calculated COD is close enough, because the accuracy for wedge fabrication is limited to 0.0005”, which is similar to the difference read from the table.

3.3.3 Wedge Preparation

Fig. 3- 8 is the sketch of wedge employed in this study. There are three dimensions designed for the wedge, thickness (B), length (L) and width (W), in which B and L are crucial. When stuck in

the WOL sample, illustrated in Fig. 3- 5, thickness of the wedge will determine the load applied on the sample and thus stress intensity factor. Length of the wedge fixes the loading points on the load line (line through the two centers of pin holes) as long as the wedge and sample keep flat at the front face. However, in order to be confident about the stress intensity at the crack tip when wedge is in position, the sensitivities of stress intensity to wedge thickness and length need to be clarified before the wedge fabrication.

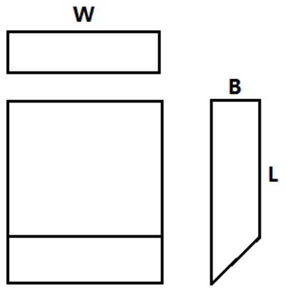

Fig. 3- 8 Schematic of wedge configuration

3.3.3.1 Wedge thickness tolerance

H6, which is previously carburized and hydrogen-charged, is used to elucidate the wedge dimension tolerance. The configuration of H6 is listed in Table 3- 6. First thing to do is to measure the slot width, which is labeled as N in the sample sketch. The nominal slot width is 5.1 mm but the measured width for H6 is 4.76 mm. The tolerance calculation procedure is as follows.

Table 3- 6 H6 configuration

Crack length	Thickness	Width	Slot width
36.0 mm	6.27 mm	76.3 mm	4.76 mm

The normalized compliance of the sample is readily available when the sample crack length is determined, which is 39.343 (BEVx/P). Load is negatively correlated with COD in the condition of fixed compliance. Because 40 MPa√m is desired, load required at load line can be calculated accordingly and thus COD is fixed. Furthermore, the wedge thickness can be determined. The thickness of wedge is comprised of the width of slot, the target COD so far. The calculation result is summarized in Table 3- 7. Results reveal even 0.0127 mm (0.0005”) deviation from target thickness, the stress intensity fluctuates more than 2 MPa√m. If deviation is 0.0254 (0.001”), the variation is around 4 MPa√m. Therefore, the stress intensity is pretty sensitive to the wedge thickness. The tolerance during fabrication is only around 0.0005” so the fabrication is important to ensure the design work. The thickness tolerance is approaching the limit of fabrication.

Table 3- 7 Wedge thickness tolerance

COD (mm)	B (mm)	Deviation (mm)	Load (lb)	K (MPa√m)
0.2357	4.9957	0	1632	40
0.2489	5.0165	0.0127	1723.3	42.3
0.2616	5.0216	0.0254	1811.2	44.4
0.2235	4.9835	-0.0127	1547.3	37.9
0.2108	4.9708	-0.0254	1459.4	35.8

3.3.3.2 Wedge length tolerance

Similar calculation was done on the wedge length tolerance. The nominal distance from front face to load line is 18.8 mm. As a result, if the length is the same to that distance, then the load can be applied at load line the same as the pins do. However, the tolerance of the length needs to be considered as well. H6 is still used as example.

The sketch below, exaggerated, illustrates the ways of considering the length tolerance. The red line is the load line. If the wedge is misplaced, either sliding in or out, the actual COD at load line will change correspondingly. If wedge slides in a little bit, COD at load line will be larger than expected. Otherwise, COD at load line is smaller than expected. As target K is 40 MPa$\sqrt{m}$, the calculated wedge thickness at load line is 4.9957 mm. If wedge with this thickness misplaces from load line, the delta COD can be calculated on the ground of geometry.

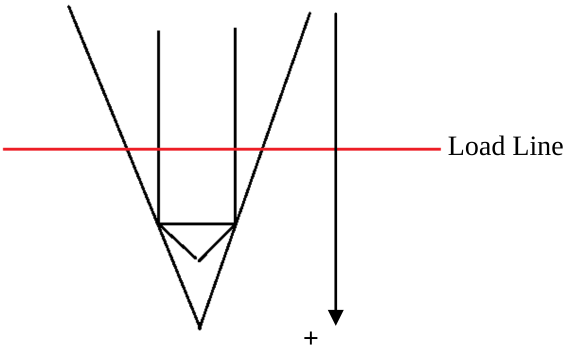

Fig. 3- 9 Sketch for wedge misalignment with load line

The result summarized in Table 3- 8 signifies deviation of 0.0254 mm (0.001”) only gives 1

MPa√m rise from the target stress intensity. Compared with the result of 0.0127 mm (0.0005”) deviation from designed thickness, the stress intensity is not as sensitive to length as thickness.

Table 3- 8 Calculation for the influence of wedge misplacement from load line

misplacement (mm)	ΔCOD (mm)	Load (lb)	K (MPa√m)
0	0	1632	40
0.0254	0.00305	1705.8	41.8
0.127	0.0153	1793.8	44
0.254	0.0305	1899.3	46.6
-0.0254	-0.00305	1670.7	41.0
-0.127	-0.0153	1582.7	38.8
-0.254	-0.0305	1477.2	36.2

The width of wedge is much easier to determine. The width is chosen to be 0.75 inches in order to be easily handled. The angle at the wedge tip is 45° which is not very important.

3.3.3.3 Trial tests by drill rods

As a part of wedge design, in order to get a general idea of the actual situation of wedge test, several trial tests were carried out by using drill rods to simulate the wedge. Drill rods with diameter 0.19”, 0.1945” and 0.197” were used in the trial tests. Though the tests were done under load and displacement control separately, all these tests yielded similar results. The loading slope signifies the compliance. The unloading slope with rod in is far from a vertical line to x-axis, indicating the rod is not ideally stiff but compressed by the load applied by the arm of the sample.

One typical data plot is shown in Fig. 3- 10, in which the loading slope is 54660 and unloading slope with drill rod in it is 293886. The unloading slope is much higher than the compliance slope. In this case, ideally, the drill rod is contact with the sample infinitely small so the stress induced from the applied load is high. Nevertheless, there is no sign of plasticity around the contact area either on the sample or on the drill rod. Moreover, the wedge contacts with sample in relatively large area due to the flat surface. Higher unloading slope with wedge in should be expected. Still extra thickness due to this slope should be taken into consideration.

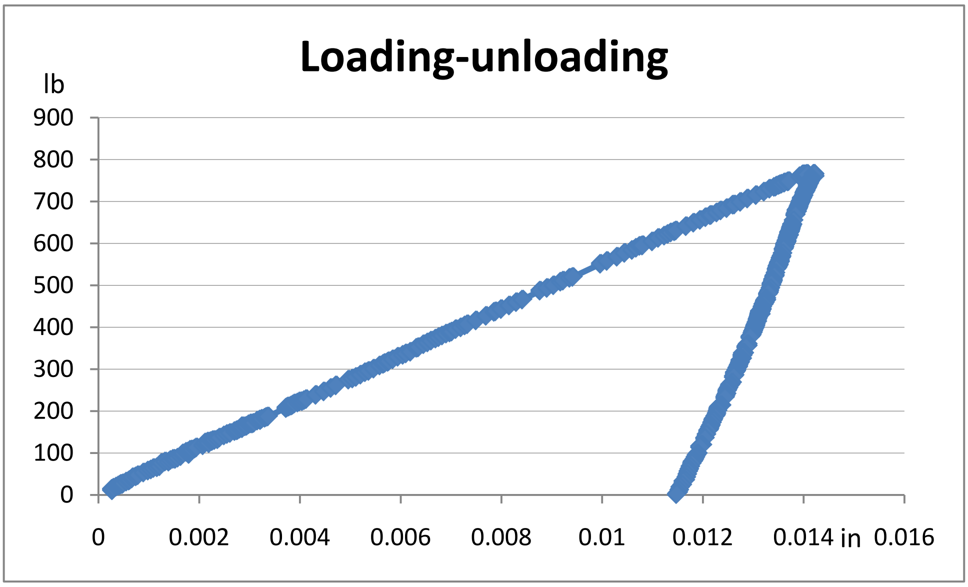

Fig. 3- 10 Loading-unloading profile of sample with drill rod of 0.197”

3.3.3.4 Wedge thickness determination

Consequently, the total thickness of wedge consists of three parts: slot width, target COD and some extra thickness for the elastic compression. From testing results later, the unloading slope with wedge is indeed higher than that with drill rod and typically around 900000.

Because all the pristine samples were nearly the same configurations, like precrack length, sample thickness, width etc, it is easier to decide the wedge thickness. Based on target stress intensity, the target COD at load line can be calculated. Table 3- 9 summarizes the predicted stress intensity on four samples, by setting the target stress intensity on sample H6 and H7. The difference on the predicted stress intensity is due to the different slot width at the load line, which can be measured. By adding some extra COD, on the ground of higher slope than drill rod tests assumption, the final wedge thickness is decided to be 5.00mm (0.197”). To insure the target stress intensity can be achieved, a thicker wedge with the thickness of 5.08 mm (0.200”) was fabricated at the same time. The actual received wedge thickness are 5.01 mm (0.1971”) and 5.083 mm (0.2001”), measured by screw micrometer.

Table 3- 9 Calculated stress intensity for wedge test on different samples

Name	Slot width at LL (mm)	COD (mm)	Thickness (mm)	Load (lb)	K (MPa√m)
H4	4.75	0.2457	4.9957	1701.1	41.7
H5	4.73	0.2657		1839.6	45.1
H6	4.76	0.2357		1632	40
H7	4.76	0.2357		1632	40

Crack length a=35.8 mm, sample thickness B=6.27 mm, sample width W=76.25 mm

3.4 Wedge testing procedure

Before the test, COD at the front and load line were estimated according to the slot width and the thickness of the wedge. Therefore target load for stress intensity can be obtained. Then the COD gauge was zeroed at the sample front face when 100 lb was applied. Tests were carried out under displacement control.

During the test, sample was loaded up as slowly as possible, until the opening of the sample front face is large enough to squeeze the wedge in. The load, COD and displacement are monitored all the way. When the COD is stable at that load, take the gauge off. Tap the wedge in; make sure the wedge back is flat with the sample front face, ensuring the applied load from the wedge is on the load line. COD gauge was put back on afterward. The sample was unloaded and taken off from the machine. From COD obtained at the end of test, final stress intensity can be estimated. The precise stress intensity can be calculated after subtracting plastic COD from total COD, which can be done after the removal of wedge from the sample.

Because the COD gauge at the front face need to be removed from the sample in order to tap the wedge in and put back on later, the consistency of COD gauge needs to be verified before the test. The gauge was put on a reference sample with a pair of glued knife edges. The gauge was zeroed first, then removed from the sample and put back on later. The COD value was recorded each time when gauge is on the sample. Six successive values were recorded and summarized in Table 3- 10 below.

Table 3- 10 Successive readings from COD gauge

Initial reading	1	2	3	4	5	6
0	-0.00003	-0.00005	-0.00008	-0.00010	0.00005	-0.00006

The COD readings did not deviate from origin zero too much and it is about one order of magnitude smaller than the tolerance of the wedge thickness. The stress intensity variation with this magnitude fluctuation of COD is less than 0.5 MPa√m. During the trial tests, it is noticed the parallelism of the knife edges are crucial to minimize the variation. If the parallelism is good, less variation of COD value is observed. Perfect parallelism of knife edges is never practical. So it is better to fix the position of the gauge clip with respect to knife edges. These procedures will mitigate the variation of COD values when the gauge is put off and on.

4. Results

4.1 Constant loading tests

Tests under load control were done on sample H2 first, which is only hydrogen-charged without carburization. Table 4- 1 is the loading parameters for the sample H2. Loading profile over time is shown in below (Fig. 4- 1). The tests lasted for more than 100 h. The load is nearly constant over the 100 h duration but the COD increases over time. The increase of COD over time indicates the activity of plastic zone. Sample does not respond to the load fully in the beginning but gradually deformed instead.

Table 4- 1 Loading parameters of sample H2

Crack length	Load	K	Plastic zone size
44.8 mm	2160 lb	77 MPa√m	8.9 mm

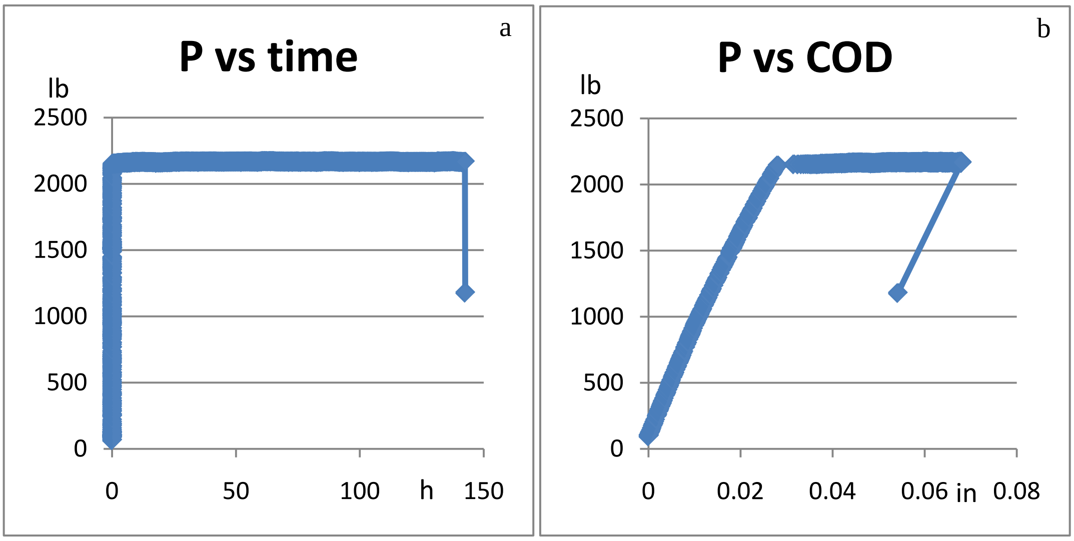

Fig. 4- 1 Loading profile of sample H2 (a) Load vs time and (b) Load vs COD

Fig. 4- 2 is the crack tip after test without any load on it. It can be easily seen the crack tip blunts severely due to the high stress intensity. The dark area extends from crack tip is seriously deformed material within the plastic zone. Such heavy plasticity rules out the possibility of brittle crack extension.

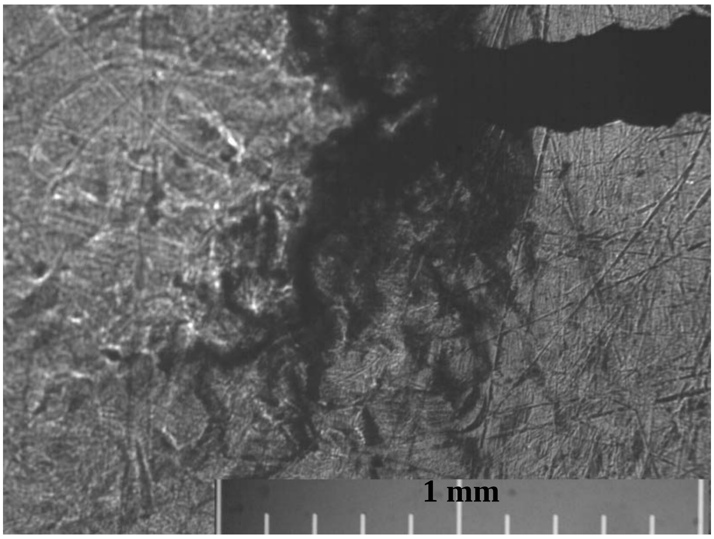

Fig. 4- 2 Sample H2 after test

Because no cracking happens on H2, which was tested under high stress intensity with severe plasticity, sample H3 was tested under a lower stress intensity condition. The test parameters were listed in Table 4- 2. Fig. 4- 3 is the loading profile. The duration of the test is 95 h. The load is stable during the whole test and the COD does not vary a lot, implying no large plasticity at the crack tip. In this case, no obvious plasticity can be seen at the crack tip. However, still no new crack extension can be observed. The crack tip after test was displayed in Fig. 4- 4. Though no severe plasticity present, some residual crack tip opening can be seen at the crack tip, yet it is much smaller than that of sample H2. The significance of the tests on H2 and H3 is the hydrogen cannot embrittle 316L stainless steel.

Table 4- 2 Loading parameters of sample H3

Crack length	Load	K	Plastic zone size
46.2 mm	1036 lb	38 MPa√m	2.1 mm

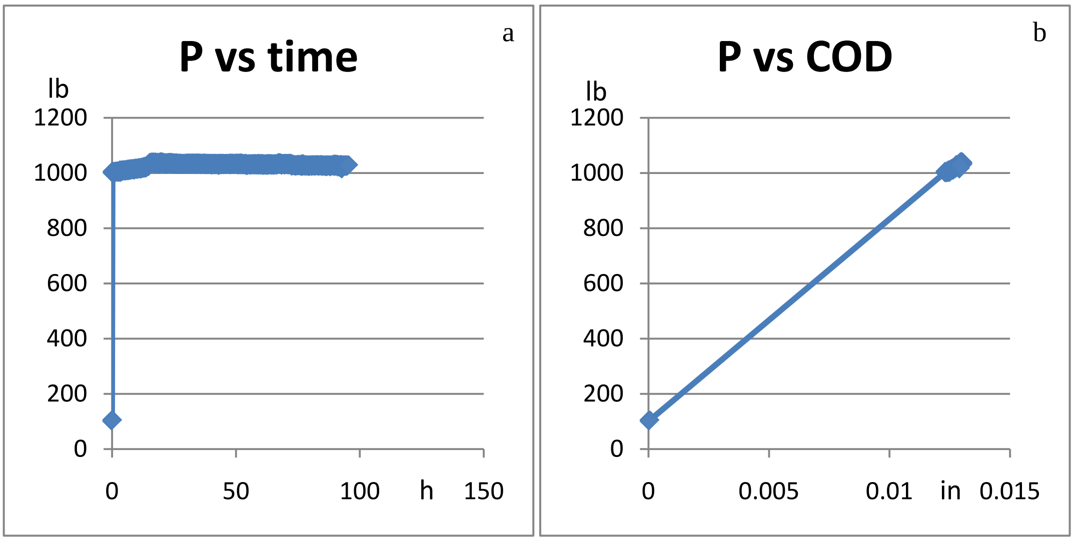

Fig. 4- 3 Loading profile of sample H3 (a) Load vs time and (b) Load vs COD

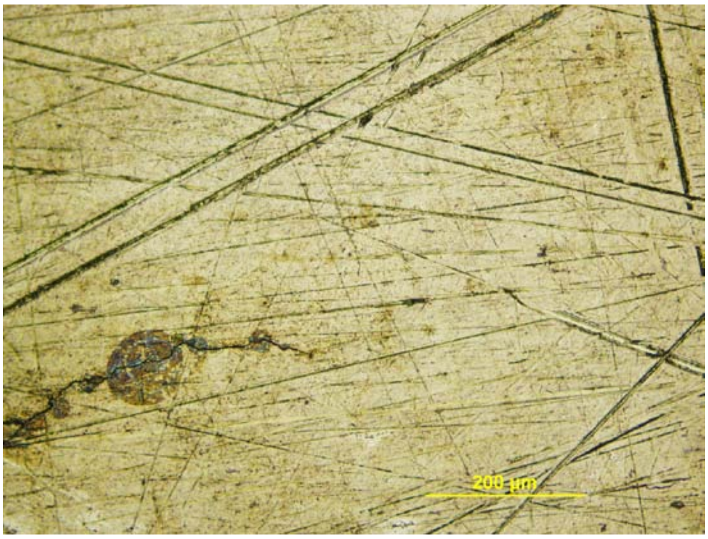

Fig. 4- 4 Crack tip of sample H3 after the test

The following test is on H6, which is hydrogen charged and also carburized. The loading parameters and profiles are summarized in Table 4- 3 and Fig. 4- 5, respectively. The load is stable and some increase of COD during the test is owing to the plasticity at the crack tip. At the target K of 40 MPa√m, appreciable plasticity at crack tip can be identified and characterized. The most valuable finding is the crack did extend during the test, which can be easily confirmed by comparing crack tip before and after test (Fig. 4- 6). Not only the main crack propagates, but also there are several minor cracks newly emerged from surface defect.

Table 4- 3 Loading parameters of sample H6

Crack length	Load	K	Plastic zone size
36.0 mm	1650 lb	40 MPa√m	2.5 mm

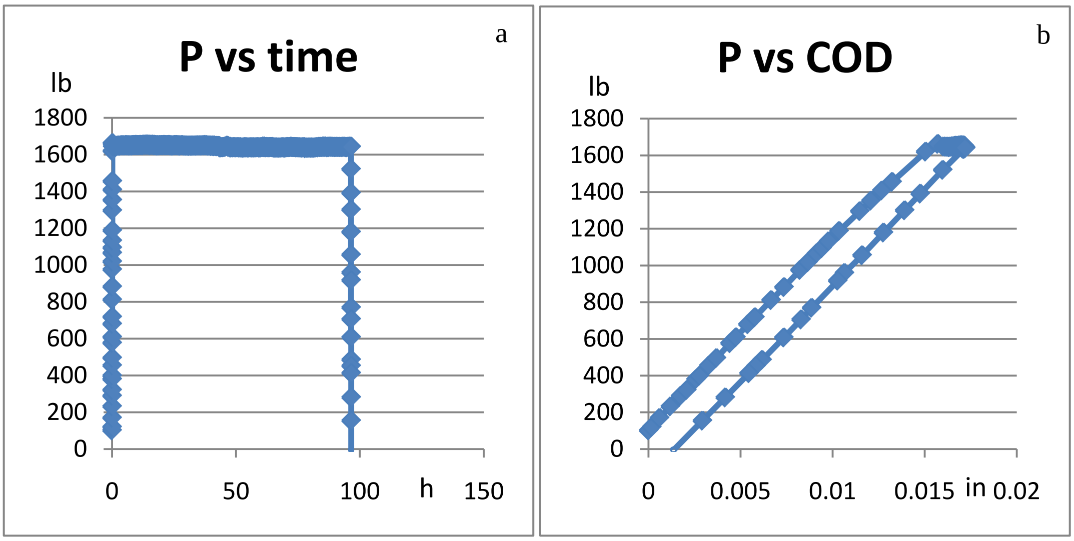

Fig. 4- 5 Loading profile of sample H6 (a) Load vs time and (b) Load vs COD

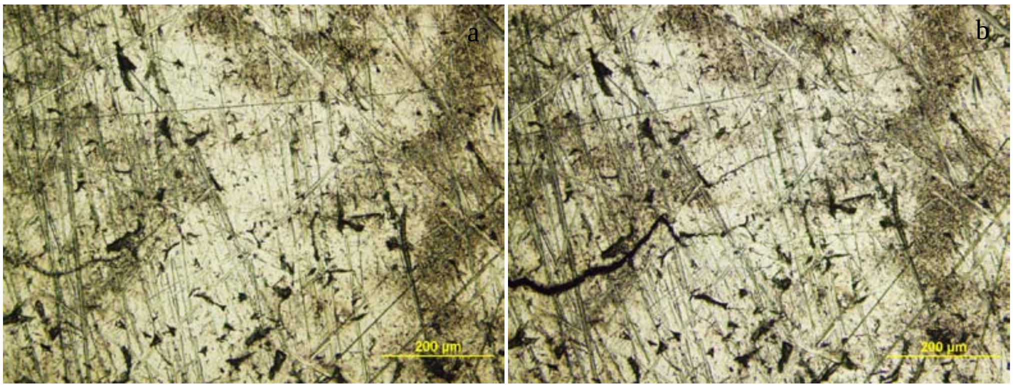

Fig. 4- 6 Crack tip of sample H3 before (a) and after (b) the test

The new crack extension is only around 150 μm, which is very small. The loading and unloading slopes of the sample H6 are nearly the same. The crack extension calculated accordingly (Table 4-4) was within the range of uncertainty of compliance method as previous stated. This calculated crack extension may be due to the blunting of crack tip as well. On the ground of H2 and H3 tests results, this cracking probably occurs within the case depth. The high residual stress within the case can be the reason of cracking.

Table 4- 4 Slope and calculated crack length for sample H6

H6	Slope	Crack length
Loading	107045	37.3 mm
Unloading	104759	37.7 mm

4.2 Wedge test

After constant load testing, there are still some questions need to be answered, like the initiation and propagation of the crack. With the help of the wedge, the sample can be removed from the machine and observation over time is possible.

The dimension and test parameter of sample H7 is listed in Table 4- 5. Achieved stress intensity is close to that of the sample H6. The complete loading profile is shown in Fig. 4- 7. During the loading, the slope is related with the compliance of the sample. Then the wedge is tapped in. As the wedge was pounded into the sample, it transferred part of the load onto itself. Since the system is under displacement control, there is some load drop during the tapping. The negative COD during the sample tapping-in is because the COD gauge was moved on a reference sample, whose COD is smaller than initial H7 COD. When wedge is pounded to be flat with the sample front face, the load is taken off. The slope from a wedge is much steeper than that from a drill rod. This is ascribed to the contact area of a wedge being much larger than that of a drill rod. Thus, the stress induced by load on wedge is smaller and the COD retraction is smaller under the same load compared with that of drill rod.

Table 4- 5 Loading parameter of sample H7

Crack length	Wedge thickness	COD	Load	Stress intensity
35.92 mm	5 mm	0.367 mm	1675 lb	41 MPa√m

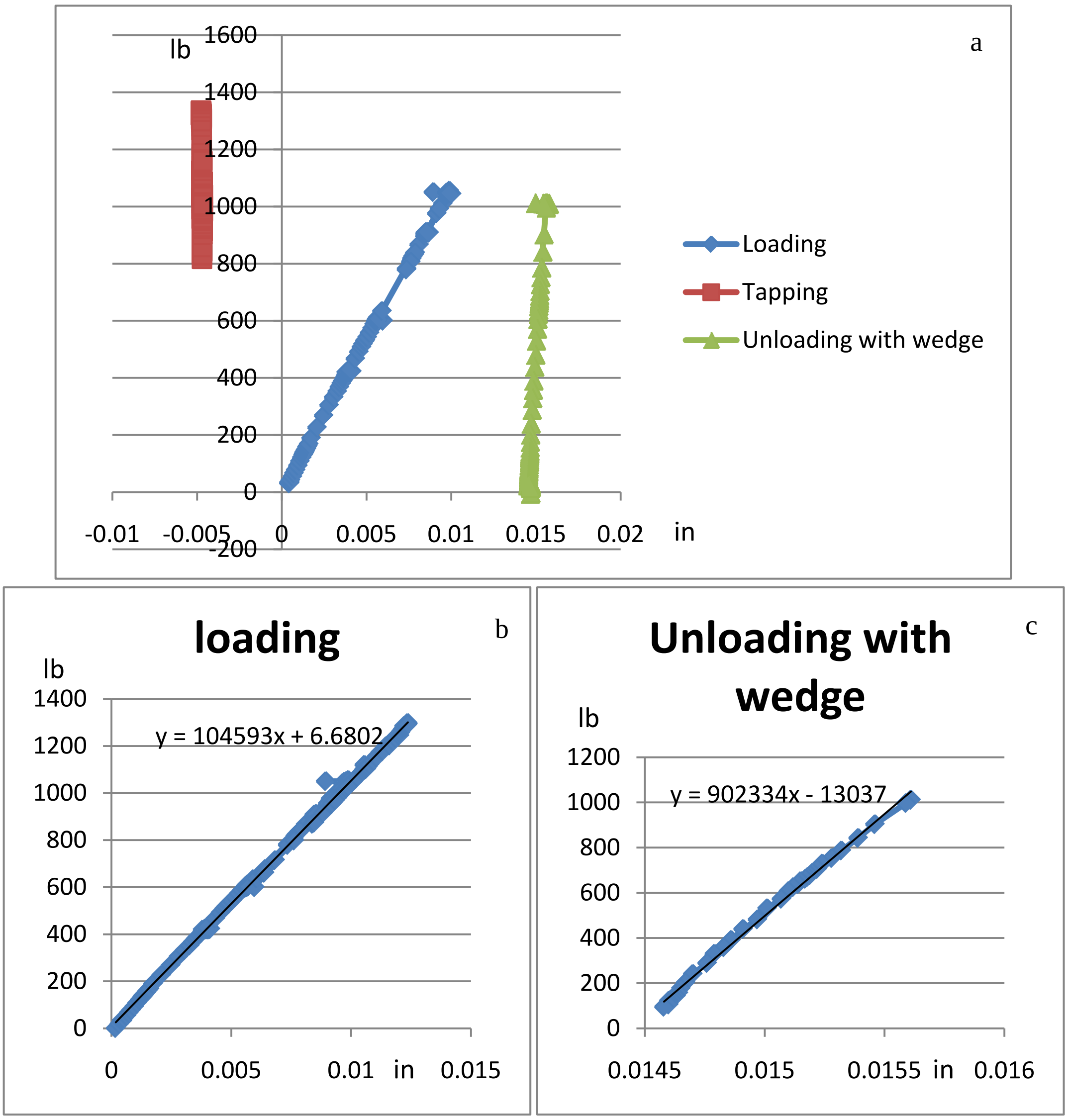

Fig. 4- 7 Loading profile for sample H7 (a) whole procedure (b) loading slope and (c) unloading slope

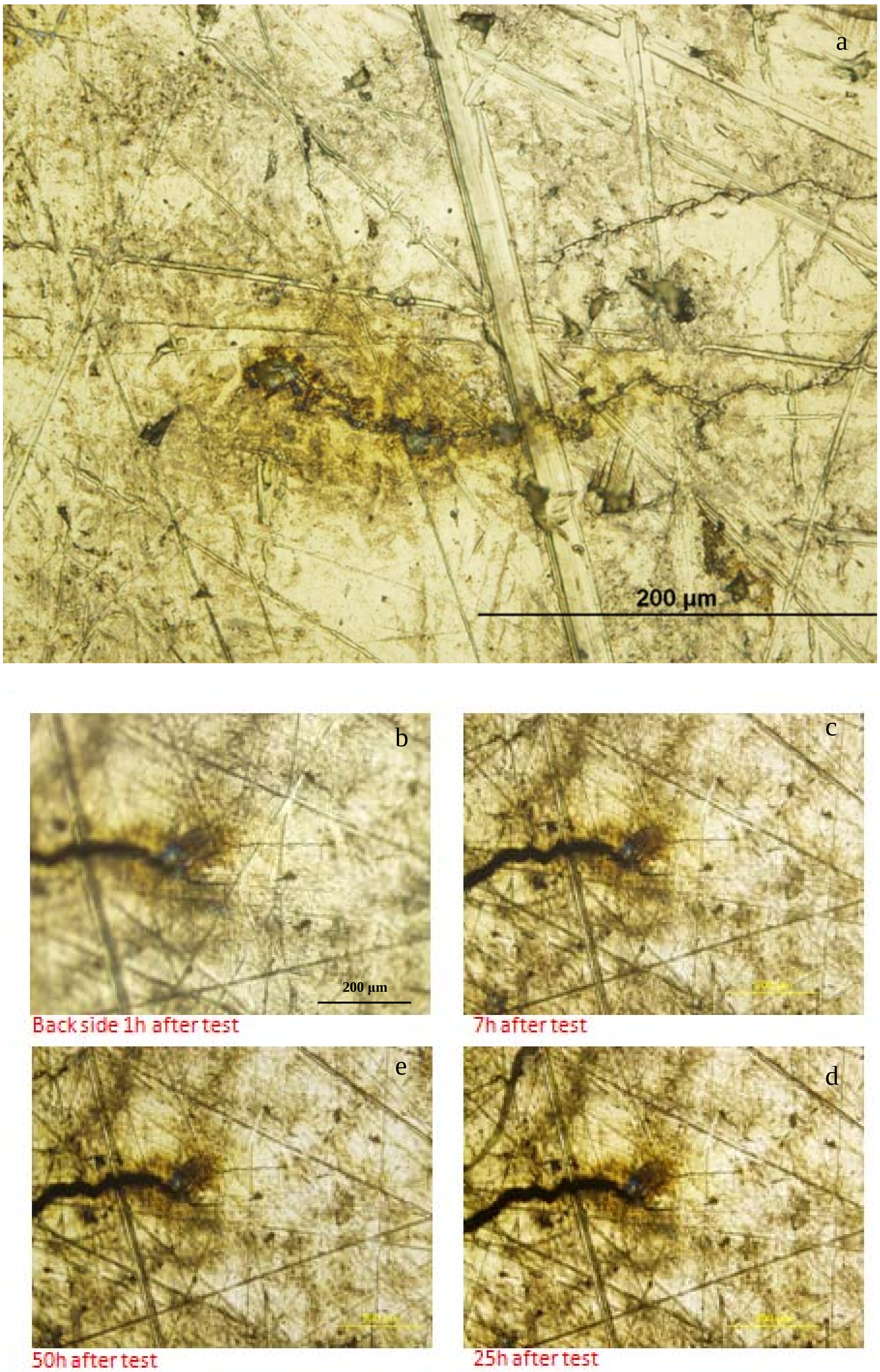

Fig. 4- 8 Crack tip of sample H7 (a) before test (b) 1 h, (c) 7 h, (d) 25 h and (e) 50 h after test

Fig. 4- 8 (b) – (e) above are four pictures taken during the first 50 h after the wedge inserted in H7. Crack tip before the test is positioned for comparison. What clearly shown is the crack propagates

during the very first hour, implying the cracking occurs during the loading. No incubation time is needed for the hydrogen-induced cracking, which contradicts with conventional observation [53]. The contradiction can be ascribed to the high equilibrium hydrogen content achieved after the hydrogen charging process.

Generally, it is widely accepted that hydrogen-induced cracking happens when a critical hydrogen concentration is achieved. Some experimental and simulation results [26, 50, 59] supports this theory that the crack will not initiate or propagate until a certain critical level of hydrogen concentration is achieved. When a tensile stress is applied, some uphill diffusion of hydrogen into the stressed and plastically deformed region is expected due to the lattice expansion. Some time later, critical concentration is reached and crack will initiate or propagate. Therefore, delayed failure is observed in hydrogen induced cracking. If this is true, then the high hydrogen concentration in material can significantly reduce the incubation time or even eliminate it.

Another observation in wedge test is there is no further crack propagation after first hour. It suggests if driving force stress intensity is higher than the threshold, the crack will propagate spontaneously and immediately. However, once the driving force stress intensity descends to the threshold, crack stops propagating.

4.3 Crack depth investigation

According to the test results of sample H2 and H6, it prompts speculation that cracking is limited to the carburized layer on sample H6. Focus ion beam (FIB) milling was carried out in order to testify this supposition.

FIB cross-section was first tried on the newly merged minor cracks. The positions were exhibited in Fig. 4- 9 (a). All these three cross-section depths are within the carburization layer thickness. The two cross-section depths on the same minor crack are different. The one near the crack tip is shallower, yet the one near the defect, the crack initiation site, penetrates deeper.

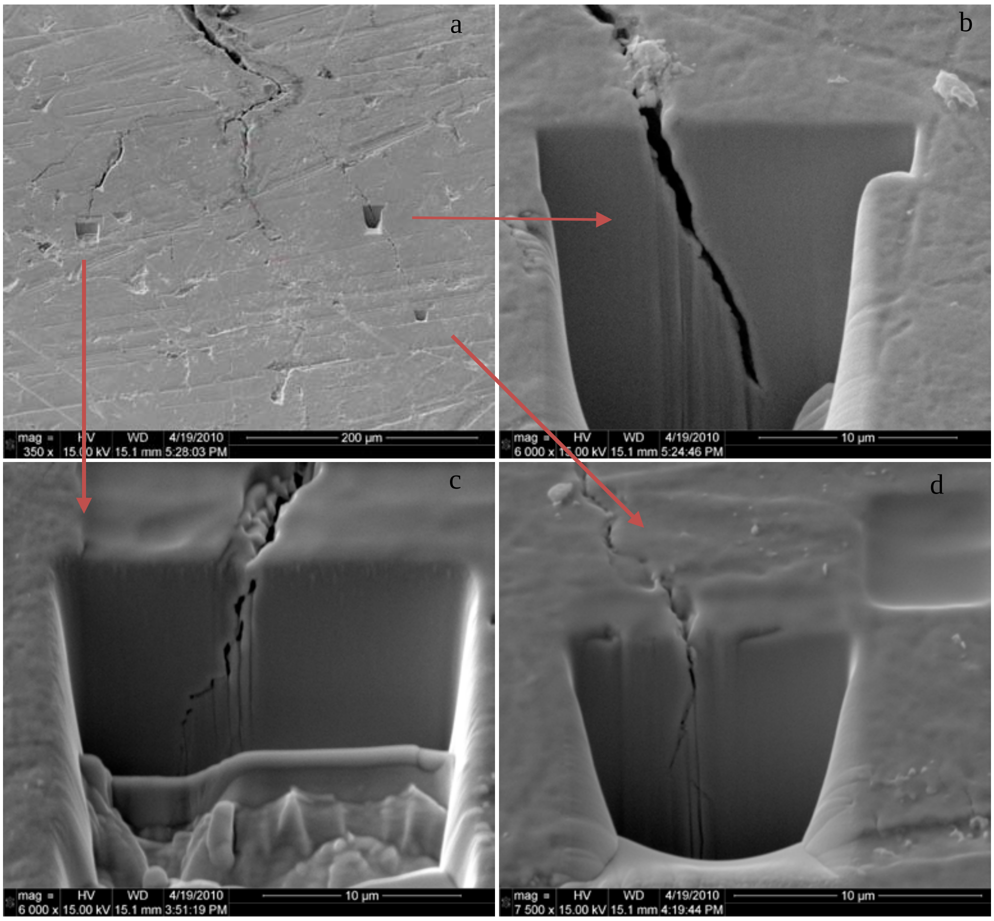

Fig. 4- 9 Cross-sections by FIB on two minor cracks of sample H6. (a) overview of three FIB cross-section positions, (b) cross-section with depth of 17.2 μm, (c) cross section with depth of 8.1 μm and (d) cross-section with depth of 10.9 μm

Similar cross-sections were done on the main crack as well. The positions of three FIB cross sections can be seen in Fig. 4- 10 (a) below. They were arranged from the original crack tip to the newly extended crack tip, numbered from 1 to 3 and shown from (b) to (d) respectively. The third cross-section was not exactly at the crack tip, because it is difficult to follow the tiny crack tip in the ion beam image.

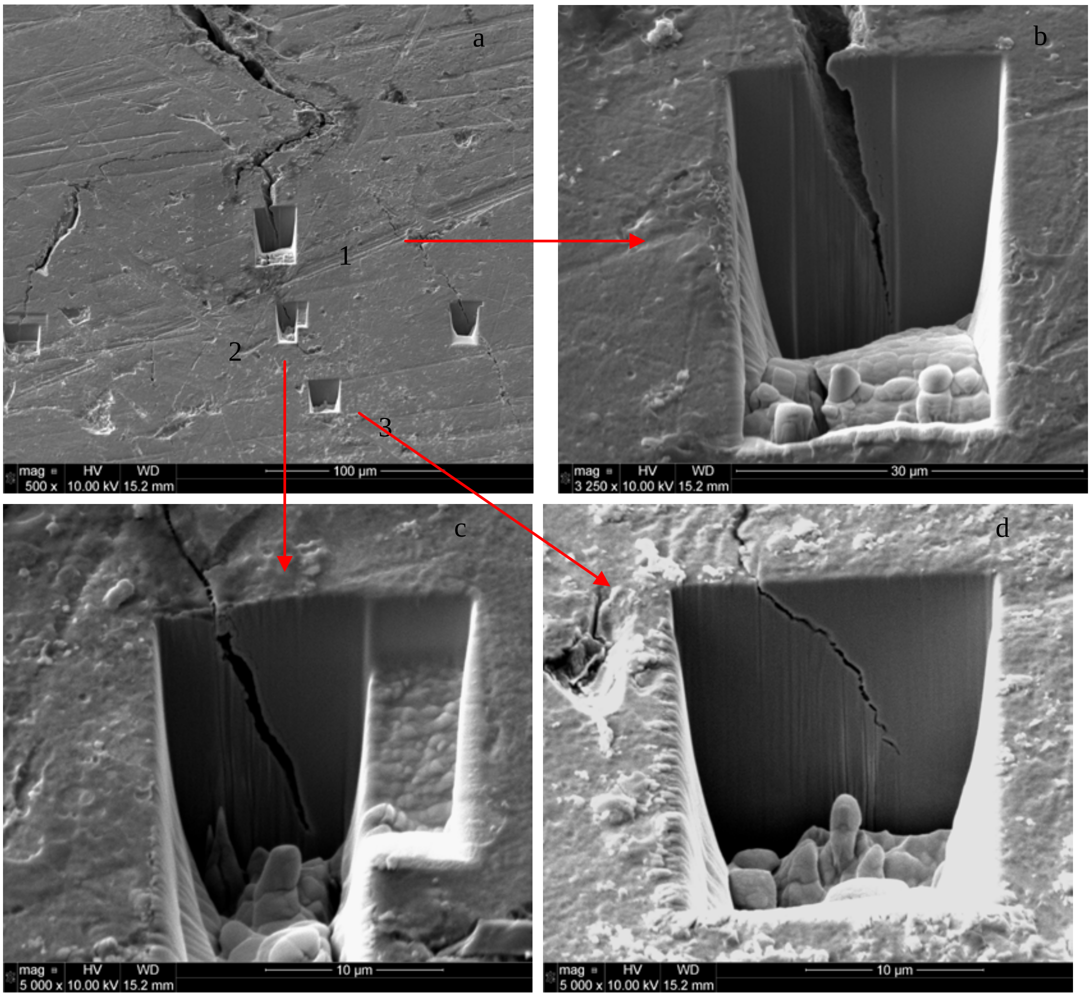

Fig. 4- 10 Three cross-sections on the main crack of sample H6

Due to the size of the sample, the sample only tilts to 40°, which is 12° deviated from the normal direction of the sample surface. Therefore the depths measured on the pictures need to convert to the true depth of crack. The schematic is shown in Fig. 4- 11.

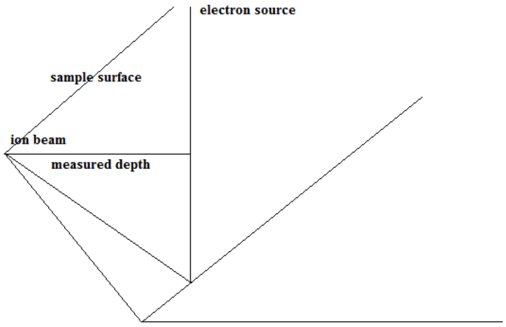

Fig. 4- 11 Schematic of actual milling depth calculation

According to the geometric relationship, the actual depth can be calculated as follows.

$$d = d_m/\cos 38° * \cos 12° \quad (4.1)$$

where d is the actual depth and d_m is the measure depth on the image. The depths of three cross sections are summarized in Table 4- 6. The crack penetrates deeper in the case as approaching the original crack tip, which echoes with the observation on the minor crack. The crack is nearly through the thickness of the case at the original crack tip. However, other two are well within the case depth.

Table 4- 6 Crack depths of three cross-sections on H6 main crack

Distance from original crack tip (μm)	Crack depth (μm)
102.7	12.5
60.3	15.7
16.2	28

4.4 Plastic zone evolution

Stress or strain field within the plastic zone is the driving force for the motion of atoms and dislocations. Diffusional creep due to the chemical potential in a stressed solid is a similar concept. If the atoms or dislocations within the zone are actually mobile, the plastic zone will change over time. Macroscopically, the COD increases over time as observed previously. It is well documented that hydrogen promotes the activity and mobility of dislocations. So when load is applied, in plastic zone, dislocations of the sample with hydrogen should have a higher mobility relative to that of the sample without. Therefore the evolution of the plastic zone in the sample with hydrogen should be more significant than the one without.

Plastic zone evolution was characterized by confocal microscope. The 3D imaging function built in the microscope is a useful tool for studying any dimension change in plastic zone. Three samples were used, B2, H4 and H5. The heat treatment history of each sample is summarized in Table 4- 7.

Table 4- 7 Heat treatment of sample B2, H4 and H5

Process	B2	CT3	H4	H5
Carburization	No	Yes	No	Yes
Hydrogen-charging	No	No	Yes	Yes

B2 as a non-treated sample is a control test sample. Wedge with the thickness of 0.2001” was inserted and 36.8 MPa√m (a=39.8 mm) is achieved at crack tip. The crack does not propagate when the wedge is in. In Fig. 4- 12, the crack tip before and after the wedge tapped in was compared. The only difference between the two is the crack tip with the wedge in it opens much wider. The stress intensity can be estimated according to the CTOD. The CTOD measured is 21.5 μm and according to the equation (2. 6. 2) the stress intensity is 36.6 MPa√m, which is pretty close to the value obtained from COD (~ 8% small). The plastic zone evolution at crack tip was recorded over time and illustrated in Fig. 4- 13. The size of the plastic zone from 1 h to 325 h barely changed. If there is any change, it is subtle. This indicates the dislocations in the plastic zone of non-treated sample are practically frozen.

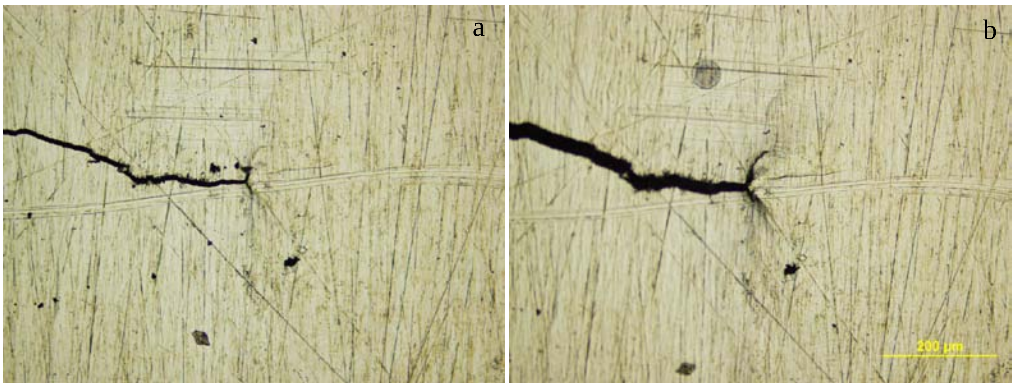

Fig. 4- 12 Crack tip of sample B2 before (a) and during (b) the test with wedge in it

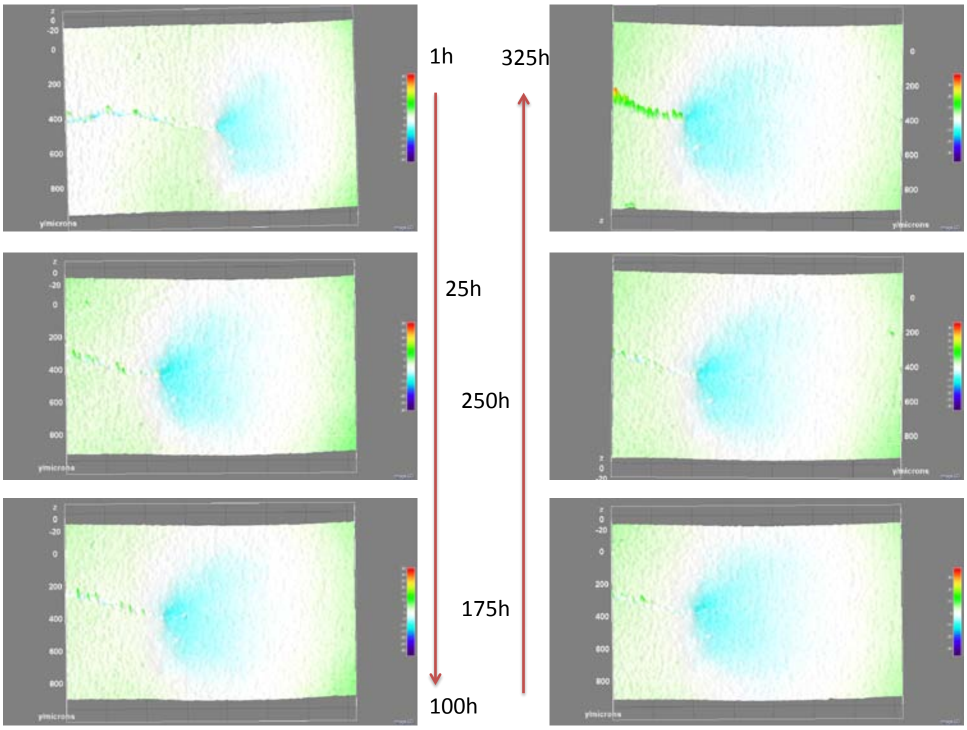

Fig. 4- 13 Plastic zone evolution of sample B2 over the time period from 1 h to 325 h

Test on sample CT3, only carburized sample, was precracked to eliminate the previous loading effect. With the help of wedge, stress intensity around 50 MPa√m is achieved. The crack tip before and during the test is shown in Fig. 4-14.

Fig. 4- 14 Crack tip of sample CT3 before (a) and during (b) the test with wedge in it

The plastic zone evolution of sample CT3 was illustrated in the Fig. 4-15. It shows the plastic zone size stays roughly the same over time, which is similar to the previous B2 result due to the immobility of dislocation under room temperature. However, the observable size on this carburized sample is comparable or even smaller than that on the sample B2, despite of higher stress intensity on sample CT3. The theoretical plastic zone size on CT3 is more than one and a half larger than that on B2. This indicates the carburized layer can suppress the plastic zone evolution efficiently at least from plan view.

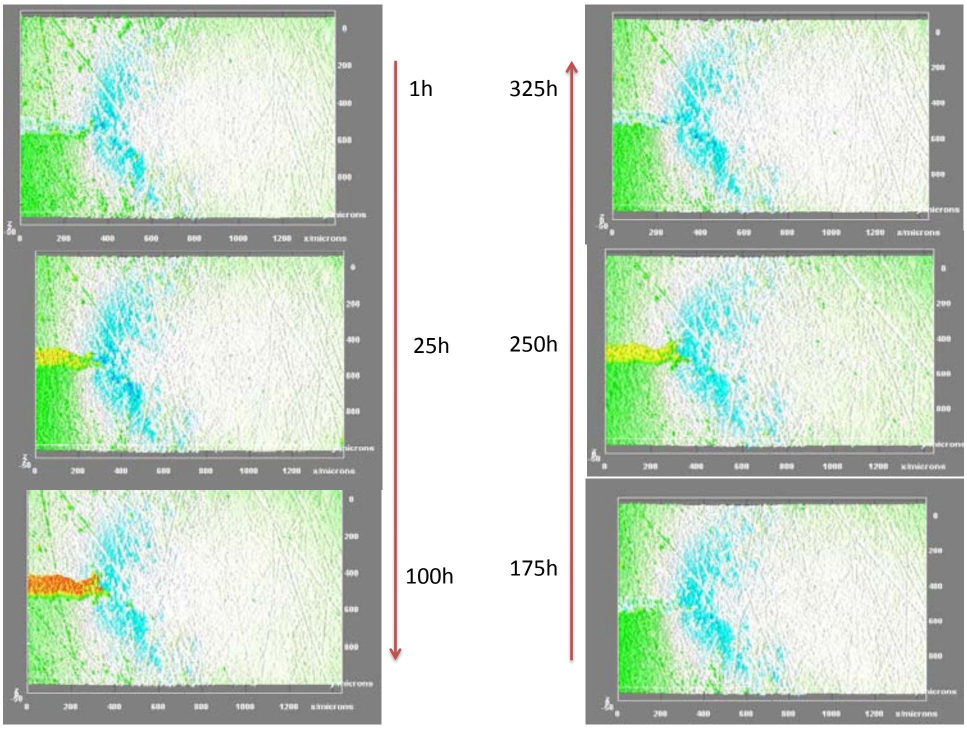

Fig. 4- 15 Plastic zone evolution of sample CT3 over the time period from 1 h to 325 h

Test on H4, without any previous loading history, was carried out afterwards with 0.1981” thick wedge. The crack tip before test was identified in Fig. 4- 16 (a). Crack tip during the test with wedge in is displayed in (b).

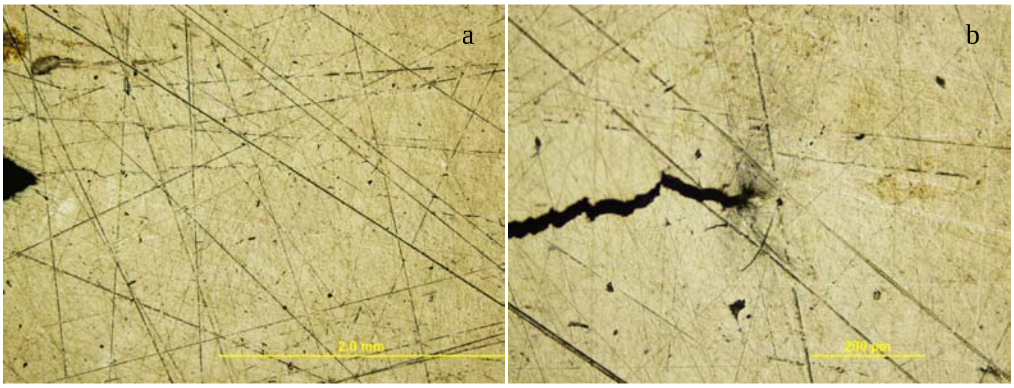

Fig. 4- 16 Crack tip of sample H4 before (a) and during (b) the test with wedge in it

The test parameter on H4 is 41 MPa√m (a=35.8 mm). It is no surprise that the crack in the sample does not propagate, same as the previous test result. 3D images (Fig. 4- 17) of crack tip over the same time period as B2 signify substantial growth of the plastic zone over this time period. The initial plastic zone is relatively small and during the first 25 h, the zone (blue region) nearly doubles its size. The depth of the plastic zone at the crack tip also varies with time. As indicated by the deep blue, the crack tip gets deeper and this deep blue area also grows over time. This implies the mobility of the dislocation is much higher than that in the sample without hydrogen. The hydrogen does facilitate the motion of dislocations, hence the plastic zone stretches out as time passes. 3D images taken after 325 h (Fig. 4- 18) suggest the plastic zone tends to be shallower over the prolonged time period. The overall plastic zone size seems to be the same but the deep blue area shrinks. The motion of dislocation finally partially relieves the strain within the plastic zone. Therefore, the plastic zone gets shallower as enough time is given for dislocations to move. But the reason of initial enlargement of plastic zone is still a mystery. The initial plastic zone deepening is possibly attributed to the easier motion of dislocations. It can be the result of competition between dislocation motion relaxation and strain build up. When load is initially applied, the motion of dislocation makes it harder to build up the deformation at the crack tip. Thus it takes longer time to reach the summit of the deformation at the crack tip. But finally relaxation can dominate the process and partially relax the strain energy.

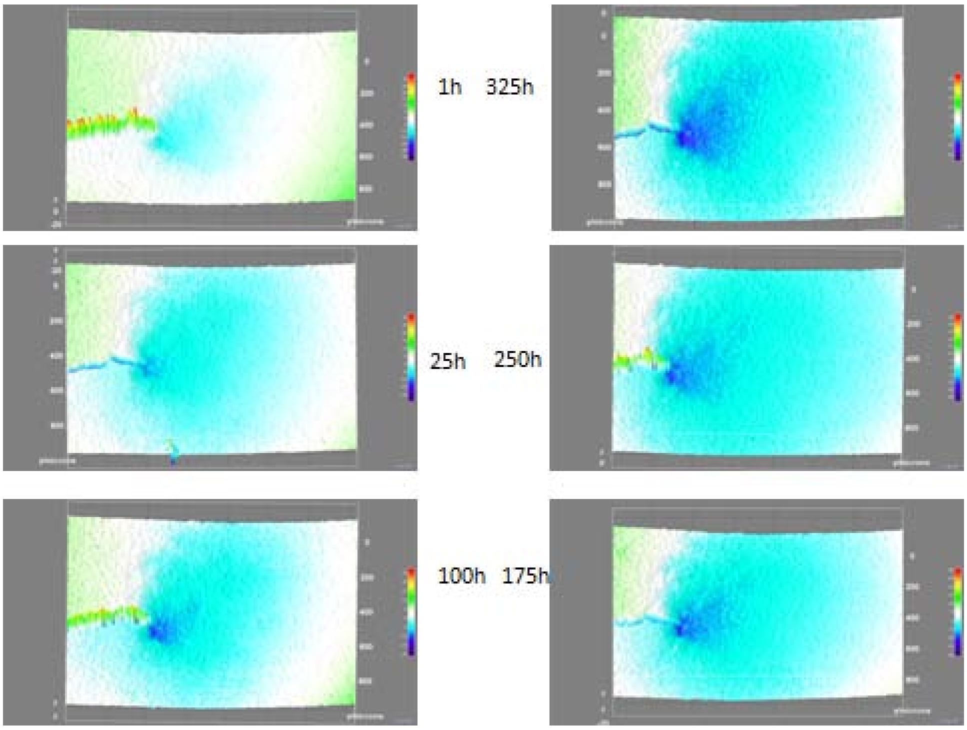

Fig. 4- 17 Plastic zone evolution of sample H4 over the time period from 1 h to 325 h

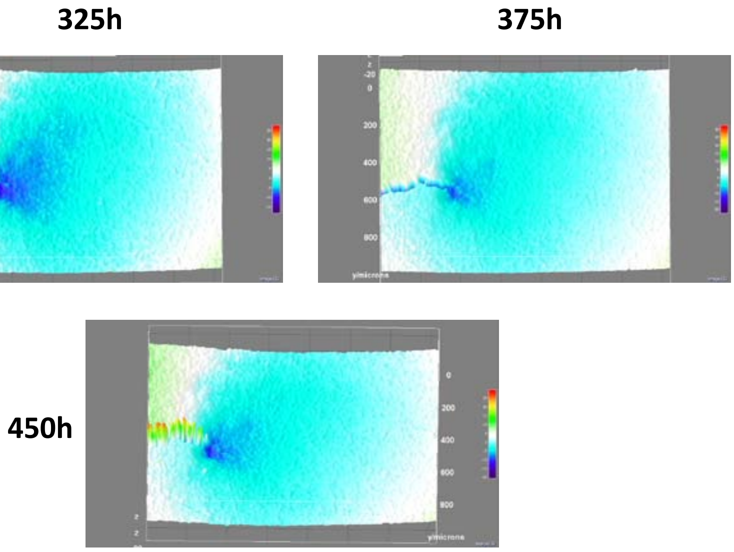

Fig. 4- 18 Plastic zone evolution of sample H4 during prolonged time

Pictures from other side of the sample, Fig. 4- 19 and Fig. 4- 20, are in a similar circumstance, which grows at the beginning and relaxes somewhat at the end. However, the sizes of the plastic zone on the two sides are slightly different because of the lower stress intensity at the side with longer crack (38 MPa√m). So the deformation on the other side is also smaller.

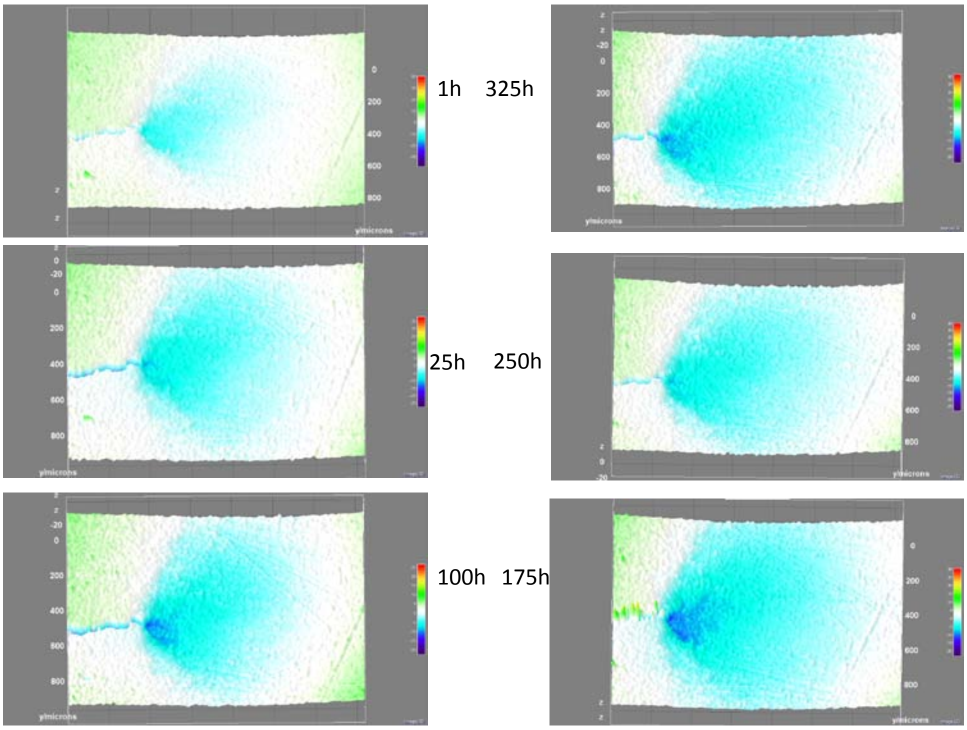

Fig. 4- 19 Plastic zone evolution of sample H4 on the other side over the time period from 1 h to 325 h

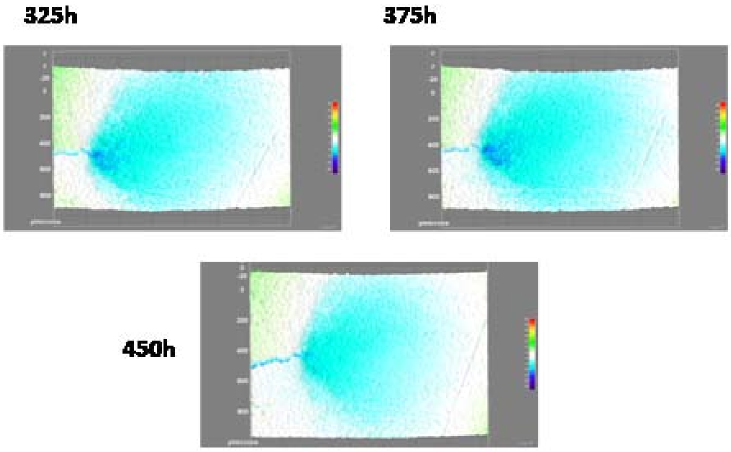

Fig. 4- 20 Plastic zone evolution of sample H4 on the other side during prolonged time

For the sample H5, on which the crack extension is observed (Fig. 4- 21), the plastic zone change over time is expected. The calculated stress intensity on H5 is 43.5 MPa√m. The plastic zone evolution result is illustrated below in Fig. 4- 22 . The plastic zone size grows at first few hours and stays roughly the same. Under the similar stress intensity to H4, the plastic zone observed on H5 is much smaller and shallower. The case is very effective to suppress the plastic zone evolution. This can be explained by the fact that the yield strength of the case is much higher than the bulk material. The plastic zone size is inversely related with yield strength. So the corresponding plastic zone size in the case is much smaller than that from bulk material as summarized in Table 4- 8. The plastic zone size observed on H5 is somewhere in between of these two extremes. The size measured from picture is around 0.8 mm.

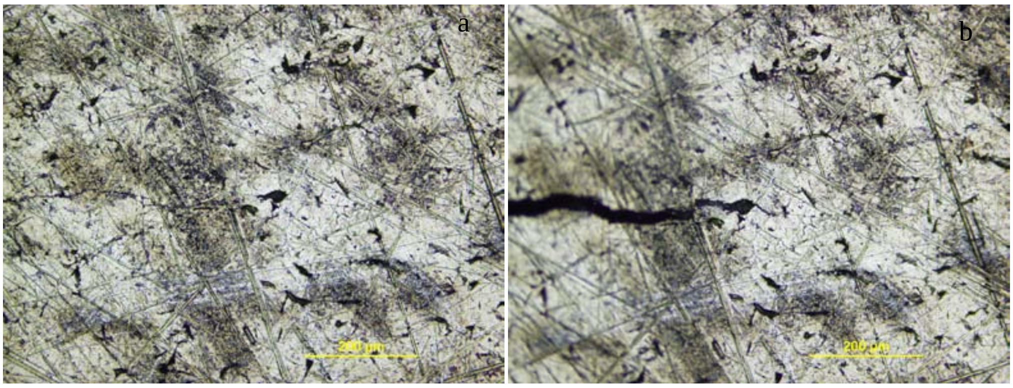

Fig. 4- 21 Sample H5 before (a) and during test (b) with wedge in it

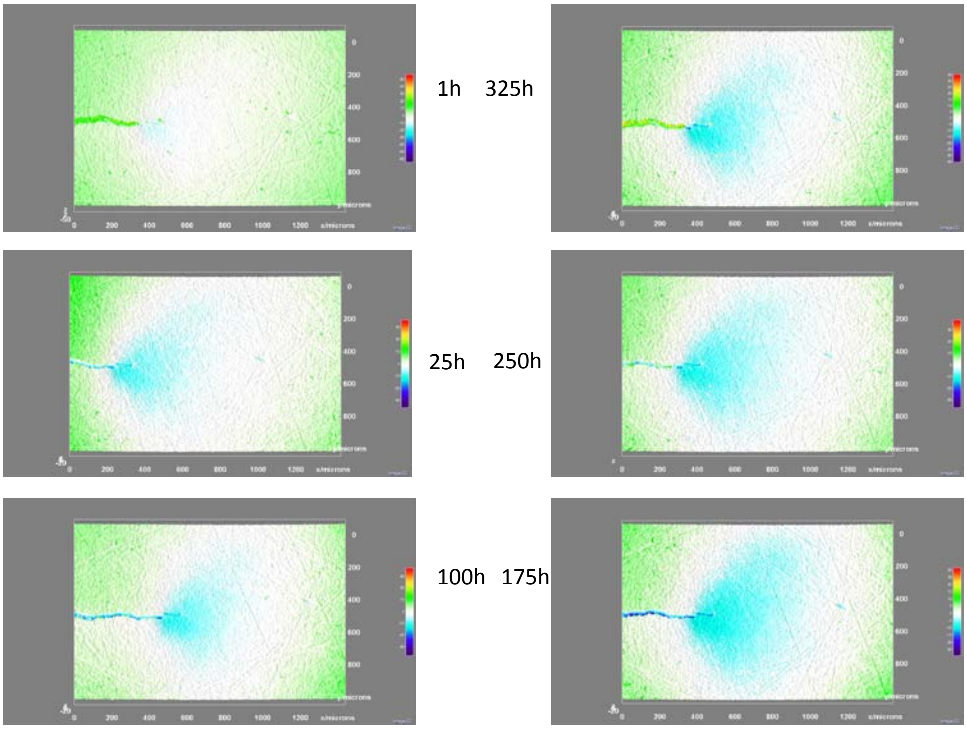

Fig. 4- 22 Plastic zone evolution of sample H5 over the time period from 1 h to 325 h

Table 4- 8 Plastic zone size of case and bulk material

K=43.5 MPa√m	Yield strength (MPa)	Plastic zone size (mm)
Case	2089	0.069
Bulk material	327.5	2.8

The images above elucidate the similar situation as sample H4, implying the bulk material dominates the behavior of the plastic zone. But the observed size of plastic zone is substantially suppressed by the presence of the case.

From plastic zone evolution aspect, the hydrogen does promote the mobility of dislocations, which is in favor of the theory of HELP. The plastic zone size observed by confocal microscope is only around 1 mm, which is only part of the total zone size. This is because what caught by microscope is the area with appreciable deformation. The plastic zone is not equally deformed within its range; especially the outer shell experiences much less deformation.

4.5 Fracture surface

In order to get a more severe cracking condition, sample H6 was further loaded (K up to 65 MPa√m) before it is pulled apart for fractography information. Extensive cracking happened during the loading on the surface enunciated in Fig. 4- 23 . It confirms no incubation needed for crack initiation on carburized and hydrogen-charged sample.

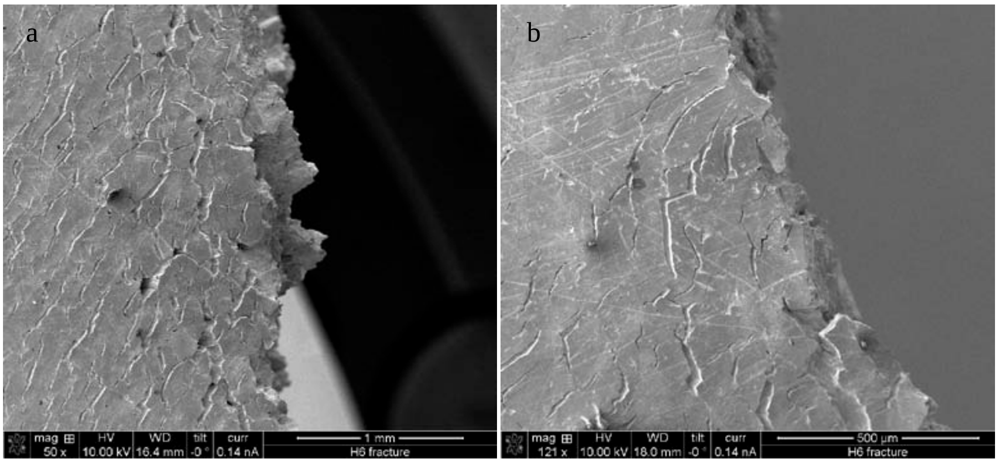

Fig. 4- 23 Two positions on sample H6 side surface experienced high stress intensity

An overview of fracture surface is shown in Fig. 4- 24 (a). The crack propagated bottom-up as indicated by the arrow. Pre-crack and tensile region can be easily distinguished. The pre-crack region is featured by the transgranular brittle surface. Large microvoids disperse all around the tensile region, suggesting the sample failed in a ductile way.

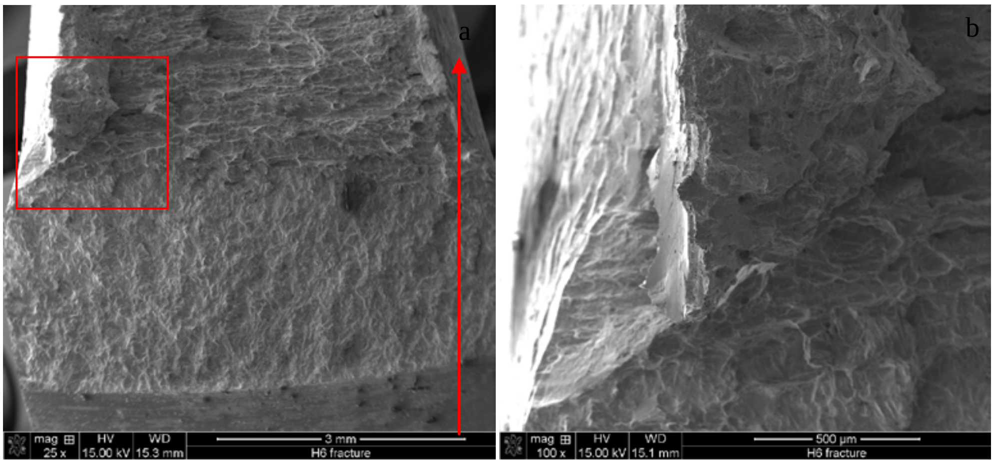

Fig. 4- 24 An overview (a) of sample H6 fracture surface, (b) is the magnified enclosed area in (a)

The interested area was enclosed in the rectangle and pictured with higher magnification in Fig. 4-

24 (b). It is even more interesting to see the difference between the case and bulk material (Fig. 4-25). Within the case, the fracture surface is rather smooth, only some crystallographic feature can be observed. Closer look at the case reveals some slip step formation. Microvoids emerge just beneath the case, signaling a transfer from brittle to ductile failure. Void is 25 um away from the case, which is the nominal case depth after standard carburization process. Some voids are even closer to the surface implying the dislocation mobility in the case. XEDS reveals that the particle in the voids are MnS, which is a common impurity in the steel. Elongated MnS strip is identified on the fracture surface and the over 10:1 aspect ratio of the strip indicates the sample maybe previously hot rolled.

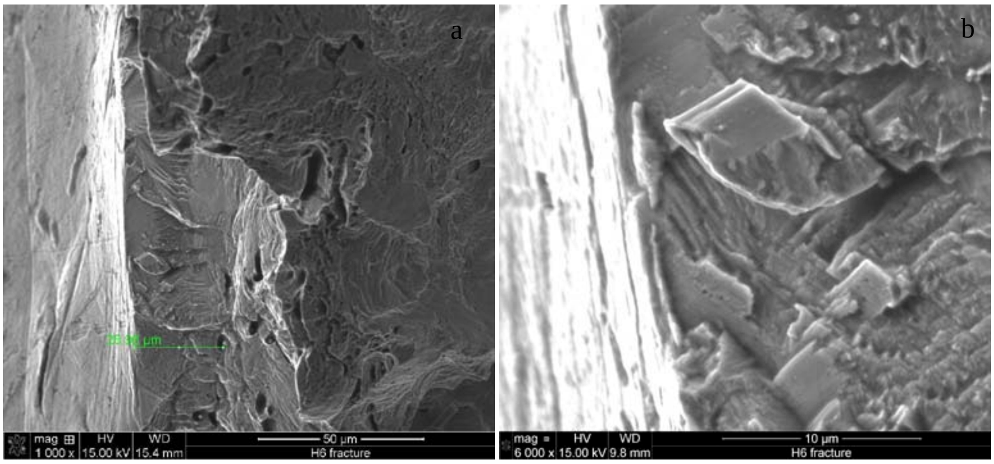

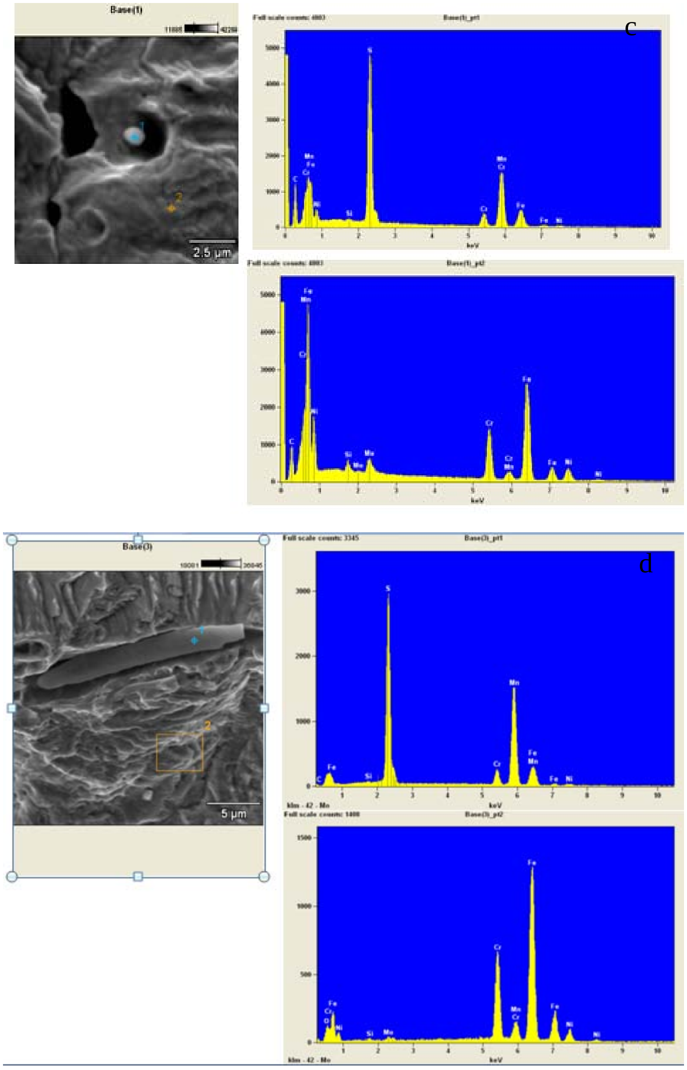

Fig. 4- 25 SEM picture of sample H6 case on fracture surface (a), (b) enlarged crystallographic feature in the case, (c) XEDS on the MnS particle in the void and (d) XEDS on the elongated MnS strip

There are some special features at the interface between the pre-crack and ductile failure regions. Some transgranular features are observed at the interface. In the Fig. 4- 26 , two relative smooth facets can be observed. There are some river-patterns on the rectangular shape facet Fig. 4- 26 (c), which originate from the lower right and grow into steps towards the upper left. This is the typical feature for river-pattern, which starts with many parallel planes and as crack advances, planes join and progressively form higher cleavage steps, like the mainstream of a river. Another cleavage facet Fig. 4- 26 (d) lies besides the first one. Similar feature is observed. Due to the polycrystal sample, the cleavage plane tilts at the grain boundary into the next grain uninterrupted. What is interesting is that the microvoids with very fine size appear just beneath these facets. This suggests the fracture feature transit from brittle cleavage failure into ductile gradually. Besides, step feature probably resulted from pre-crack lies just on the right of these two facets, indicating the two facets are at the interface between pre-crack and tensile fracture area.

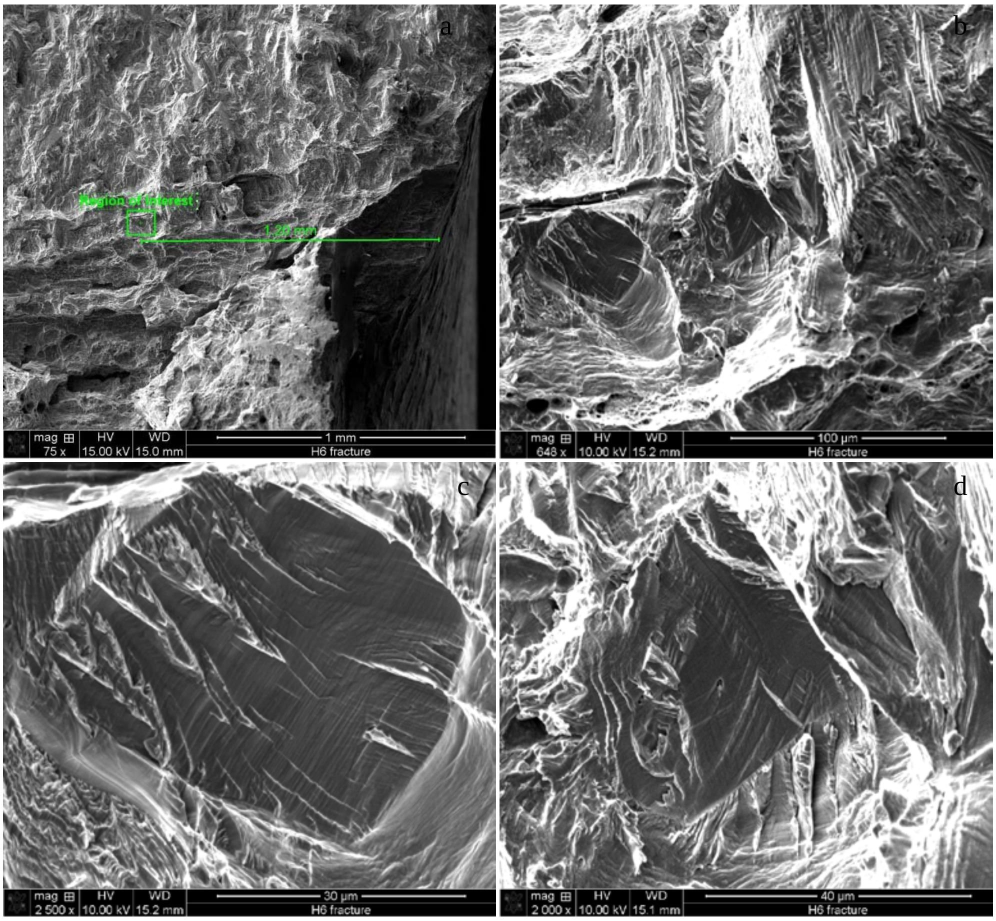

Fig. 4- 26 Transgranular facet at the interface of precrack and tensile failure region (a) location of observed features, (b) overview of the two facets, (c) magnified rectangular facet and (d) magnified triangle facet

Other cleavage features were also found in the interface region and listed in the Fig. 4- 27 below. Steps in Fig. 4- 27 (b) are very similar to the ASTM standard shown in (c). Some major steps were followed by lower steps. In Fig. 4- 28 , several big steps formed and fine size microvoids lie beneath them, which is similar to the brittle to ductile failure transition mentioned above. The brittle fracture steps were obviously within the interface area in (c). The steps were topped by stretch zone and voids are beneath them. This is a good region where definitely out of the pre-crack area but still featured by brittle failure. So the transition from brittle to ductile failure is possible.

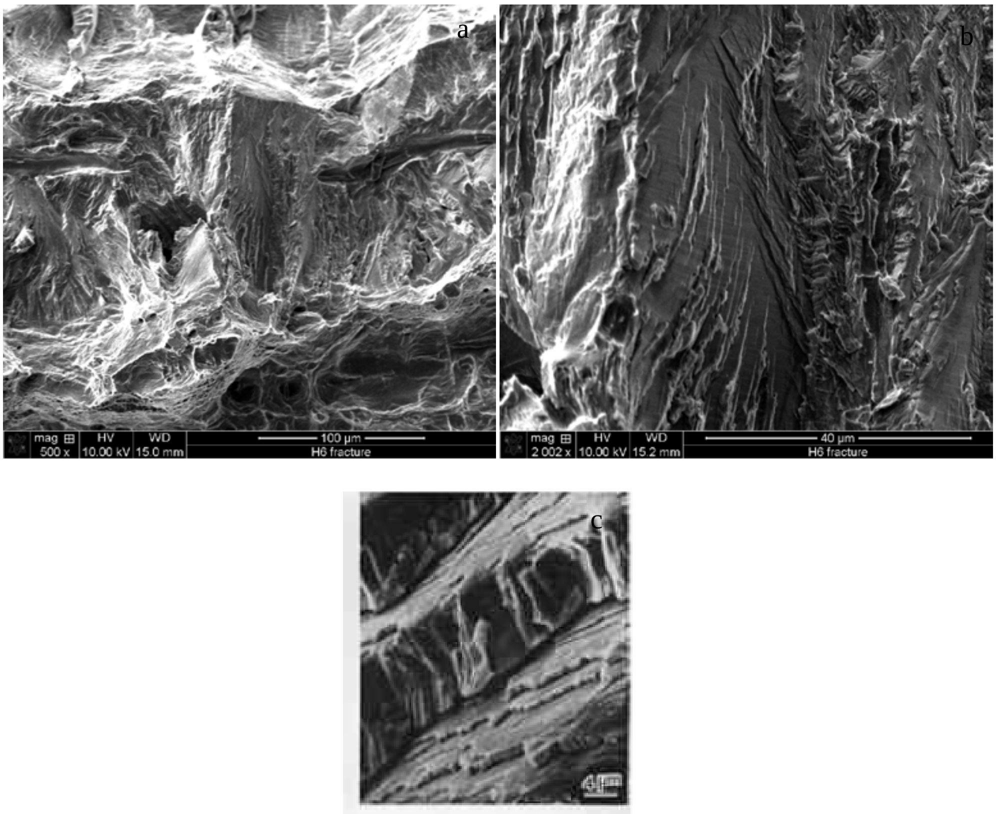

Fig. 4- 27 (a) Trangranular steps at the interface area, (b) magnified step area and (c) cleavage steps in a Cu-25 at.% Au alloy failed by transgranular stress-corrosion crack [60]

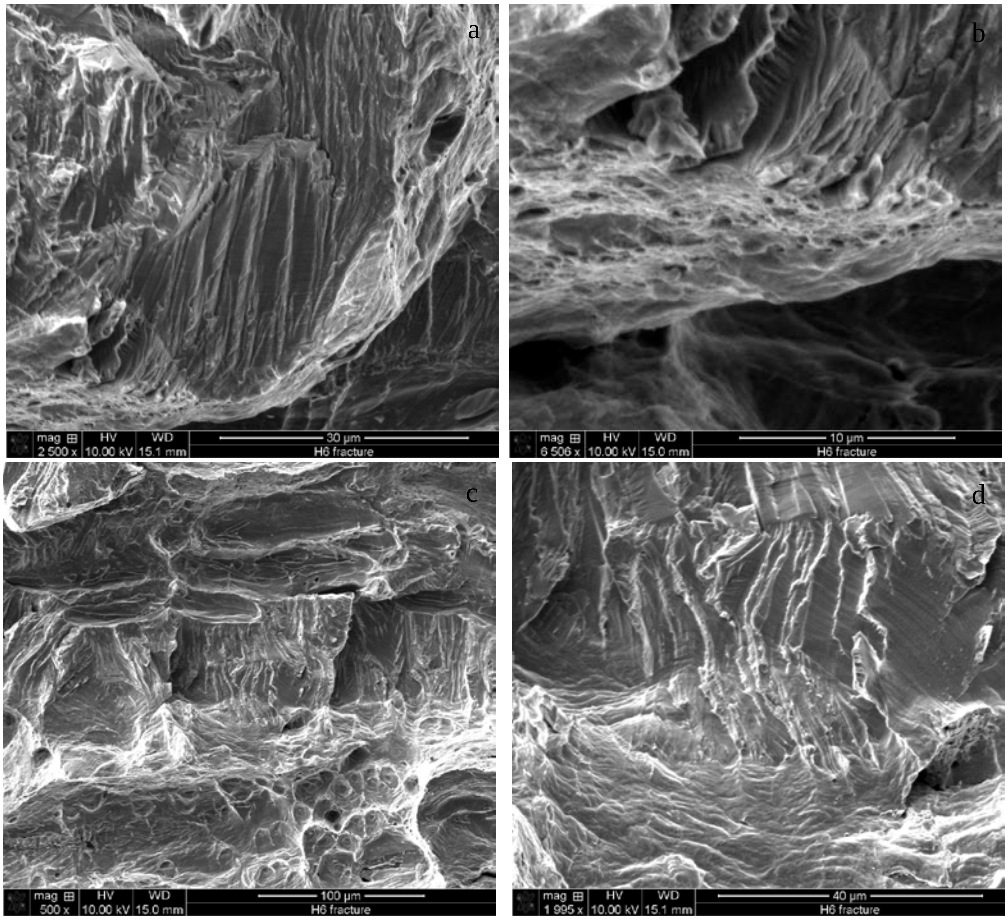

Fig. 4- 28 Brittle step feature at the interface (a), (b) closer look at the microvoids beneath it, (c) another brittle step site, (d) magnified step area

In the far field, some other features were captured and displayed in Fig. 4- 29. All the failure features are band-like, parallel to the MnS strips previously identified. One band is comprised of several rectangular cleavage facets, which is usually observed in the cathodic charging condition. Another band seems to fail intergranularly. But the size of grain is way too small for the sample, whose size is usually around 10 to 20 um. But at least, this band is heavily cracked. There are intensively secondary cracks within the band. The large grains break down to the smaller scale. However, the exact reason for this is not clear.

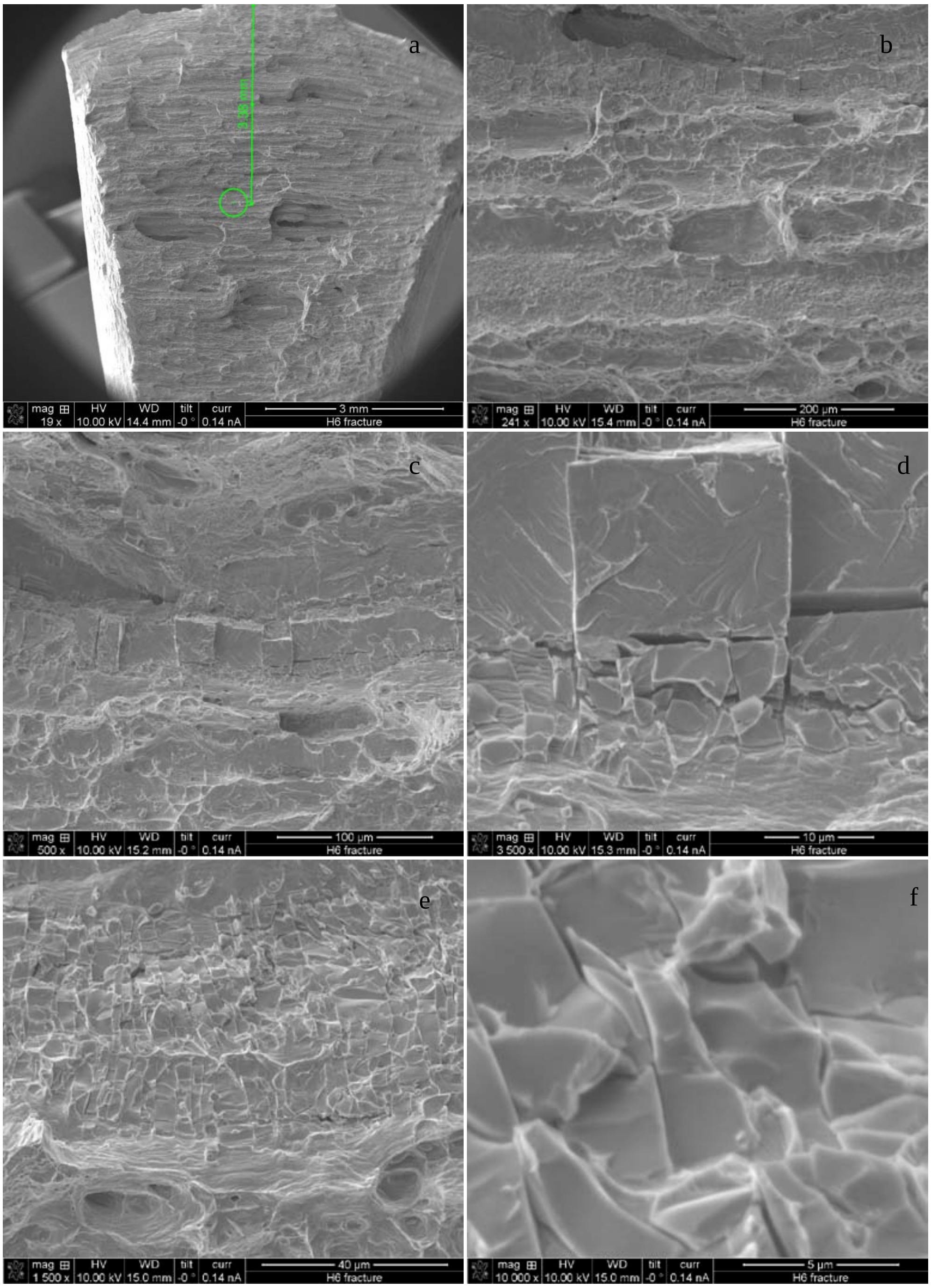

Fig. 4- 29 (a) location of observed feature, (b) Overview of two band-like features, (c) brittle facets, (d) rectangular brittle facet with high magnitude, (e) heavily cracked region and (f) magnified cracked region

5. Discussion

5.1 CTOD model

CTOD is essentially zero when the sample is unloaded because the crack should close and the two cracked surface should contact each other. However, when load is applied, the crack will open and CTOD increases correspondingly. When the load is high enough, plasticity comes in to play and some permanent plastic CTOD can be seen on the sample. From previous test result, the non-carburized 316L sample does not crack after hydrogen charging. In the core of the carburized sample, which essentially is the non-treated material, the crack only blunts by the load applied without any physical crack extension. However, crack extension is observed on the carburized surface and the crack is confined in the case. So the principle is when the sample is loaded up, at the very beginning, some plasticity takes place and crack tip blunts as illustrated in Fig. 5- 1 (a). Due to the extremely high (>2 GPa) strength in the case, the plastic zone is fairly small in the case (<100 um) so small-scale-yielding can be applied. Crack extension in the case can be treated as elastic behavior while the bulk material blunts, as illustrated in Fig. 5- 1 (b).

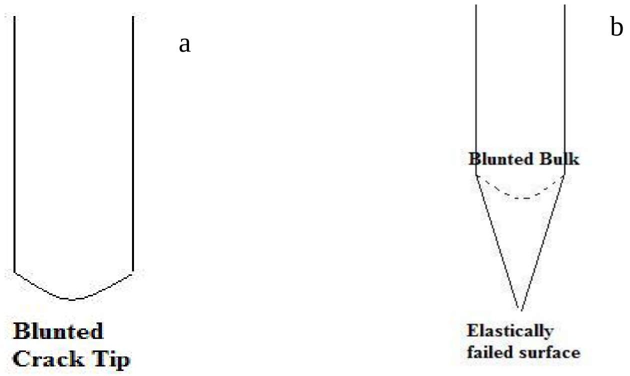

Fig. 5- 1 Schematics of loaded crack tip

Because of the strength difference between the bulk material and carburized layer, the corresponding CTOD is different. From equation 2. 6. 2, which applies for small-scale-yielding regime, the elastic CTOD can be calculated. Table 5- 1 summarizes the elastic CTOD in bulk material.

Table 5- 1 elastic CTOD on bulk material

K	$\sigma_{ys,eff} = (\sigma_{ys} + UTS)/2$	E	CTOD
40 MPa√m	327.5 MPa	193 GPa	25.6 μm

The residual stress at each depth is taken as the yield strength for carburized layer for certain depth in this study. The residual stress at certain depth is retrieved and listed in the following Table 5- 2 from the original data in Fig. 5- 2 [19]. These data was fitted by Boltzmann equation (shown in the Fig. 5- 3 (a)) and the fitting curve is presented in Fig. 5- 3 (a). The fitted residual stress at each depth is substituted into the equation 2. 6. 2. The calculated elastic CTOD values are shown in Fig. 5- 3 (b). When the residual stress drops below the effective yield stress (from 20 μm to 25 μm), the yield stress of the case was taken as the effective yield stress.

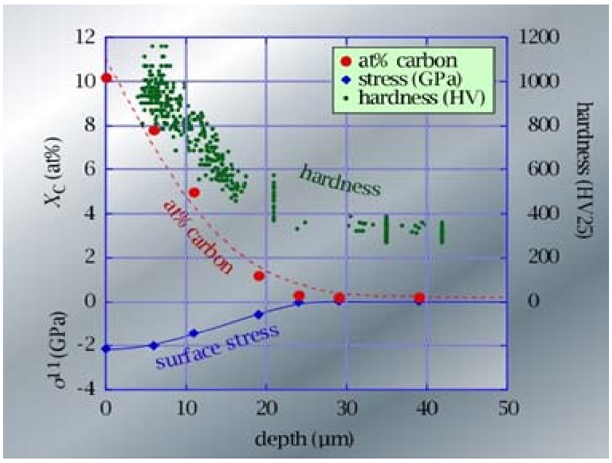

Fig. 5- 2 Residual stress on the surface

Table 5- 2 Calculated residual stress for certain depth from XRD result

Depth (μm)	Residual stress (MPa)
0	-2100
6	-2000
11	-1600
19	-200
24	0

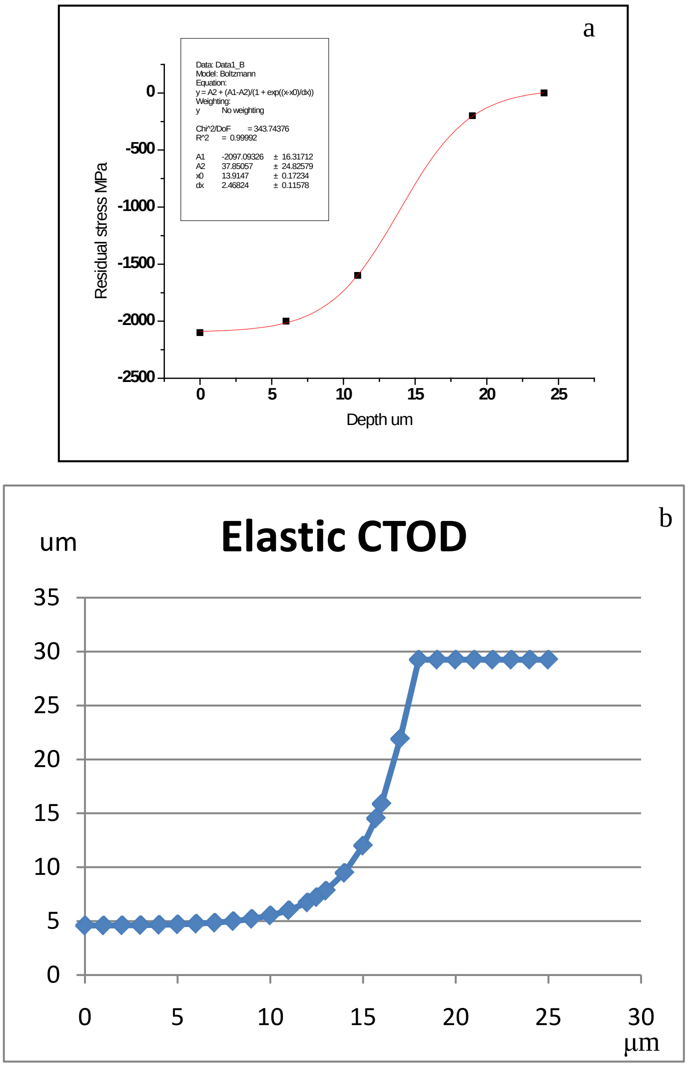

```
Data: Data1_B
Model: Boltzmann
Equation:
y = A2 + (A1-A2)/(1 + exp((x-x0)/dx))
Weighting:
y         No weighting

Chi^2/DoF       = 343.74376
R^2       =  0.99992

A1        -2097.09326     ±  16.31712
A2        37.85057        ±  24.82579
x0        13.9147         ±  0.17234
dx        2.46824         ±  0.11578
```

Fig. 5- 3 (a) Residual stress fitting result, (b) calculated elastic CTOD in the carburized layer

When the load is applied, certain stress intensity is achieved at the crack tip but the responding CTOD value varies from the very surface to the bulk material. As a result of the continuous strength change within the case, the elastic CTOD dependent on stress intensity should be continuous as well. The fundamental reason for the continuous CTOD from surface to bulk is owing to the smooth carbon concentration curve within the case.

The total CTOD at the crack tip is comprised of two parts, elastic part and plastic part. The elastic part has been taken care of above and the plastic part can be calculated by the hinge model mentioned in the previous chapter.

According to equation 2. 7. 1, the r_p, which is the rotational factor, needs to be determined beforehand. Stated in Anderson's book [10], for typical material, r_p usually equals to 0.44. But from the Saxena's paper [11], an equation is given to calculate the location of the axis of rotation in the WOL sample, which is listed below.

$$\frac{X_0}{W}=0.408778 - 1.52443\left(\frac{a}{W}\right) + 9.04028\left(\frac{a}{W}\right)^2 - 17.3354\left(\frac{a}{W}\right)^3 + 15.9708\left(\frac{a}{W}\right)^4 - 5.56415\left(\frac{a}{W}\right)^5 \tag{5.1}$$

Table 5- 3 summarizes the sample configuration considered and calculation result. The calculated r_p is less than one third of 0.44. This leads to a big difference on the calculated plastic CTOD.

Table 5- 3 Sample H6 configuration and rotational factor calculation

Crack length	Width	a/W	X_0/W	r_p
36.015 mm	76.25 mm	0.4723	0.5430	0.134

The recorded Load vs COD curve of H6 is in Fig. 4- 5 (b). One initial data point used to get V_p is (101.0 lb, 0.00001"). On the unloading portion, a linear fitting of the data points around 101 lb is carried out and the fitting equation is listed below:

$$P=101103* V_p -141.71 \tag{5.2}$$

On the basis of the fitting equation 5.2, COD at the load of 101 lb is 0.00240”. The plastic COD obtained from these data is 0.00239”.

By knowing the crack mouth opening displacement (V_p), the only thing undetermined in equation 2. 7. 2 is the value of rotational factor (r_p). However, if the plastic portion of CTOD at the original crack tip can be known, the actual rotational factor can be calculated accordingly. The fact that the core material beneath the case does not crack when the load is present makes measuring the CTOD after the test possible. Because the plastic deformation at the crack tip is permanent, when the sample is free of load, the remnant opening displacement at the original crack tip is the plastic CTOD initially in the bulk material. This is based on the assumption that the carburized layer failed elastically during the test, and there is no cracking in the bulk material. Substituting the plastic COD value 0.00239” into equation 2. 7. 2, along with z=2.5 mm, the result for different r_p value is listed in the following table.

Table 5- 4 the calculated plastic CTOD based on different rotational factor

r_p	CTOD (δ) (μm)	V_p =0.00239”
0.134	7.5	a=2.215 mm
0.44	19.1	W=76.25 mm

It’s obvious that the CTOD value for r_p =0.44 is more than twice of that for r_p =0.134. Therefore, it can be easily told which one is practically close to reality. By comparing the Fig. 4- 6 (a) and (b)

(H6 before and after test), the position of the original crack tip can be identified. A blue line is drawn on the Fig. 5- 4 to signify the crack tip. Two other lines along the crack are drawn. The positions of the three lines are: near the new crack tip (purple), original crack tip (blue) and the wake of crack (orange). Grey scale line scan, processed by ImageJ, is taken on all three lines. Fig. 5- 4 (b-d) display the crack width of the 3 lines from tip to the crack wake, respectively.

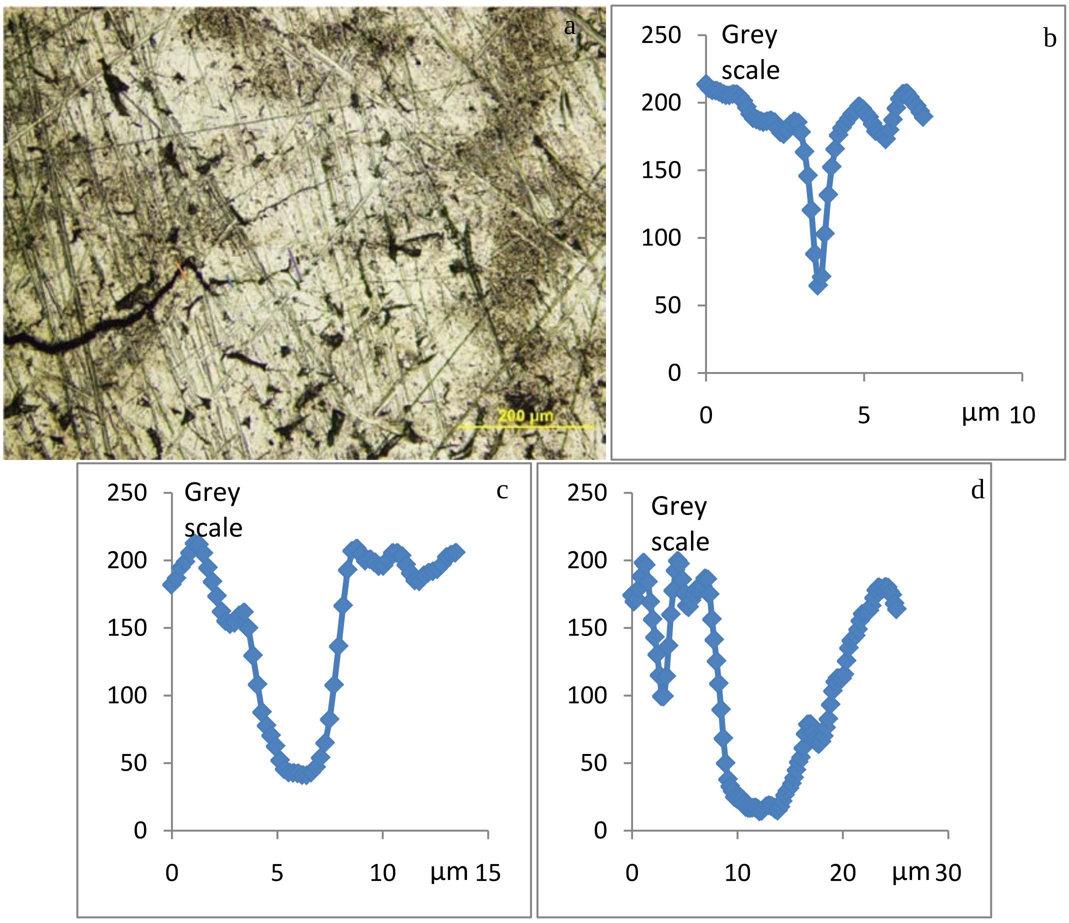

Fig. 5- 4 (a) Crack extension on sample H6, grey scale of at new crack tip (b), original crack tip (c) and in the wake of crack (d)

The width of the crack is defined by the grey scale. The grey scale is low in the crack owing to no light reflected back and it is high on the uncracked surface. Fig. 5- 4 (b) is the purple line and it indicates the width of the crack is around 1.5 μm. The position of the purple line is very close to the new crack tip but not exactly on it. The crack width defined by the curve in Fig. 5- 4 (b) is 7.5 μm. This value is the same to the predicted one based on the value of r_p =0.134. In (c), whose line scan is taken behind the original crack tip, the width of the crack is around 16.5 μm. Even in the wake of the crack, the width of the crack is still smaller than the value predicted by r_p =0.44. So the location of rotation axis is accurately predicted by the linear elastic equation 5.1 and r_p =0.134. However, one thing should be noted that equation 5.1 is based on the LEFM. In this case, it is obvious that there is plasticity at the crack tip and so the r_p value should be slight larger than 0.134. The plastic CTOD should be larger than the previous calculation.

Based on the CTOD observed on the very sample surface, it is reasonable to assume that the carburized layer cannot counterbalance any plastic CTOD. In other words, the plastic CTOD is uniform through the whole thickness of the case. This can be justified by the FIB cross-sections on the H6 surface. Except the one at the original crack tip, all the other cross-sections reveal similar crack width through the crack depth. The total CTOD is the sum of the elastic and plastic parts as shown in Fig. 5- 5.

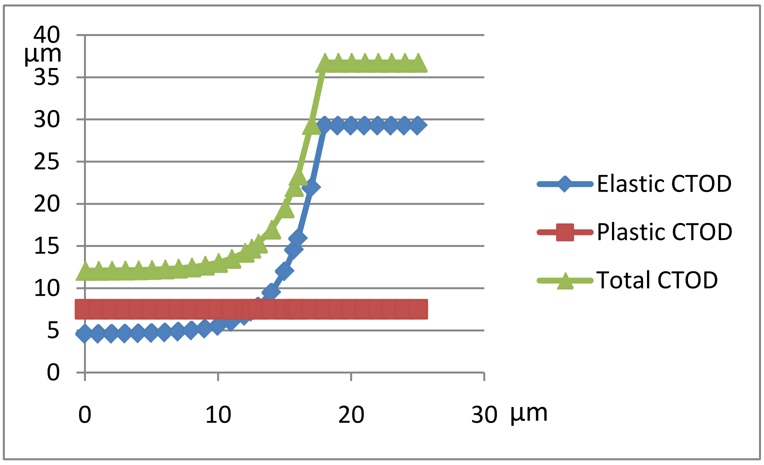

Fig. 5- 5 CTOD variation through the case thickness

At this point, the total CTOD on the sample is obtained at the load of 1650 lb. The CTOD varies from the surface to the core due to the different strength within the case. When the small-scale yielding condition applies, equation 2. 6. 2 can be reversed and simplified into equation 5.3,

$$K=\text{sqrt}\ (\sigma_{ys}*E*\delta) \tag{5.3}$$

The actual stress intensity within the case can be predicted by this equation when the nominal stress intensity is applied by the external load. By substituting yield strengths at different case depths, the Young’s modulus and the calculated CTOD, the actual stress intensity can be estimated and the result is plotted in the Fig. 5- 6. The curve in Fig. 5- 6 signifies the actual stress intensity in the case increases as the surface is approached. The maximum stress intensity is at the very surface and it is about 78.8 MPa√m.

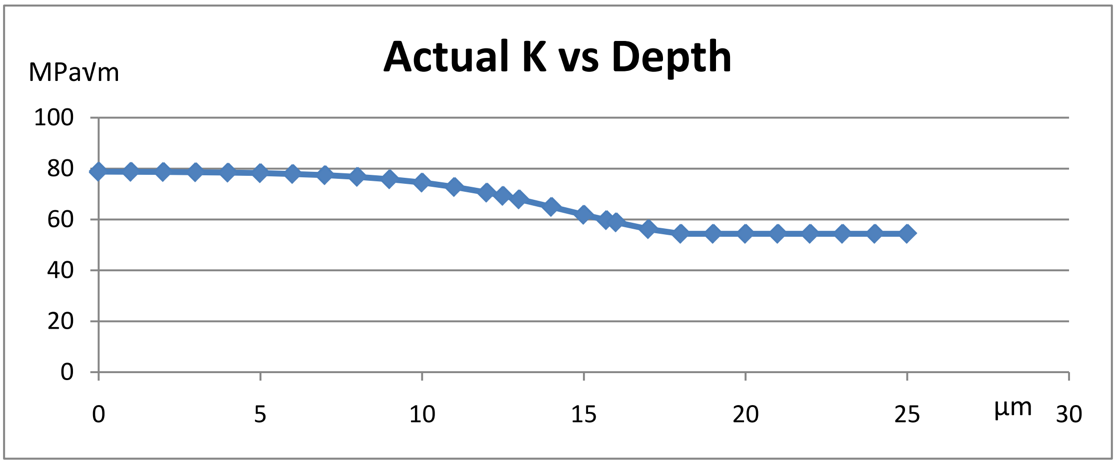

Fig. 5- 6 The actual stress intensity vs depth on sample H6

All previous analysis is based on one surface of the H6 sample. Now similar analysis is carried out on the other side. The tested surface is in Fig. 5- 7 (a) and the blue line indicates the position of the original crack tip. The grey scale scan is in the Fig. 5- 7 (b). The crack width is about 4 um, which is only half of that on the other side. This is due to the difference in the crack length and further detailed explanation will be presented in the next section. So the actual stress intensity in this layer can also be forecasted by the CTOD model and resulting stress intensity curve is plotted in Fig. 5- 8. Even though the K_{max} on the very surface is lower than that on the other side, the overall trend is the same.

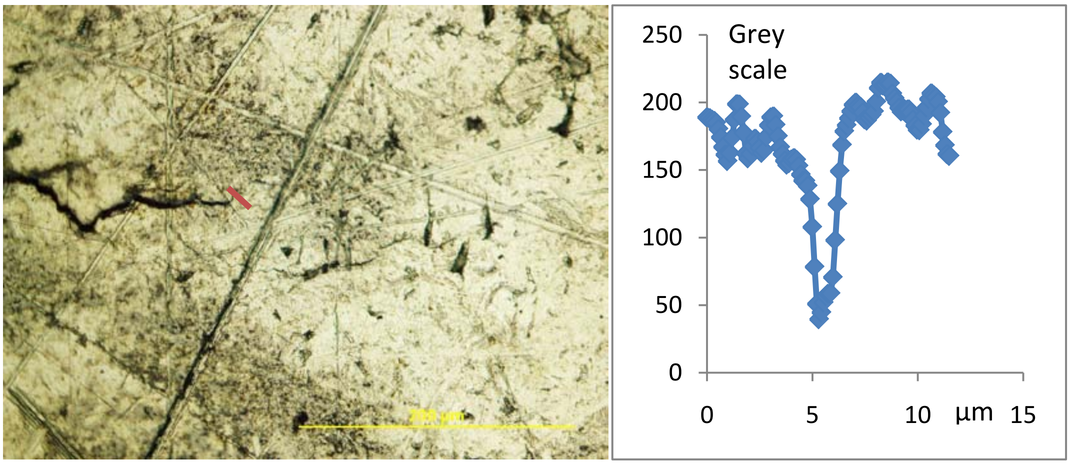

Fig. 5- 7 (a) Back surface of sample H6 and (b) grey scale of the red line

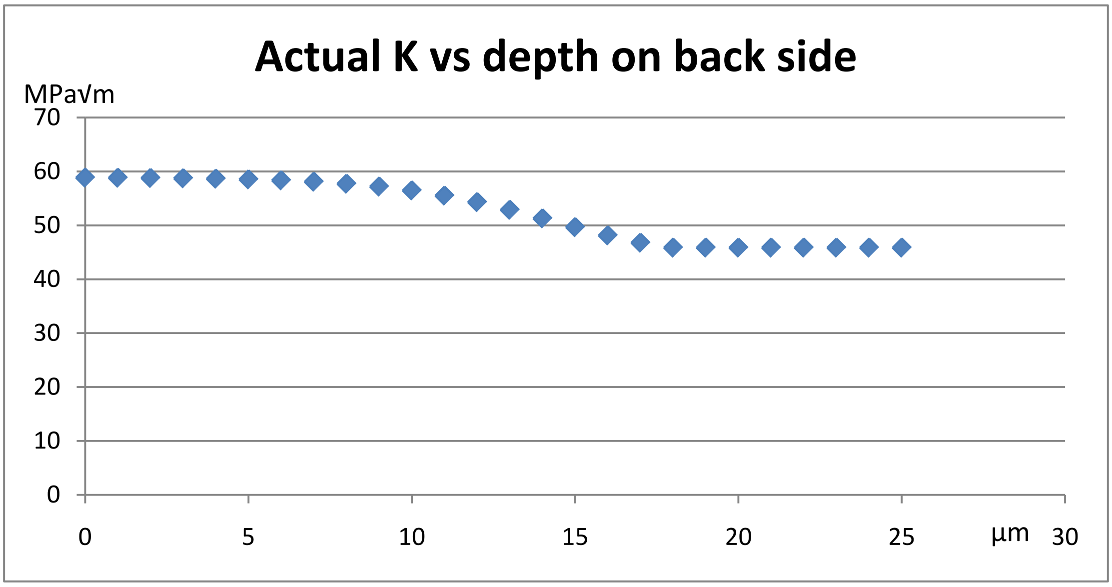

Fig. 5- 8 Actual K vs depth on the back of sample H6

To sum up, the actual stress intensity in the case is larger than the nominally applied stress intensity owing to the high strength within the case. Since stress intensity is the driving force of the crack propagation, the difference in the actual stress intensity will give rise to the different crack propagation distance from the original crack tip. This can be readily seen on the very surface of the two sides of the sample. The newly extended crack length is much longer on the fore side than that on the back side.

5.2 Stress intensity interpretation

The predicted stress intensity by CTOD model is the driving force for the crack extension. When the crack is arrested ultimately, the stress intensity at the crack tip is equal to the threshold. The difference between the driving force stress intensity and the threshold stress intensity determines how far the crack can go.

Because the strength of the case increases as the surface is approached, the threshold may decrease correspondingly as what happens in the high strength steel case. So the largest difference between applied stress intensity and threshold is on the very surface, where the stress intensity applied is largest while the threshold is lowest as can be seen in the Fig. 5- 9. The three data points are fitted exponentially to get the threshold line. The higher two points are experimental data [56]. The datum point on the surface is the calculation result that will be introduced later. The crack on the very surface has the potential to propagate farthest according to the figure. Another thing should be noticed is that the two curve in the Fig. 5- 9 actually cross over each other. This infers that somewhere in the case depth, the applied stress intensity will be equal to or lower than the threshold. It leads to the prediction of the crack is only partly through the thickness of the case, i.e. the crack never propagates at certain depth. However, the FIB cross-sections seem to rebut this. FIB cross-section at sample H6 original crack (Fig. 4- 10 (b)) demonstrates crack go through the whole case thickness. But this may be due to the possible partial carburization at the pre-crack tip.

Other FIB cross-sections support this partial penetration depth prediction.

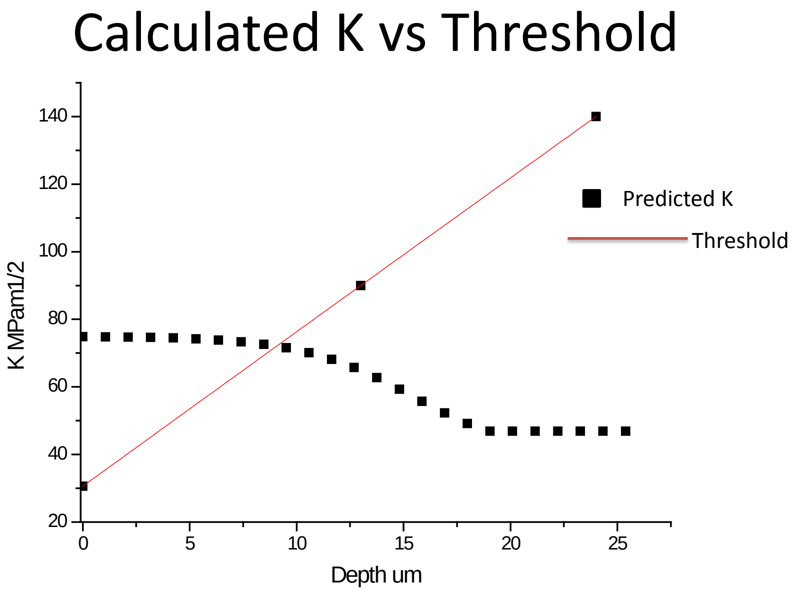

Fig. 5- 9 Calculated K vs Threshold through the case thickness

The difference between the applied stress intensity and threshold will be compensated by the stress intensity contributed by the residual stress in the wake of the new crack and also by the stress intensity introduced by the ligament of the ductile core material. The stress intensity contributed by residual stress can be calculated by the weight function. The stress intensity due to the ductile core material can be predicted by the bridging model [61].

5.2.1 Stress intensity from residual stress

The residual stress in the wake of newly cracking surface will impose stress intensity factor that can offset the applied stress intensity. This stress intensity can be calculated by weight function, equation 5.4.

$$K=\int_0^a \sigma(x)\ m(\alpha,\ x)\ dx \qquad (5.4)$$

In order to use weight function, the crack length, newly extended crack length and width of the sample need to be known. All these can be measure from the sample after the test (Fig. 4- 6). For the fore side of H6 sample, the configuration is summarized in Table 5- 5. It is reasonable to assume that at the same depth the residual stress is the same. The stress term in equation 5.4 can be moved out from the integral and equation 5.5 is obtained.

$$K_{res} = \sigma_{res} * \int_0^a m(\alpha,x)dx \qquad (5.5)$$

The fitting curve for residual stress within the case has been displayed in Fig. 5- 3 (a) previously. After integrating weight function according to equation (2. 13), by substituting the residual stress, the stress intensity due to the residual stress at this depth is readily available.

Table 5- 5 Sample configuration used in weight function calculation and result

Initial crack length a_i	Final crack length a_f	Crack extension	Width W	h
35.57 mm	35.74 mm	0.17 mm	76.25 mm	0.02096√m

Further calculation about stress intensity due to residual stress on the very surface is -37.9 MPa√m. According to the calculation result, when the crack extends 0.17 mm ahead of the original crack tip, the residual stress in the wake of newly cracked surface impose a stress intensity on the crack. Consequently, the driving force is relaxed by this amount of stress intensity. When the driving force stress intensity is reduced to the value of threshold, the crack will stop finally.

5.2.2 Bridging model

Various kinds of reinforcement shapes have been employed in the composite, like particulates and fibers. Laminate system is also a common style and often shows the best fracture resistance. It is a very efficient way to increase the toughness of the intrinsic brittle intermetallic compound, illustrated schematically in Fig. 5- 10. The advantage of laminate system is the high aspect ratio of the second phase increases the probability of intersection with the crack, therefore enhancing the toughness by creating a larger shielding zone of continuous bridges in the crack wake. According to the sketch, there are two orientations: one is crack arrester orientation and the other is crack divider orientation. The arrester orientation is defined as the crack grows perpendicular to the layer interface yet subsequently through each layer; the divider orientation is the crack plane normal to the layers and crack advances simultaneously through all layers [61, 62, 63].

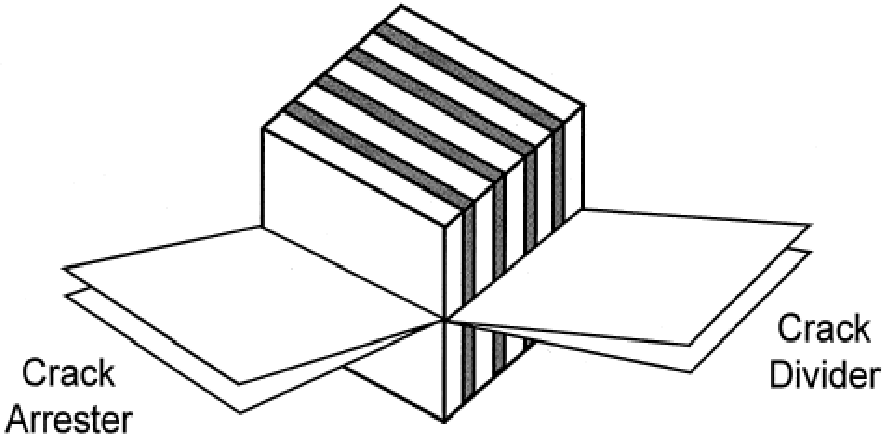

Fig. 5- 10 Laminate composite orientation

After carburization, WOL samples can be treated as a three-layer laminate system, which has two brittle layers embracing the ductile matrix. The orientation of the sample is crack divider, i.e. the crack goes through all three layers at the same time. In the crack divider orientated laminate system, it is well established that the brittle phase will tunnel ahead of the crack tip, leaving the ductile phase behind [61]. The ductile phase behind can form a bridging zone to shield the far-field applied stress intensity. The significant increase in the toughness of the laminate system is mainly attributed to the bridging zone (crack tunneling). This bridging zone will actually reduce effective stress intensity at the crack tip.

The effect of bridging zone can be characterized by the bridging model. The schematic of bridging model is in Fig. 5- 11. The shielding contribution from bridging zone can be calculated according to equation 5.6.

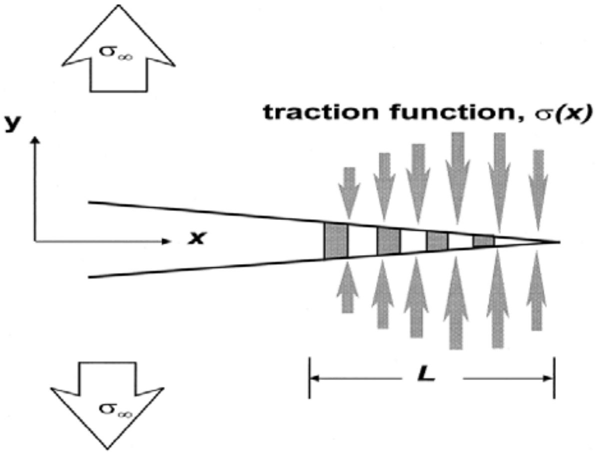

Fig. 5- 11 Schematic representation of the bridging model

$$K_b = \int_L \sigma(x)h(\alpha, x)dx \tag{5.6}$$

where K_b is the stress intensity contribution from bridging zone, σ(x) is the crack surface traction due to the ligament in the bridging zone, h(α,x) is the weight function across the bridging area, L is the length of bridging zone. According to the superposition principles, the actual stress intensity at the crack tip can be calculated by equation 5.7 when bridging stress intensity is counted in.

$$K_{act}=K_{app}-K_b+K_{res} \tag{5.7}$$

The computation of bridging stress intensity (equation (5.6)) requires the knowledge of crack surface traction σ(x) and it is not very straightforward work. A simplified approach to this problem can be used alternatively with good accuracy [61]. It is assumed that σ(x) is a constant function and uniformly active over the bridging zone. The magnitude of this traction can be equal to some characteristic flow parameter, σ_c, which effectively is the constraint flow stress of the bridging metal. It can be taken as the yield strength of the metal. The discreteness of the metal is counted in by multiplying the volume fraction, f, of the bridging metal. With these foregoing assumptions, the equation 5.7 can be rewritten as equation 5.8,

$$K_{act}=K_{app}-f\sigma_c \int_L h(\alpha, x)dx+K_{res} \tag{5.8}$$

From the continuous pictures taken from confocal microscope, the crack lengths measured on two sides of the sample are different. One side (fore side) is 1.77 mm and the other side (back side) is 2.66 mm. The difference in the initial crack length will lead to the difference of actual stress intensity applied on the two sides due to the bridging effect. The material between the two surface crack tips shields some stress intensity. Here by assuming the crack tip connects the two surface crack tips linearly, the fraction of bridging area is 0.5 and is the shadowed area in the Fig. 5- 12. According to equation 5.8, the bridging stress intensity can be calculated as listed in Table 5- 6. The applied stress intensity is lower at the back side whose crack length is longer. This is the reason that the plastic CTOD at the back side is smaller and thus the actual stress intensity on the very surface is lower.

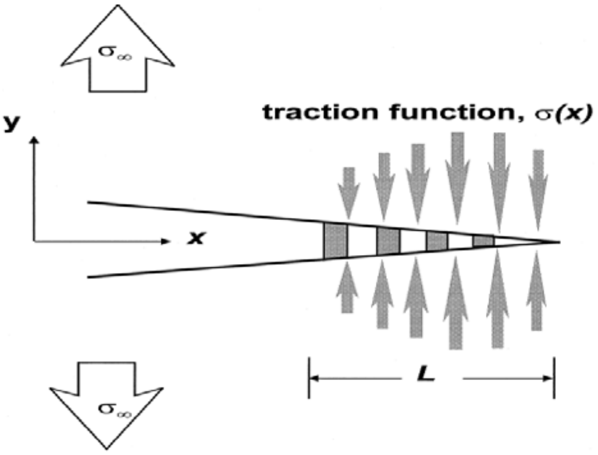

Fig. 5- 12 Sketch of bridging model

Table 5- 6 Bridging K contributed from ductile ligament in the wake of crack

Yield stress (MPa)	K_b (MPa√m)	h=0.04938 (√m)
170	4.2	f=0.5
327.5	8.1	

The bridging model is not only in effect when there is difference in the initial crack length, but also when the crack propagates. When the crack advances, the core material beneath the newly cracked surface will further shield some driving force stress intensity away. The fraction of bridging area can be calculated according to the geometric relationship as sketched in the Fig. 5-13. The new counterbalancing bridging stress intensity is summarized in Table 5- 7. The contribution of bridging stress intensity from new crack extension is pretty small.

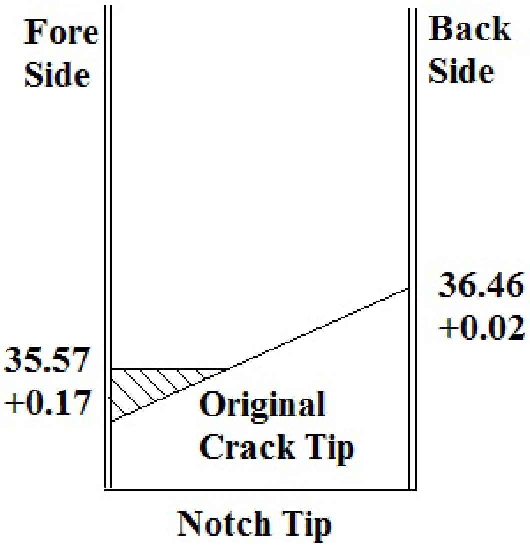

Fig. 5- 13 Sketch for bridging K contributed from new crack extension (unit: mm)

Table 5- 7 Calculation on sample H6 of bridging K contributed from new crack extension

	a (mm)	Δa (mm)	f	h (√m)	K_b* (MPa√m)
Fore	35.57	0.17	0.10	0.02096	0.3
Back	36.46	0.02	1.0	0.00714	1.2

* K_b is calculated based on 0.2% yield strength, i.e. 170 MPa

*The shadowed area is the bridging area due to newly crack extension on the fore side. On the back side the whole area ahead of the original crack tip is the bridging area (f=1).

To sum up, the overall bridging stress intensity is comprised of two parts: one is the bridging due to the crack length difference and the other is owing to the new crack extension.

5.2.3 Threshold calculation

In the light of the CTOD model developed in the previous section, the overall driving force for crack extension is actually higher than the nominally applied stress intensity. This total driving force is counterbalanced by the stress intensity from bridging effect and residual stress in the wake of newly cracked surface, as expressed in equation 5.7. Accordingly, when the driving force stress intensity is down to critical threshold value, the crack stops propagating. Table 5- 8 below summarizes the overall data, including the calculated threshold. There is little difference between the resulting threshold values on two sides, but overall they agree well.

Table 5- 8 Calculation of sample H6 cracking threshold

Unit: MPa√m	K_{act}	K_{res}	K_b	K_{th}
Fore	78.8	-37.9	0.3	40.6
Back	58.8	-14.9	5.6	38.3

5.2.4 Threshold variation across the depth

The threshold of partial penetrated crack in the case unveiled by FIB can be calculated by the method stated above as well. The sketch of this certain depth threshold is illustrated in Fig. 5- 14 below. Combined with the length and depth information from FIB, the thresholds are calculated and listed in the Table 5- 9.

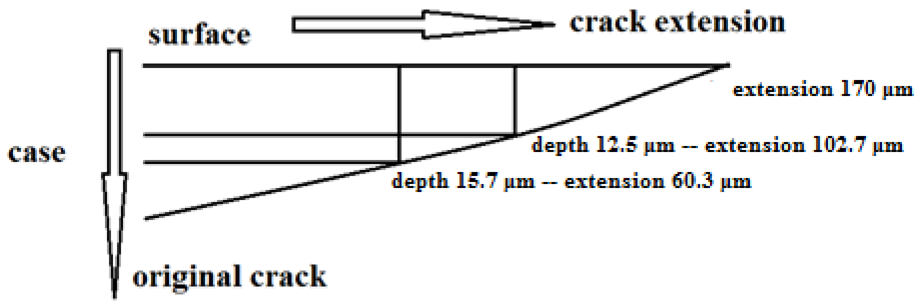

Fig. 5- 14 Schematic of crack depth variatioin based on FIB cross-sections

Table 5- 9 Thresholds of different depths

Depth (µm)	Distance (µm)	K_{act} (MPa√m)	K_{res} (MPa√m)	K_{th} (MPa√m)
0	170	74.8	-37.9	36.6
12.5	102.7	64.5	-21.6	42.6
15.7	60.3	53.6	-8.2	45.1

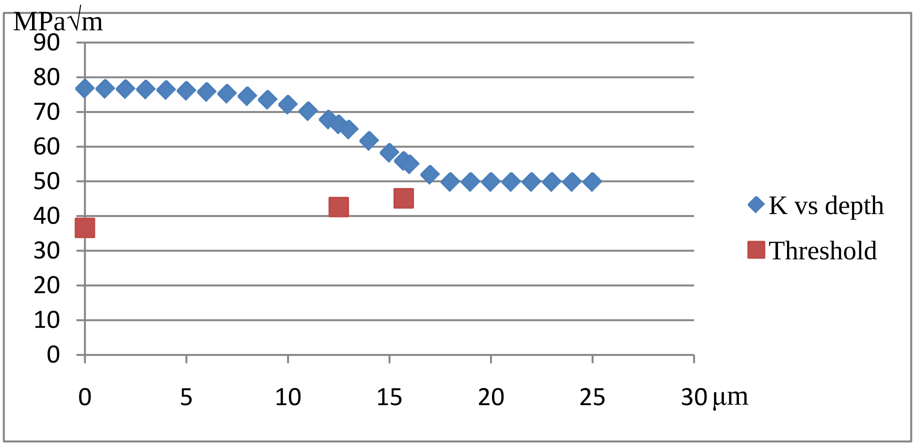

Fig. 5- 15 Driving force stress intensity vs depth and threshold variation with depth

The threshold versus case depth is plotted in Fig. 5- 15, combined with driving force stress intensity versus case depth. The threshold increases as the bulk material is approached. The inverse relationship between the yield strength and cracking threshold maintains. In Fig. 5- 9, which is the estimated threshold vs case depth before any experimental result, the threshold value is well above driving force stress intensity at 12.5 μm. Thresholds used in that plot are converted from papers about 316 stainless steel with certain yielding strength obtained by work-hardening. However, the shape of the Fig. 5- 15 is totally different, in which the cracking even occurs at the depth of 16 μm. Moreover, the FIB cross-section at the original crack tip reveals the nearly through thickness cracking. This may be an exception due to the partial carburization at the pre-crack tip. Nevertheless, the different curve shape can be attributed to the different mechanisms to strengthen the steel. The work-hardened steel seems to be better than the same high level strength achieved by carburization process with respect to the hydrogen-induced cracking, implying the carbon injected into the steel is more sensitive to the hydrogen.

5.3 Fracture surface analysis

XRD was used to identify the phase present on the fracture surface. A scan pattern on H6 fracture surface with 5s/step is shown Fig. 5- 16. Compared with reference peaks in Table 5- 10, the phases present on the H6 fracture are γ, α' and ε, summarized in Table 5- 11. Except identified phases, one peak at 48.1° does not belong to any regular phase on hydrogen-charged sample. From PDF card, Fe P63/mmc, hexagonal iron is a possible candidate because its highest intensity peak locates there. However, this phase is very uncommon in the stainless steel and other two major peaks of this phase are not applicable in the XRD pattern. So further investigation is necessary in order to identify this peak. On the other hand, the peak positions of delta ferrite are nearly the same to those of martensite, so a XRD pattern alone is not enough to be a piece of evidence for the existence of either delta-ferrite or martensite.

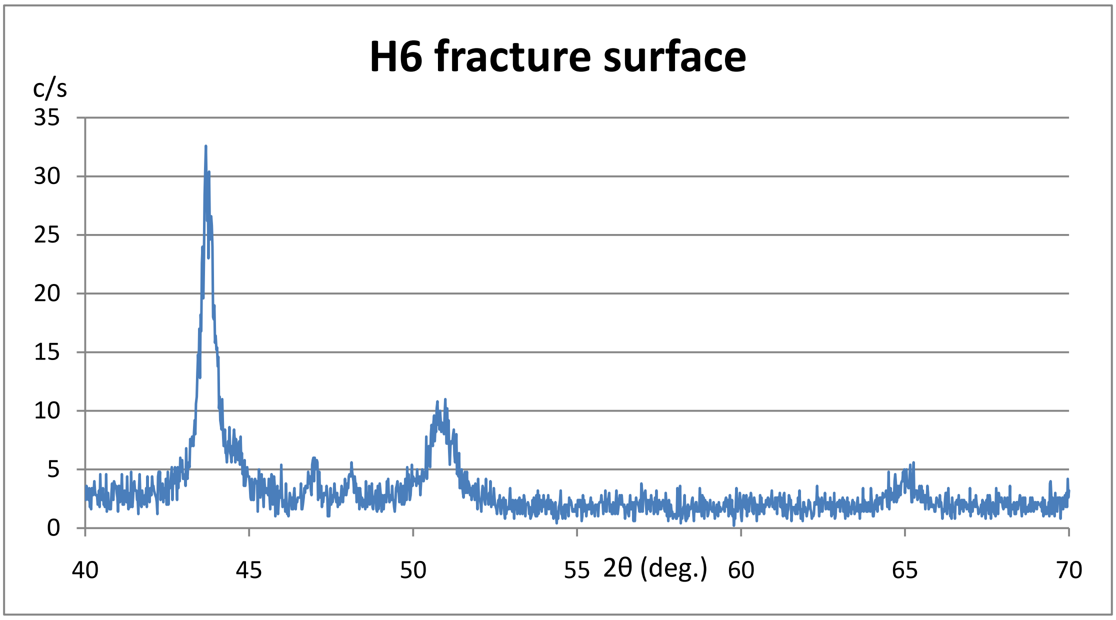

Fig. 5- 16 XRD pattern on H6 fracture surface

Table 5- 10 XRD peaks of common phase on hydrogen charged surface

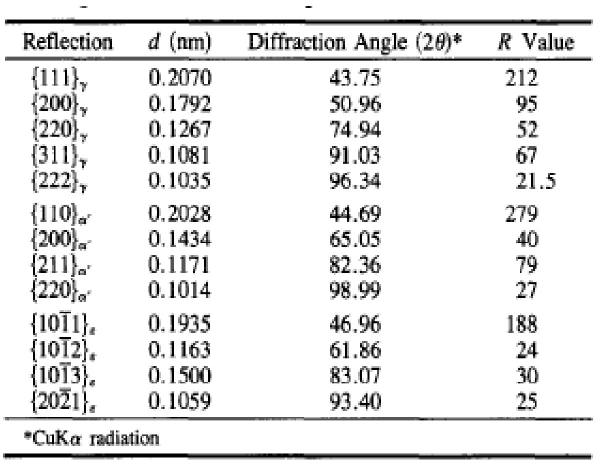

Reflection	*d* (nm)	Diffraction Angle (2*θ*)*	*R* Value
$\{111\}_\gamma$	0.2070	43.75	212
$\{200\}_\gamma$	0.1792	50.96	95
$\{220\}_\gamma$	0.1267	74.94	52
$\{311\}_\gamma$	0.1081	91.03	67
$\{222\}_\gamma$	0.1035	96.34	21.5
$\{110\}_{\alpha'}$	0.2028	44.69	279
$\{200\}_{\alpha'}$	0.1434	65.05	40
$\{211\}_{\alpha'}$	0.1171	82.36	79
$\{220\}_{\alpha'}$	0.1014	98.99	27
$\{10\bar{1}1\}_\epsilon$	0.1935	46.96	188
$\{10\bar{1}2\}_\epsilon$	0.1163	61.86	24
$\{10\bar{1}3\}_\epsilon$	0.1500	83.07	30
$\{20\bar{2}1\}_\epsilon$	0.1059	93.40	25

*CuKα radiation

Table 5- 11 Identified phase on the H6 fracture surface

2θ (deg.)	Phase
43.7	γ
44.6	α’
47	ε
48.1	unknown
50.8	γ
65	α’

One more XRD scan on non-treated sample fracture surface is available. Besides two peaks from γ phase, only a peak at 44° which either belongs to deformation-induced martensite or ferrite. Another two scans on the H6 and H2 plane surface demonstrate only γ phase available in the sample represented in Fig. 5- 17. Therefore, the extra peaks on the H6 fracture surface can only be attributed to the fracture process and the presence of hydrogen.

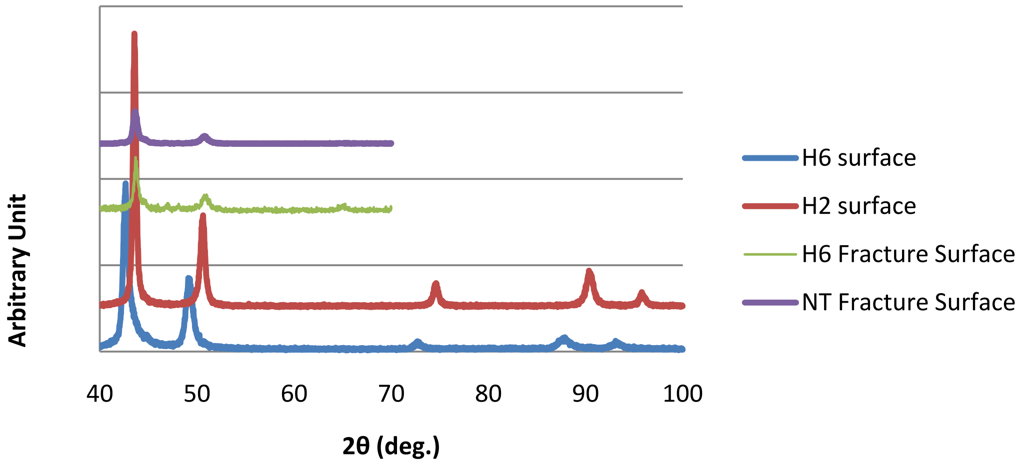

Fig. 5- 17 XRD scans on H2 and H6 surfaces and NT andH6 fracture surfaces

Elemental mapping was done on the brittle failure area as illustrated in Fig. 5- 18. It reveals that the brittle featured area is enriched by chromium and depleted by nickel. This segregation should be present prior to the tensile failure, because the suspected martensite transformation is diffusionless. Therefore, this segregation is the best evidence of existence of delta ferrite. The delta ferrite is inherently susceptible to hydrogen and failed in brittle way due to its BCC nature.

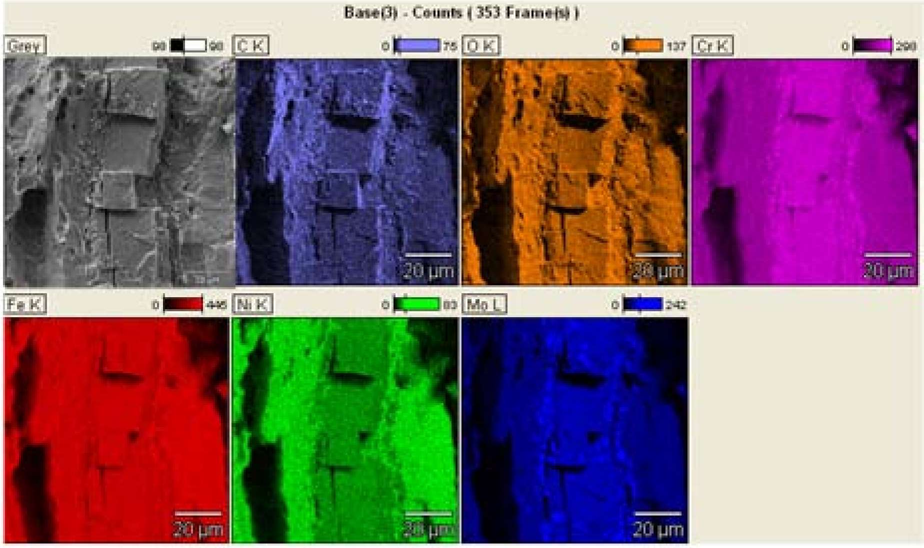

Fig. 5- 18 XEDS mapping on brittle featured fracture surface

The heavily cracked area next to the rectangular facet is enriched by molybdenum as the sparkling bright spot in the Fig. 5- 18 in the Mo mapping. In order to confirm this, another mapping was finished shown in Fig. 5- 19. Though the mapping time is not long enough to get a decent nickel distribution, the distributions of Mo and Cr are clear. These heavily cracked regions are enriched by Cr and Mo. This implies the Mo is more susceptible to hydrogen than other elements. Mo polycrystal itself can be significantly embrittled by hydrogen [65].

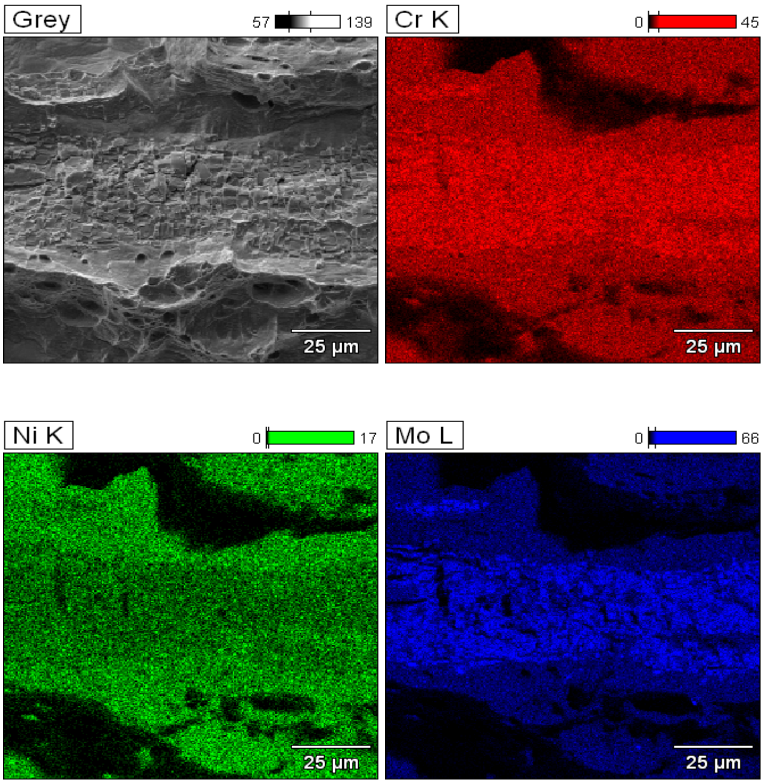

Fig. 5- 19 XEDS mapping on heavily cracked region

From these two mapping result, it is tentative to conclude the different fracture feature can be owing to the different elemental segregations and thus further different phases. Macro segregation in 316L stainless steel has been counted for the high degree of variability in H_2 cracking resistance for different batches of 316L stainless steel [49].

OIM is utilized trying to figure out the phase and orientations of these brittle featured regions. It is well known the slip system in FCC structure makes cleavage failure nearly impossible. Only few cleavage failures were observed in FCC system. The most extensively studied FCC system failed in cleavage style is Ir. The calculation and experimental results both confirms that the cleavage system is (100) [001] [66].

Due to the rough fracture surface, OIM results are only available in the similar fractured region elsewhere as illustrated in Fig. 5- 20. In Fig. 5- 20, only BCC in (001) orientation was detected. Combined with element segregation information obtained from previous result, it supports the segregated area is essentially the delta ferrite, which is inhomogeneity formed during the metallurgical process.

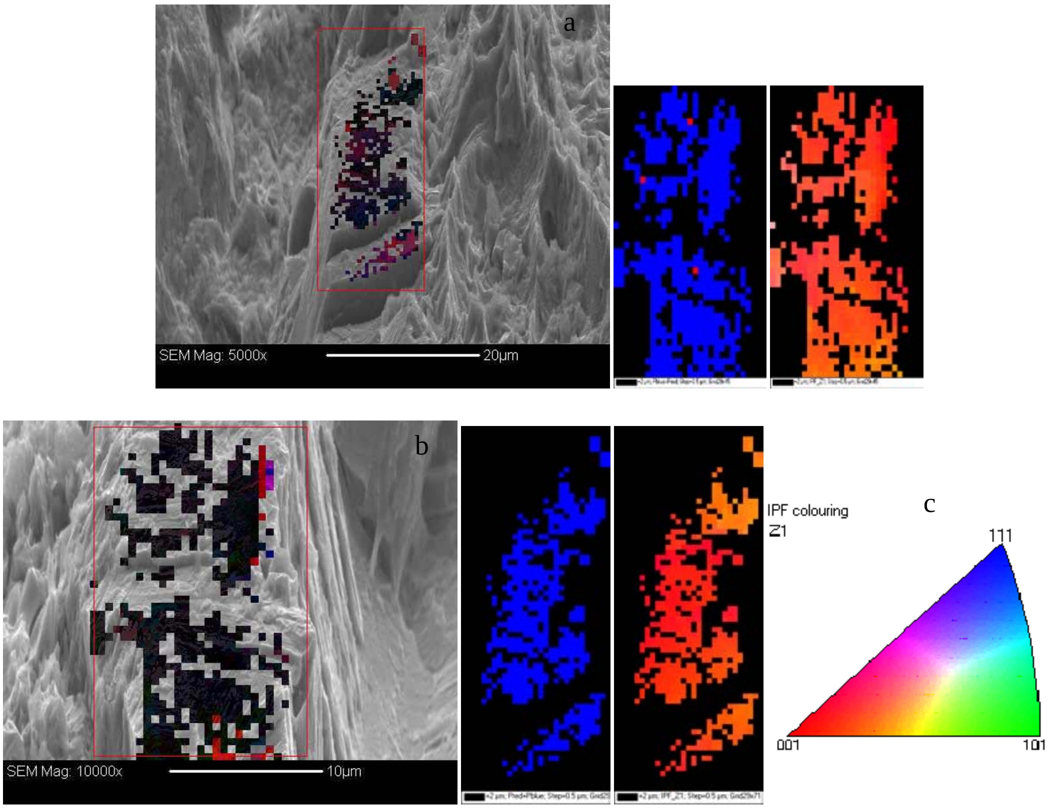

Fig. 5- 20 OIM results on two brittle featured fracture surface. (a) OIM region on the fracture surface, phase mapping and orientation mapping, (b)another OIM region and (c) Inverse Polar Figure (IPF) colouring

Conclusion

Constant load and wedge test are done on the hydrogen-charged 316L stainless steel with sharp pre-crack in it. Hydrogen induced cracking was observed in the carburized sample, whereas no cracking happened in the non-carburized sample. The cracking is due to the extremely high strength of the carburized surface. The actual stress intensity in the case, which is much higher than the nominally applied stress intensity, is predicted by crack tip opening displacement model. The threshold of the very surface is calculated according to bridging model and weight function, which is around 40 MPa√m. Demonstrated by FIB cross-sections, the cracks in the carburized sample are all within the carburized layer and tend to be shallower towards the newly extended crack tip. The inverse relationship between the yield strength (corresponding case depth) and threshold value still maintains according to the calculation result.

Plastic zone evolution investigation reveals the enhanced dislocation mobility within the plastic zone in the hydrogen-charged samples. The carburized layer is demonstrated to be very efficient to suppress the plastic zone size due to the high strength of the case. Microvoid coalescence mode dominates the fracture surface. Brittle-featured facet is confirmed as delta-ferrite on (001) orientation.

The significance of this study is that the extremely high strength carburized surface is susceptible to gaseous hydrogen. Consequently a partial carburization that brings strength up to an appropriate level may be a better choice for hydrogen storage application.

Appendix Ⅰ

Though the hydrogen can embrittle the case is an undeniable fact, still, the effect of case on the hydrogen diffusion during the charging process is not clearly known. Appendix will try to address this.

Under normal condition, where only hydrogen acts as interstitial atoms, hydrogen prefers the octahedral sites, because of its larger size. When samples go through carburization process first, carbon atoms will take the octahedral sites first. The achieved carbon atomic percent is usually around 12. Considering there are four atoms and four octahedral sites per FCC unit cell, 12 at% carbon can be treated as one carbon atom at interstitial every two unit cell. This ensures the strain introduced by carbon still be local. The assumption that no interaction between carbon introduced strain is reasonable. When hydrogen is introduced, there are still plenty of interstitial sites for hydrogen to freely jump. Moreover, the overall lattice expansion after carburization is well accepted. The lattice expansion brings down the energy barrier of each jump to squeeze through the lattice thus further facilitates the diffusion of hydrogen. From another perspective, there is high concentration-dependent diffusion for hydrogen, just like carbon and nitrogen diffusion [68]. The high concentration-dependent diffusion is due to the expansion introduced by the preceding carbon or nitrogen. If this is true, the preceding carbon in the sample should promote the afterwards hydrogen diffusion in the same way.

On the other hand, all the previous discussion is based on the perfect lattice and diffusion itself is on the ground of lattice diffusion. The reality after carburization is massive dislocations are introduced into the case. The trapping of hydrogen by dislocation [69] during the hydrogen-charging process must be considered. There are deep traps (~1.2 eV) and reversible traps (~0.5 eV) in the sample. The hydrogen atoms in reversible traps are in local equilibrium with mobile hydrogen atoms. But the hydrogen atoms in deep traps are practically frozen. These deep traps will be saturated with the captured hydrogen. After the saturation, there is no further inhibition for hydrogen diffusion.

So what most possibly happens during the hydrogen-charging process is as follows. In the initial hydrogen-charging stage, hydrogen diffusion will be inhibited by the traps formed due to the previous massive carbon injection. However, when traps are saturated, carburized case will facilitate the hydrogen diffusion.

Appendix Ⅱ

Fatigue crack growth rate (FCGR) tests were done on the horizontal machine under the condition of constant load and 0.5 Hz in 0.6 M NaCl solution. The loading ration (R) is 0.2, where R is the minimum stress over maximum stress during a loading cycle. Six samples went through from one time to six times of carburization process were tested respectively, named as CT1 to CT6. Data is acquired by software Automated Fatigue Crack Growth 2001 series and further processed by the Automated Fatigue Crack Growth Analysis. The plot of delta stress intensity versus FCGR is shown in figure below.

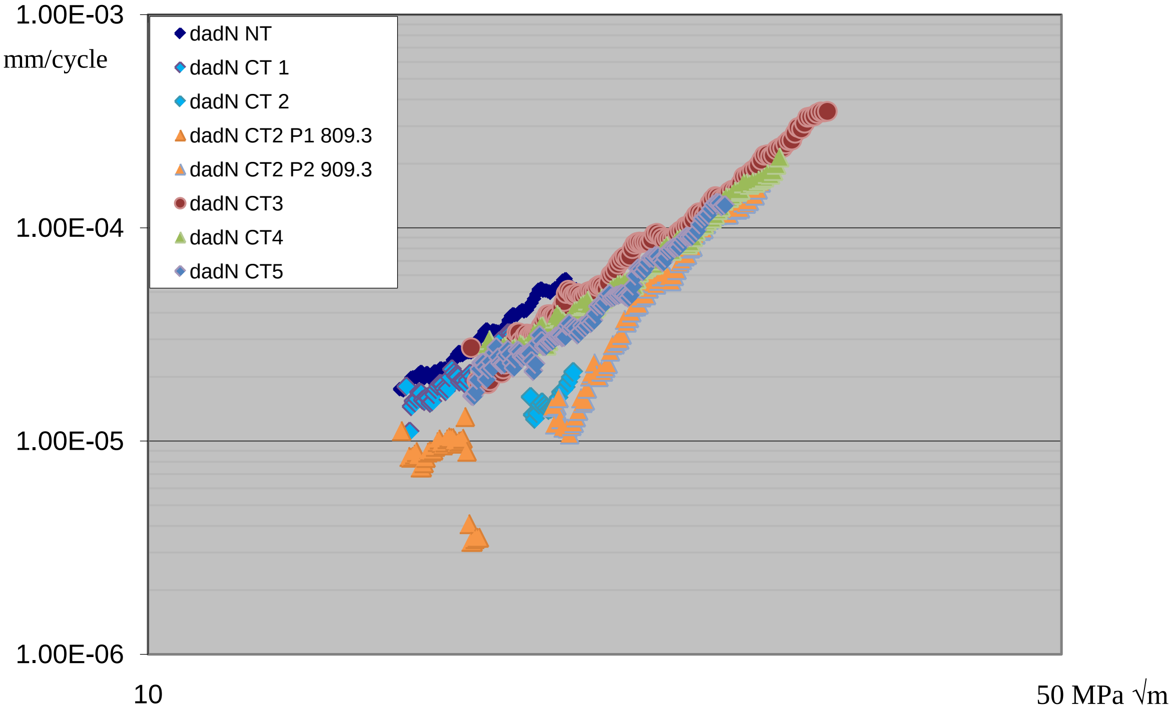

Fig. A II- 1 FCGR curve of NT and multiple carburized samples

The tests of NT, CT1 P1/P2 and CT2 P1 are done under the load of 809 lb. But the FCGR for CT1 and CT2 drops too low and thus use the load of 909 lb instead afterwards. The FCGR of NT is in the low stress intensity range and the highest growth rate is achieved compared with other carburized samples. All the FCGR data from carburized samples are lower than the NT one, indicating the interstitial carbon hardened layer can suppress the crack growth. However, the effect of successive carburization is not straightforward. From the plot, in the low delta stress intensity range, the FCGR of CT1, CT2 and CT6 are the slowest. FCGR of other carburized samples are in the between of the NT and slowest samples. Therefore, there is no obvious relationship between the carburization times and FCGR reduction.

In the high delta stress intensity range, all the six FCGR curves converge. This implies the beneficial effect of carburization is negligible when applied stress intensity is high. It can be ascribed to the fraction of carburized layer is small compared with bulk material. So when the stress intensity is high, the bulk material dominates the fatigue crack growth behavior.

For sample CT1 and CT2, there are big FCGR drops in the curve. Taking sample CT1 as an example, the FCGR plunge as shown by red data point in the Fig. A II- 2 below. From the surface observation, the crack at the corresponding data points shows serious crack branching, which can be a reason for this FCGR retardation. Actually, the crack deflection and bifurcation can significantly reduce the effective stress intensity at the crack tip and thus can cause crack retardation or even arrest [70]. The picture (Fig. A II- 3) taken shows that main crack branches into several parts. This can shield the effective stress intensity at crack tip substantially and thus cause the observed shape reduction of FCGR.

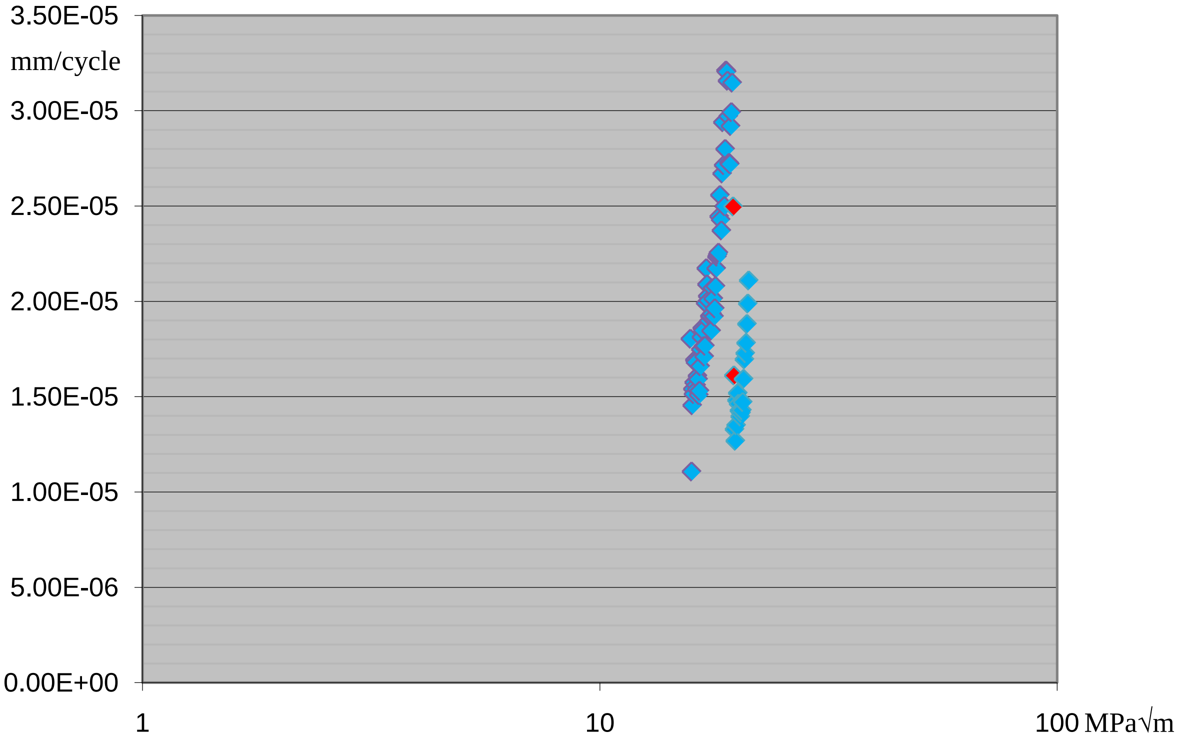

Fig. A II- 2 FCGR curve of one-time carburized sample

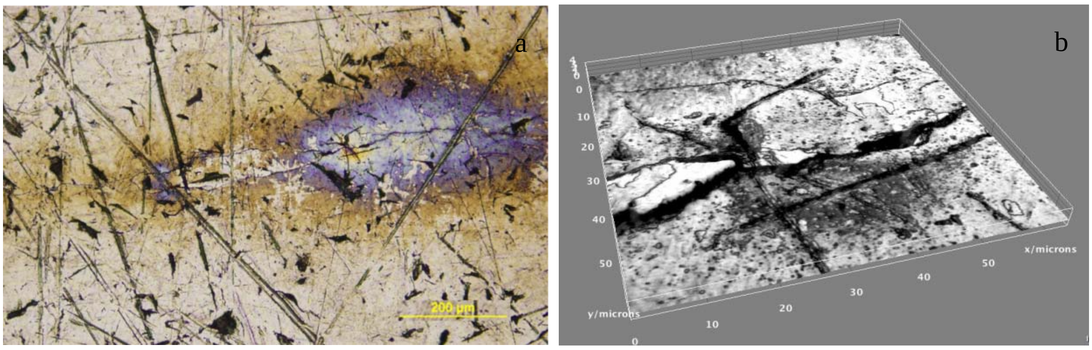

Fig. A II- 3 Crack branching of one-time carburized sample (a) and 3D image of the branching position

Another feature on the sample surface is that there is some colored region along the crack observed by the confocal microscope. This colored region is much wider along the crack on the carburized sample than that on the non-treated sample with the same exposure period in the solution, as illustrated in the Fig. A II- 4. The different color can be due to the different thin film thickness. The composition of the thin film can be studied by XPS. The result (Fig. A II- 5) indicates it is mainly the iron oxide. However, this iron oxide is pretty similar to the rust and not protective. The depth of this thin film is around 150 nm. This indicates the carburized sample surface is possibly more susceptible to the corrosion environment.

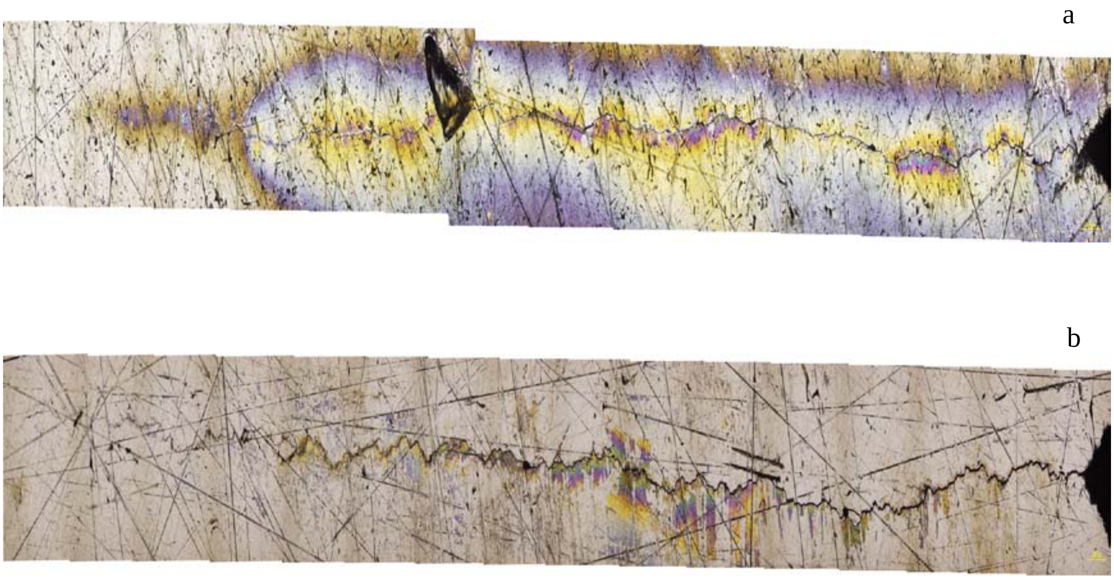

Fig. A II- 4 Total crack length of NT (a) and one-time carburized (b) samples

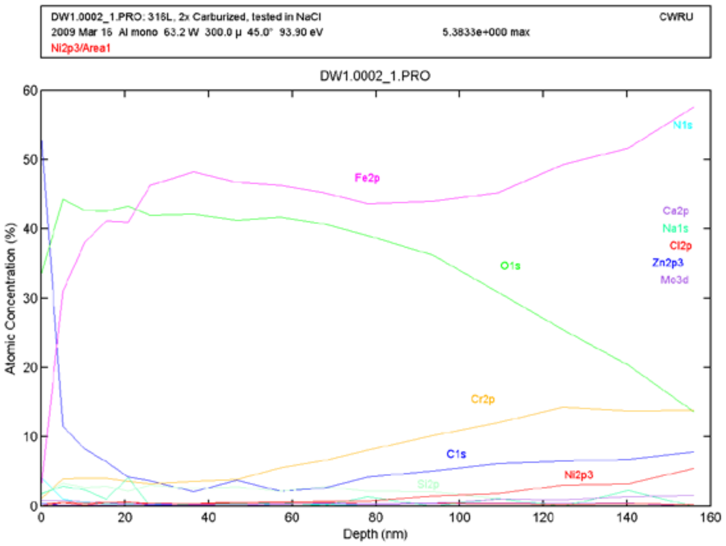

Fig. A II- 5 XPS result of colored thin film along the crack of one-time carburized sample

Fractography study of the corrosion fatigue test sample shows there is no difference between the case and bulk material (Fig. A II- 6 (a)). And the transgranular cleavage dominates the fracture surface. On the fracture surface, secondary cracks can also be identified.

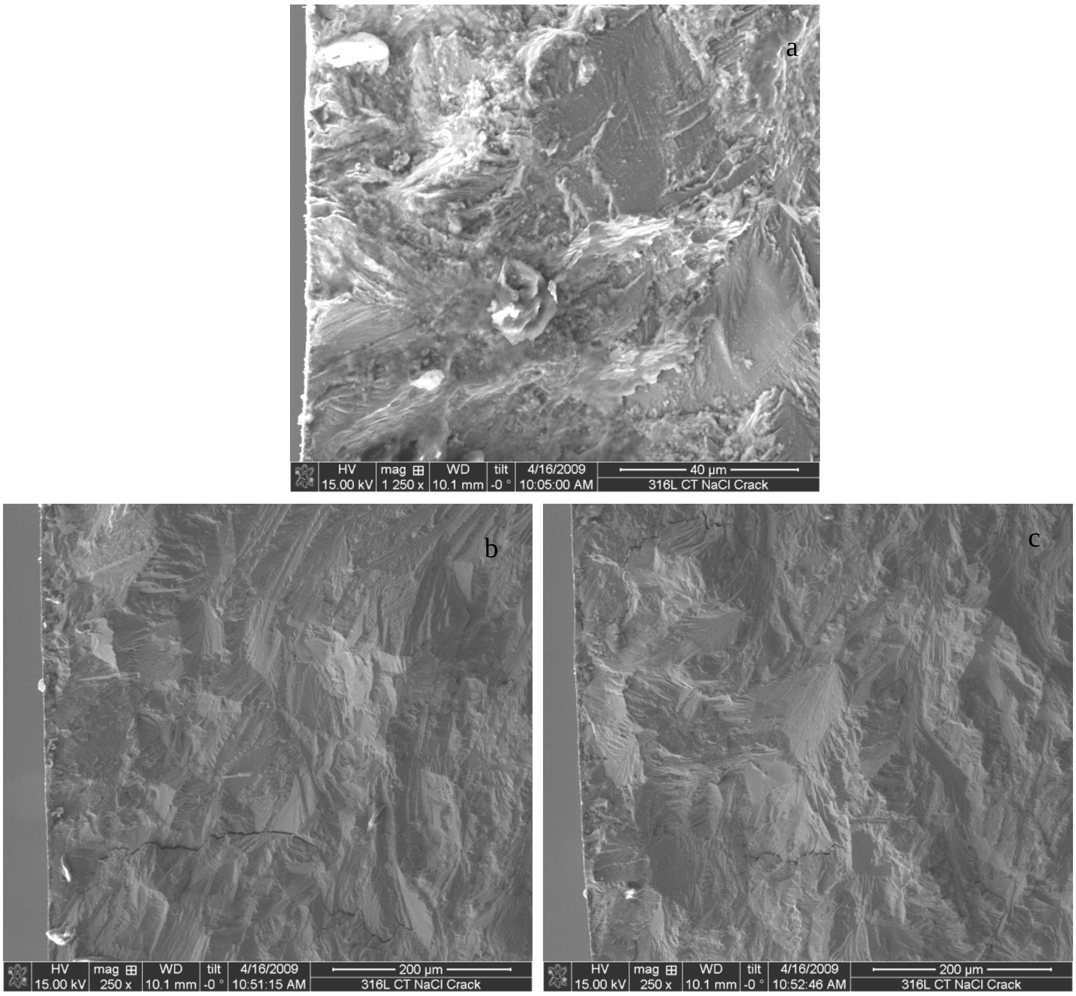

Fig. A II- 6 Fractography of one-time carburized sample (a) and secondary crack on the fracture surface (b) and (c)

Appendix Ⅲ

Multiple Carburized sample Characterization

Multiple carburization process was done on the 316L stainless steel. The same samples used in the corrosion fatigue tests as CT1, CT2, CT4, CT5 and CT6 were characterized in this part.

The case depths were exposed by the metallographic work and the hardness profiles were achieved by the Agilent nano-indenter. All the figures acquired for the samples are the overlay of hardness profile with metallography work. The etchant utilized is $HCl:HNO_3:H_2O=2:1:1$.

Figures listed below from Fig. A III- 1 to Fig. A III- 5 are the results from sample CT1, CT2, CT4, CT5 and CT6. The revealed case depth and highest hardness for each sample is summarized in Table A III- 1.

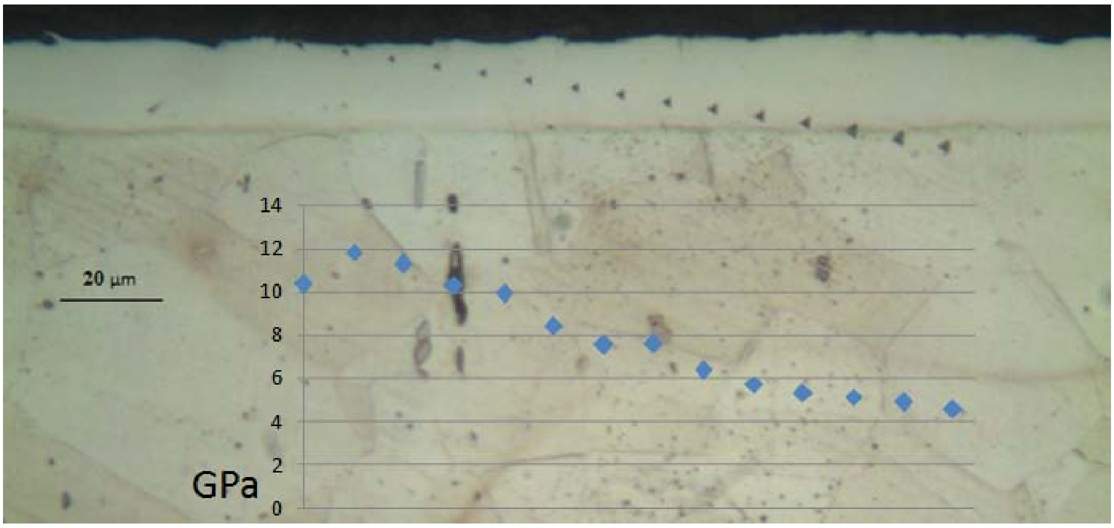

Fig. A III- 1 Metallography work and hardness profile on sample CT1

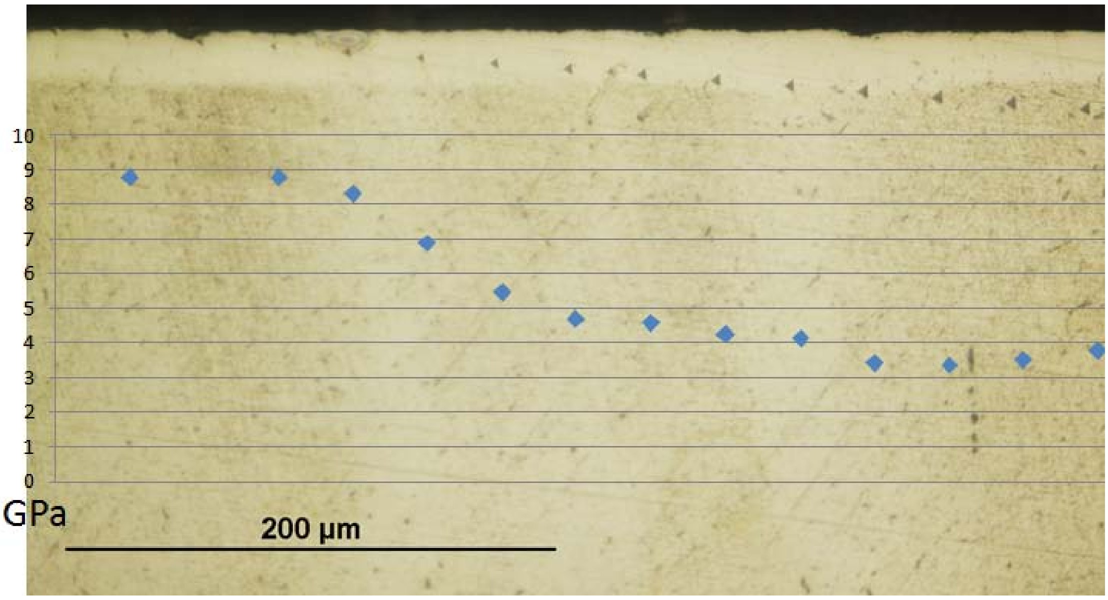

Fig. A III- 2 Metallography work and hardness profile on sample CT2.

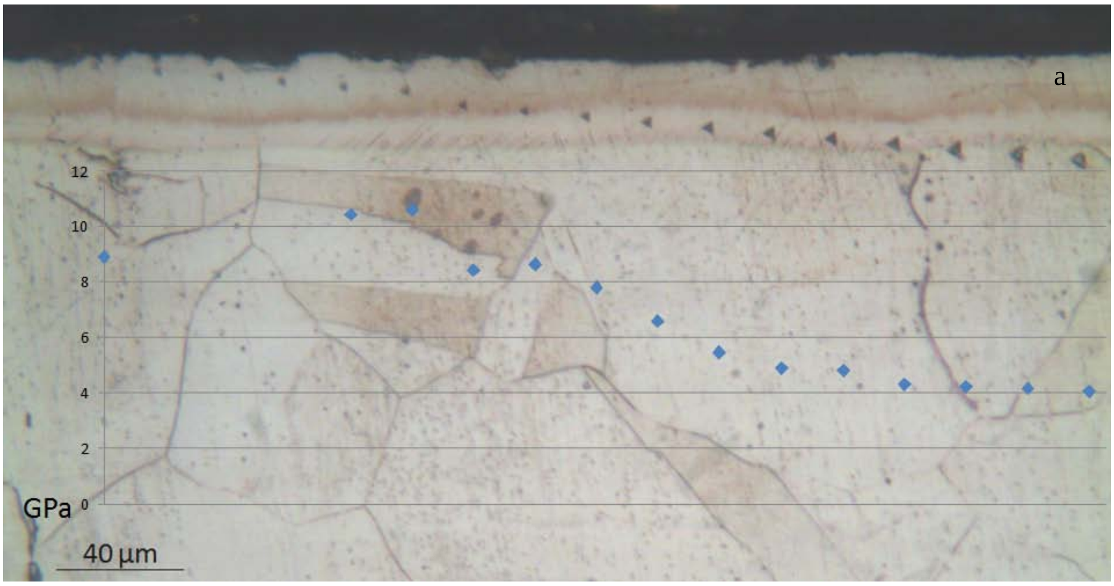

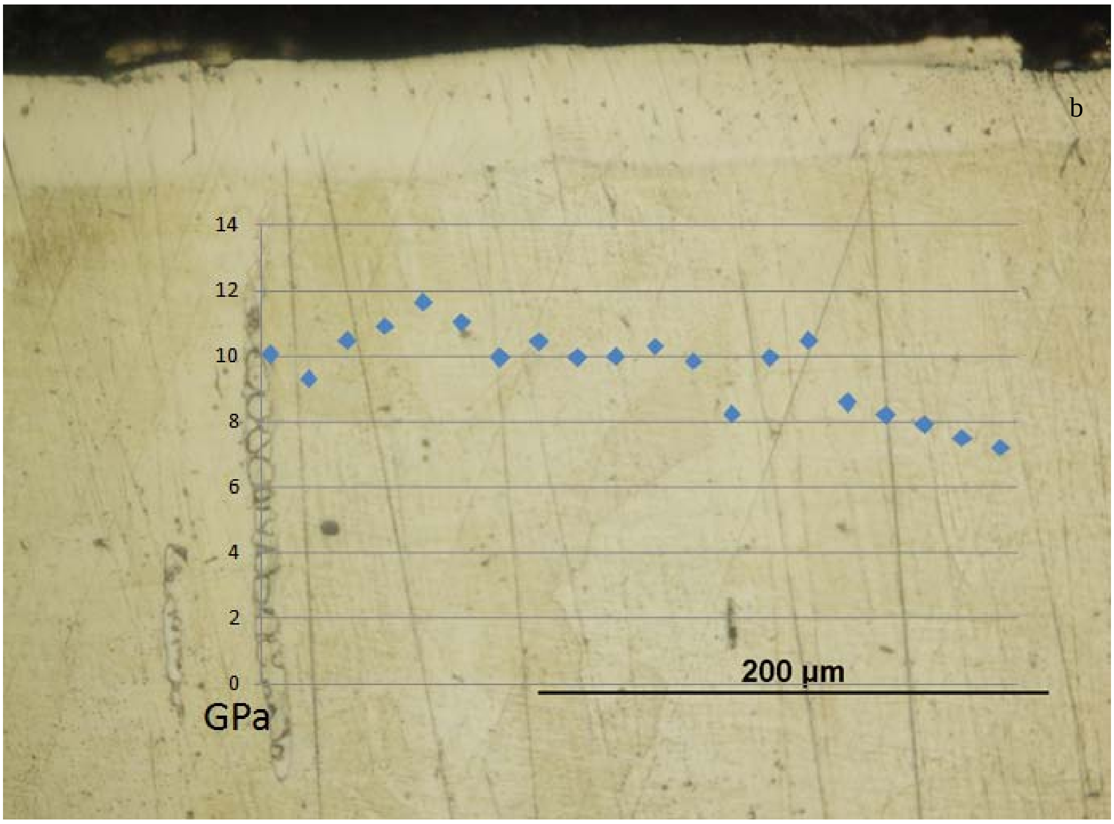

Fig. A III- 3 (a) Metallography work and hardness profile on sample CT4 and (b) CT4 with a thicker case.

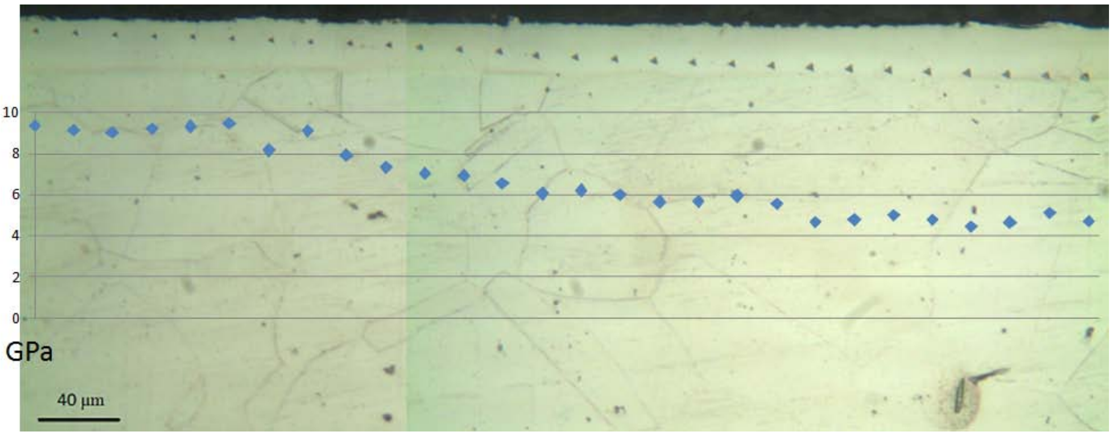

Fig. A III- 4 Metallography work and hardness profile on sample CT5.

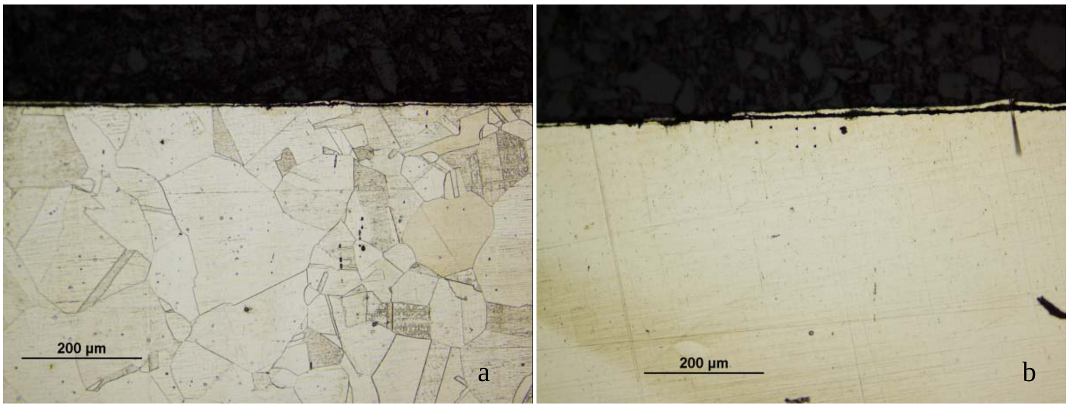

Fig. A III- 5 Metallography work and hardness profile on sample CT6 (a) is etched sample and (b) is hardness indents.

Table A III- 1 Case depth and hardness summary for multiple carburized samples

Sample	Case depth (μm)	Surface hardness (GPa)
CT1	20	12
CT2	25	9
CT4	30 (45)	10.5 (12)
CT5	30	10

The observed case depths for multiple carburized samples become thicker as more times of carburization process went through. The case depth increases from 20 μm for one time carburized sample to 30 μm for five times carburized sample as shown in the table. However, the case thickness did not follow the square root of time as rule of thumb in diffusion. The hardness profiles achieved on these samples suggest the surface hardness cannot be improved by successive carburization process. The hardness values obtained from carburized samples are all around 10 GPa, indicating the surface hardness is limited by the solute carbon atoms content.

It should be noted that a case depth around 45 μm was once observed on sample CT4 as shown in Fig. A III- 3 (b) which is comparable to the result previous investigated by our group [9]. 45μm deep case also gives a decent surface hardness which is around 12 GPa. However, the same feature was missing after further polishing. Only a case depth about 30 μm could be seen and the surface hardness also decreases to 10.5 GPa. These results on sample CT4 indicate the thickness of case is not uniform on the sample CT4. Moreover, the case depth found on sample CT5 is only around 30 μm indicating no further improvement compared to sample CT4. There is no case unveiled on the sample CT6, which is also surprising. The hardness near the edge of the sample is 3.25 GPa, nominally same to the bulk material hardness.

XRD results are also available on these samples shown in Fig. A III- 6 below and the lattice expansion was obtained from the XRD patterns and summarized in Table A III- 2. The patterns of NT and CT are adopted from previous study. The lattice expansion actually increases with successive carburization except the case of CT5 whose lattice expansion is actually less than CT2. XRD pattern of sample CT6 also suggests there is no hardened case in it. The possible explanation for the absence of case observation on CT6 is that the sample is mislabeled.

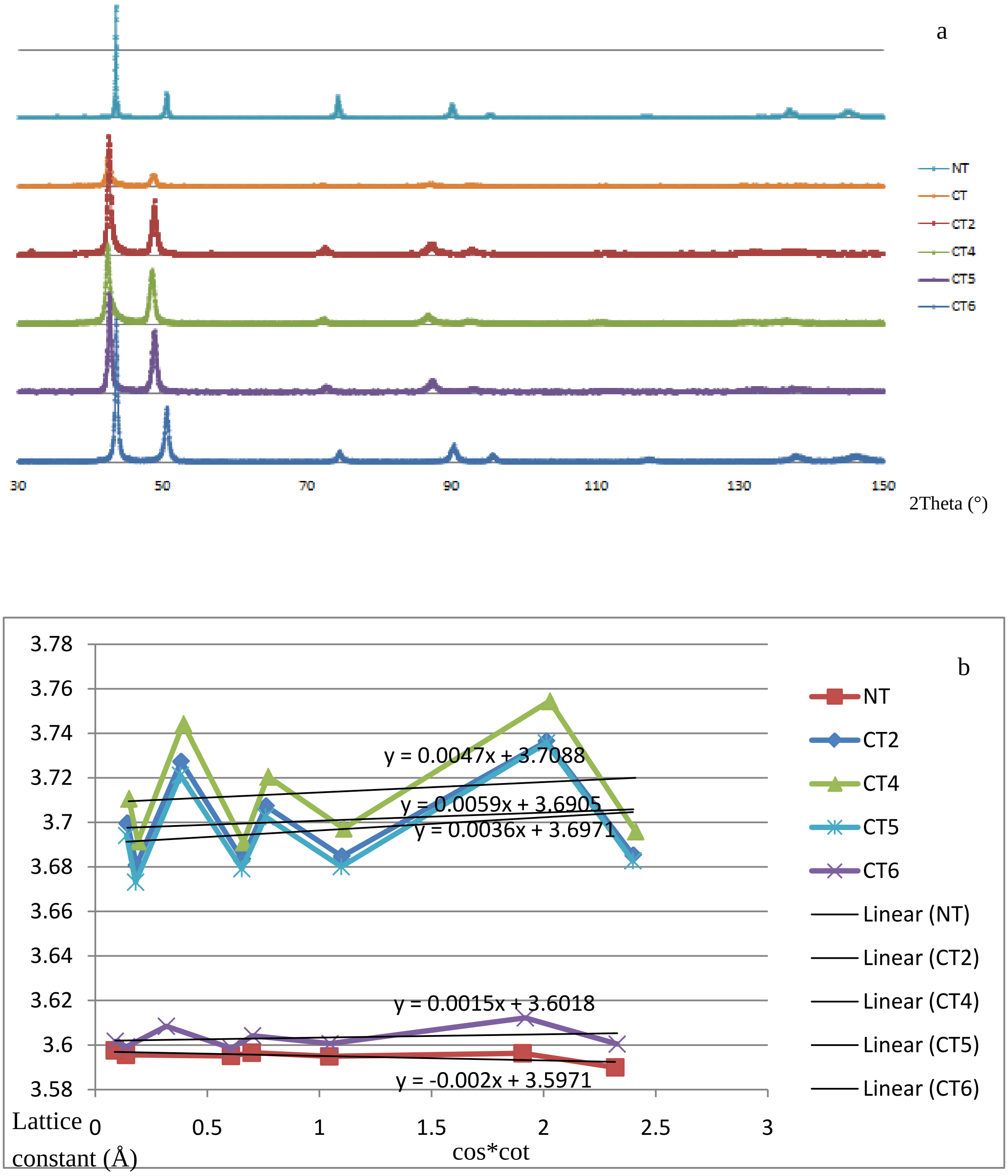

Fig. A III- 6 NT and multiple carburized samples (a) is XRD patterns and (b) is lattice constant calculation.

Table A III- 2 Lattice constant and expansion

	Lattice constant (Å)	Lattice expansion (%)
NT	3.597	
CT2	3.697	2.78
CT4	3.709	3.11
CT5	3.691	2.60
CT6	3.608	0.13

The characterization suggests the successive carburization can increase the interstitial carbon hardened case thickness and expand the lattice further but not necessarily proportionally related to the carburization times. However, the surface hardness stays roughly the same despite of the successive carburization.

Appendix IV

Residual stress estimation on both H-charged and carburized 316L stainless steel

Based on the HELP theory and test result on plastic zone evolution, the hydrogen atoms can actually unpin dislocations from obstacles and increase their mobility. However, this actually goes against the bases of carburization process. Due to the huge amount of interstitial carbon atoms, the dislocations in the hardened case are immobile and this gives rise to the high hardness and residual stress in the layer. Therefore, if the hydrogen atoms activate the dislocation motion, the residual stress decreasing can be expected. Sample H6, which is hydrogen charged after carburization, was used in this study.

The residual stress is determined by the standard XRD $\sin^2\psi$ technique [71].

$$\sigma = \frac{E}{(1+\nu)sin^2\psi}\left(\frac{d_i - d_n}{d_n}\right) = \frac{E}{(1+\nu)sin^2\psi}\left(\frac{a_i - a_n}{a_n}\right) \quad (1)$$

σ, denotes the residual stress; E, Young's modulus; ν, Poisson ratio; ψ, various tilt angles; d_i, lattice spacing of a particular hkl plane at various tilt angles; d_n, lattice spacing of the same hkl plane at ψ=0. And the lattice parameters attained from d_i and d_n are a_i and a_n.

The original XRD patterns are shown in Fig. A IV- 1 original XRD patterns for the (420) peak of sample H6 below.

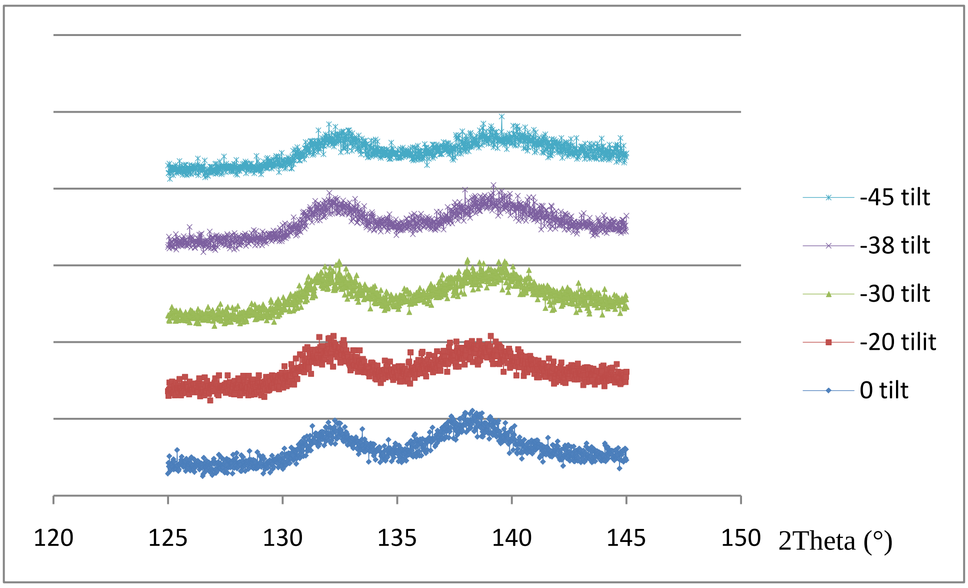

Fig. A IV- 1 original XRD patterns for the (420) peak of sample H6

According to De Wit's study on the diffraction elastic constants of cubic polycrystal, [72] the ν and E parameters can be represented.

$$G=\frac{E}{1+\nu} \tag{2}$$

by the effective shear modulus of the effective medium, G, as shown in equation 2. The value for G is equal to 1/S2, where S2 is the second diffraction elastic constant. Therefore, the residual stress can be given by

$$\sigma=\frac{slope}{intercept} * \frac{2}{S2_{hkl}} \tag{3}$$

where slope is defined by $\frac{d_i-d_n}{sin^2\psi}$; intercept is d_n. Fig. A IV- 2, shows the calculated residual stress in hydrogen-charged and carburized 316L sample H6.

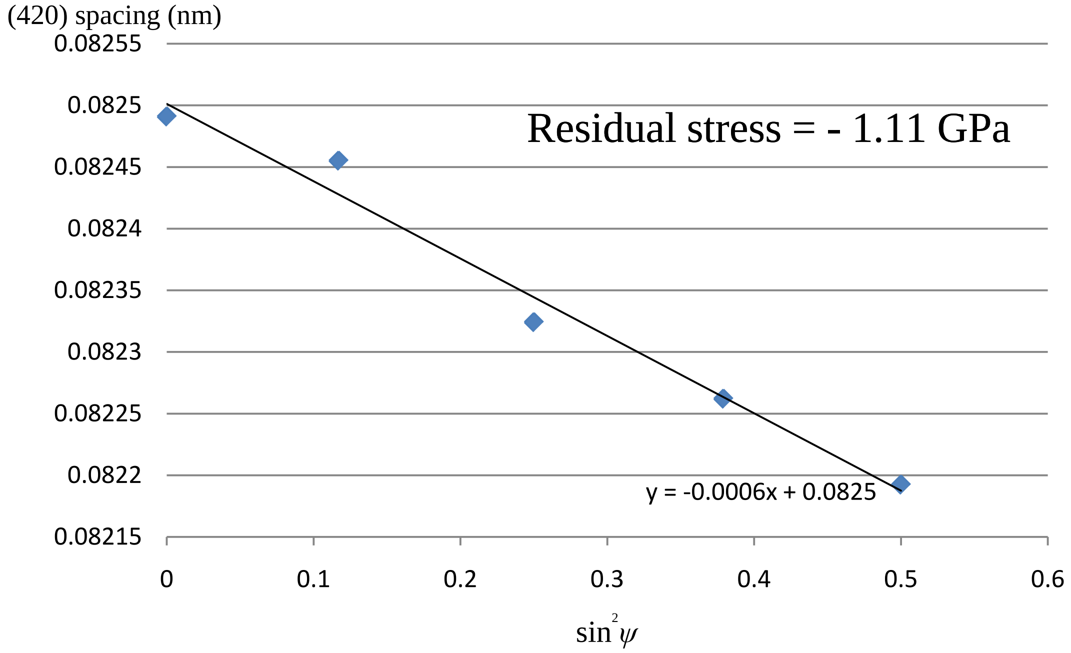

Fig. A IV- 2 XRD lattice parameters for the (420) peak of hydrogen-charged and carburized 316L as a function of $\sin^2\psi$

According to Kroner's original cubic equation for the effective shear stress modulus of cubic polycrystal

$$G^3-\alpha G^2-\beta G-\gamma=0 \tag{4}$$

where $\alpha=\alpha_2-\alpha_1$, $\beta=\beta_2-\beta_1$

and α_1, α_2, β_1, β_2, γ are given by De Wit [72] as follows:

$\alpha_1=\frac{3}{8}\{3\kappa+4[\mu''+3(\mu'-\mu'')]\Gamma$

$\alpha_2=\frac{1}{5}(2\,\mu'+3\,\mu'')$

$\beta_1=\frac{3}{4}\kappa[\mu''+3(\mu'-\mu'')\Gamma]$

$\beta_2=\frac{3}{40}(6\kappa\mu'+9\kappa\mu''+20\mu'\mu'')$

$\gamma=\frac{3}{4}\kappa\mu'\mu''$

Γ was introduced to describe the diffraction effects of a cubic polycrystal and given by

$\Gamma=(h^2k^2+k^2l^2+l^2h^2)/(h^2+k^2+l^2)$

and the cubic bulk modulus and shear moduli are

$$\kappa = \frac{1}{3}(c_{11} + 2c_{12})$$

$$\mu' = \frac{1}{2}(c_{11} - c_{12})$$

$$\mu'' = c_{44}$$

The XRD result suggests the residual compressive stress on the sample H6 surface is 1.11 GPa, which is only half of that on the carburized sample. This supports the HELP theory and confirms the hydrogen atoms can mobilize the dislocation from the obstacles and thus easier to flow under stress.

In order to confirm the compressive residual stress in one time carburized sample, the same procedure is employed to determine the residual stress in CT1. The original XRD patterns and calculated compressive residual stress result on (420) plane is shown in the Fig. A IV- 3. The calculation indicates the residual stress in the sample CT1 is around -2.5 GPa, which is even higher than the value reported by our group previouslys. Therefore, the lower residual stress level observed on sample H6 can be due to the presence of hydrogen.

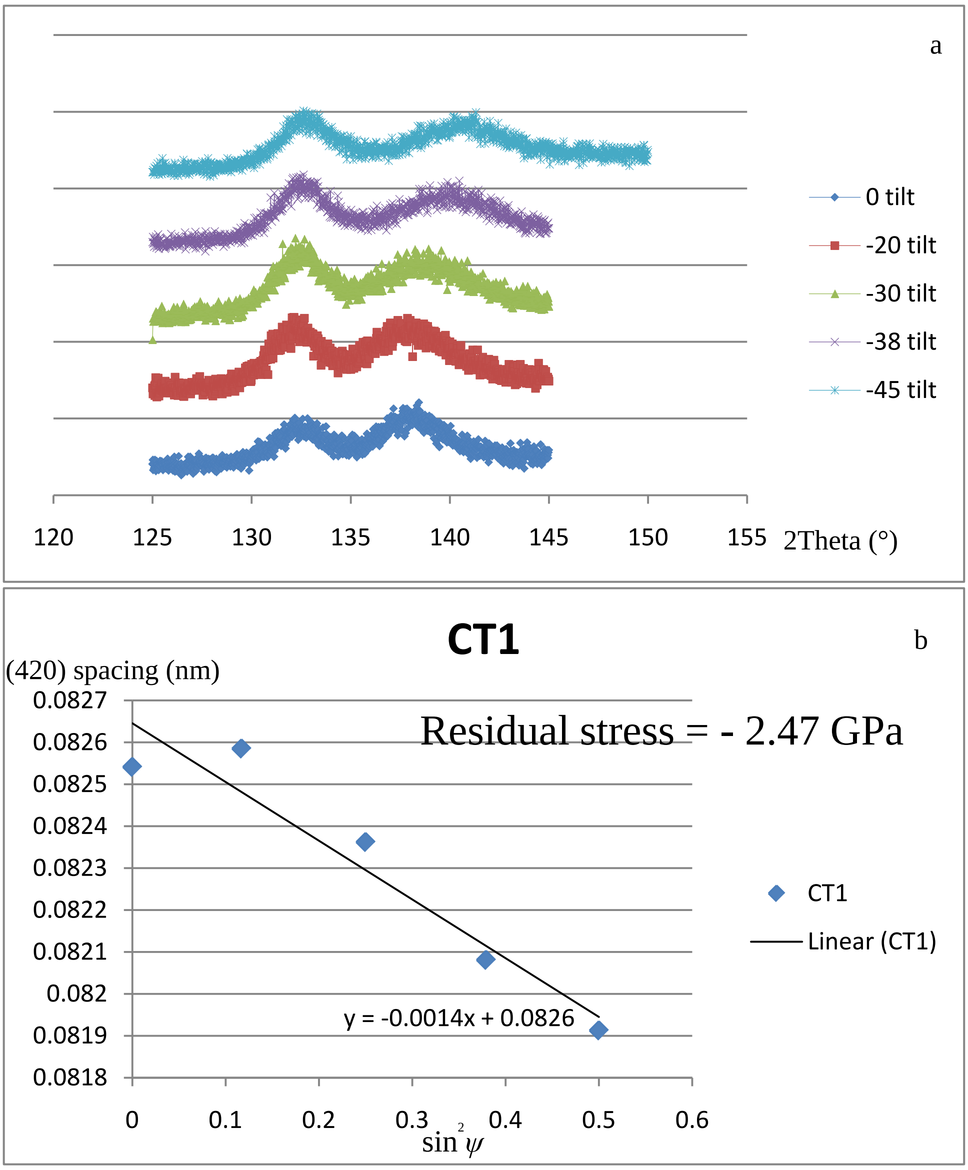

Fig. A IV- 3 (a) original XRD patterns for the (420) peak of sample CT and (b) XRD lattice parameters for the (420) peak of carburized 316L as a function of sin$^2\psi$

Future Work

1. To study the brittle-like fracture facet at the interface between the pre-crack and tensile region. It is a possible FCC brittle failure spot.
2. To study the possible elemental-segregation-induced FCC brittle failure.
3. To study the hydrogen diffusion and interaction with carbon in the hardened case.
4. To study the effect of carburization on the cathodic-charged hydrogen-induced embrittlement.
5. To study the possible benefits of partial carburization process on the hydrogen-induced cracking behavior.
6. To study the effect of successful carburization on the alloy inherent susceptible to the hydrogen.

Bibliography

1 C Borchers, T Michler, T Pundt, Effect of Hydrogen on the Mechanical Properties of Stainless Steels, Advanced Engineering Materials, 2008

2 J Watson, Y Shen, M Meshii, Effect of Cathodic Charging on the Mechanical Properties of Aluminum, Metallurgical Transactions A, 1988

3 C Briant, Z Wang, N Chollocoop, Hydrogen embrittlement of commercial purity titanium, Corrosion Science, 2002

4 N Bandyopadhyay, J Kameda, C McMahon Jr. Hydorgen-Induced Cracking in 4340-Type Steel: Effects of Composition, Yield Strength and H_2 Pressure, Metallurgical Transactions A, 1983

5 W Maeng, M Kim, Comparative study on the fatigue crack growth behavior of 316L and 316LN stainless steels: effect of microstructure of cyclic plastc strain zone at crack tip, Journal of Nuclear materials, 2000

6 Stainless steel handbook, 1959

7 George Dieter. “Mechanical Metallurgy”, SI metric edition

8 Y. Murakami. “Stress intensity factor handbook”, pp.24

9 N Agarwal, H Kahn, A Avishai, G Michal, F Ernst, A Heuer, Enhanced fatigue resistance in 316L austenitic stainless steel due to low-temperature paraequilibrium carburization, Acta Materialia, 2007

10 Fracture mechanics: fundamentals and applications, T. L. Anderson

11 A Saxena, S Hudak, Review and extension of compliance information, International Journal of Fracture， 1978

12 H Bueckner, A novel principle for the computation of stress intensity factors, Journal of Applied Mathematics and Mechanics, 1970

13 J Rice Some remarks on elastic crack tip stress fields, International Journal of Solids and Structures, 1972

14 T Fett, D Munz, Stress intensity factors and weight functions

15 D Nelson, Effects of residual stress on fatigue crack propagation, Residual stress effects in fatigue, ASTM STP 776, American Society for Testing and Materials, 1982

16 C Kim, D Diesburg, G Eldis, Effect of residual stress on fatigue fracture of case-hardened steels – an analytical model, Residual stress effects in fatigue, ASTM STP 776, American Society for Testing and Materials, 1982

17 S Collins, P Williams, Low temperature colossal supersaturation, Advanced Materials & Processes, 2006

18 Y Cao, F Ernst and G Michal, Colossal carbon supersaturation in austenitic stainless steels carburized at low temperature, Acta Materialia, 2003

19 G Michal, F Ernst, H Kahn, Y Cao, F Oba, N Agarwal and A Heuer. Carbon supersaturation due to paraequilibrium carburization: stainless steels with greatly improved mechanical properties, Acta Materialia, 2006

20 F Martin, P Natishan, E Lemieux, T Newbauer, R Rayne, R Bayles, H Kahn, G Michal, F Ernst and A Heuer. Enhanced corrosion resistance of stainless steel carburized at low temperature, Metallurgical and Materials transactions A, 2009

21 P Hsu, Master thesis, 2008

22 Lucas O’donnell, Master thesis, 2010

23 T Michler, J Naumann, Hydrogen environment embrittlement of austenitic stainless steel at low temperatures, International Journal of Hydrogen Energy, 2008

24 D Delafosse, T Magnin, Hydrogen induced plasticity in stress corrosion cracking of engineering systems, Engineering Fracture Mechanics, 2001

25 F Zucchi, V Grassi, C Monticelli, G Trabanelli, Hydrogen embrittlement of duplex stainless steel under cathodic protection in acidic artificial sea water in the presence of sulphide ions, Corrosion Science, 2006

26 T Zackroczymski, A Glowacka, W Swiatnicki, Effect of hydrogen concentration on the embrittlement of a duplex stainless steel, Corrosion Science, 2005

27 C San Marchi, B Somerday, X Tang, G Schiroky, Effects of alloy composition and strain hardening on tensile fracture of hydrogen-precharged type 316 stainless steel, International Journal of Hydrogen Energy, 2008

28 E Herms, J Olive, M Puiggali, Hydrogen embrittlement of 316L type stainless steel, Material Science & Engineering A, 1999

29 V Olden, C Thaulow, R Johnson, Modelling of hydrogen diffusion and hydrogen induced cracking in supermartensitic and duplex stainless steel Material and Design, 2008

30 J Toribio, Hydrogen-plasticity interactions in pearlite steel: a fractographic and numerical study, Material Science & Engineering A, 1996

31 R Swanson, A Thompson, I Bernstain, Effect of notch root radius on stress intensity in mode Ⅰ and mode Ⅲ loading, Metallurgical and Materials Transactions A, 1986

32 A West and M Louthan Jr., Dislocation transport and hydrogen embrittlement, Metallurgical Transactions A, 1979

33 A Brass, J Chene, Hydrogen uptake in 316L stainless steel: consequences on the tensile properties, Corrosion Science, 2006

34 A Valiente, L Caballero, J Ruiz, Hydrogen assisted failure of precracked specimens of 316L stainless steel, Nuclear Engineering and Design, 1999

35 C San Marchi, B Somerday, S Robinson, Permeability, solubility and diffusivity of hydrogen isotopes in stainless steel at high gas pressure, International Journal of Hydrogen Energy, 2008

36 P Rozenak, L Zevin, D Eliezer, Hydrogen effect on phase transformations in austenitic stainless steel, Journal of Materials Science, 1984

37 A Bentley, G Smith, Phase transformation of austenitic stainless steel as a result of cathodic hydrogen charging, Metallurgical Transactions A, 1986

38 N Narita, C Altstetter, H Birnbaum, Hydrogen-related phase transformations in austenitic stainless steel, Metallurgical Transactions A, 1982

39 Q Yang, L Qiao, S Chiovelli, J Luo, Critical hydrogen charging conditions for matensite transformation and surface cracking in type 304 stainless steel, Scripta Materilia, 1999

40 M Hoelzel, S Danilkin, H Ehrenberg, D Toebbens, T Udovic, H Fuess, H Wipf, Effect of high-pressure hydrogen charging on the structure of austenitic stainless steels, Material Science & Engineering A, 2004

41 K Nibur, D Bahr, B Somerday, Hydrogen effect on dislocation activity in austenitic stainless steel, Acta Materilia, 2006

42 P Ferreira, I Robertson, H Birnbaum, Hydrogen effects on the interaction between dislocations, Acta Materilia, 1998

43 A Barnoush, H Vehoff, In situ electrochemical nanoindentation: a technique for local examination of hydrogen embrittlement, Corrosion Science, 2008

44 D Abraham, C Altstteter, Hydrogen-enhanced localization of plasticity in an austenitic stainless steel, Metallurgical and Materials Transactions A, 1995

45 Y Katz, N Tymiak, W Gerberich, Nanomechanical probes as new approaches to hydrogen/deformation interaction studies, Engineering Fracture Mechanics, 2001

46 P Ferreira, I Robertson, H Birnbaum, Hydrogen effect on the character of dislocations in high-purity aluminum, Acta Materilia, 1999

47 Y Mine, C Narazaki, K Murakami, S Matsuoka, Y Murakami, Hydrogen transport in solution-treated and pre-strained austenitic stainless steels and its role in hydrogen-enhanced fatigue crack growth, International Journal of Hydrogen Energy, 2009

48 G Caskey Jr., Hydrogen damage in stainless steels. Environmental degradation of engineering materials in hydrogen 1981

49 T Michler, Y Lee, R Gangloff, J Naumann, Influence of macro segregation on hydrogen environment embrittlement of SUS 316L stainless steel, International Journal of Hydrogen Energy, 2009

50 T Perng, C Altstetter, Comparison of hydrogen gas embrittlement of austenitic and ferritic stainless steel, Metallurgical Transactions A, 1987

51 R Gangloff, R Wei, Gaseous hydrogen embrittlement of high strength steels, Metallurgical Transactions A, 1977

52 W Gerberich, Y Chen, Hydrogen-controlled cracking – an new approach to threshold stress intensity, Metallurgical Transactions A, 1975

53 D Eliezer, A Arbel, P Rozenak, Hydrogen induced delay failure of AISI 316L and 321 types stainless steels, Journal of Materials Science Letters, 1983

54 R Stoltz, N Moody, M Perra, Microfracture model for hydrogen embrittlement of austenitic steels, Metallurgical Transactions A, 1983

55 W Dietzel, S Ghosal, Stress corrosion cracking – a new approach to testing methods, Materials Science, 1997

56 M Perra, Sustained load cracking of austenitic steels in gas hydrogen. In: MR Louthan, RP McNitt and RD Sisson, editors. Environmental Degradation of Engineering Materials in Hydrogen. Blacksburg VA: Laboratory for the study of Environmental Degradation of Engineering Materials, Virginia Polytechnic Instritute (1981) p. 321-333

57 R Stoltz, A West, Hydrogen assisted fracture in FCC metals and alloys. In: IM Bernstein and AW Thompson, editors. Proceedings of the International Conference on Effect of Hydrogen on Behavior of Materials: Hydrogen Effects in Metals, 1980, Moran WY. The metallurgical Society of AIME (1980) p.541-553

58 ASTM E647 1993

59 S Singh, C Altstetter, Effect of hydrogen concentration on slow crack growth in stainless steel, Metallurgical Transactions A, 1982

60 ASM Metals Handbook Vol. 12, Fractography

61 D Bloyer, K Venkateswara Rao and R Ritchie, Fracture toughness and R-curve behavior of laminated brittle-matrix composites, Metallurgical and Materials Transactions A,

62 K Hwu, B Derby, Fracture of metal/ceramic laminates - Ⅱ crack growth resistance and toughness, Acta Materilia, 1999

63 D Bloyer, K Venkateswara Rao and R Ritchie, Resistance-curve toughening in ductile/brittle layered structures: behavior in Nb/Nb_3Al laminates, Materials Science & Engineering A, 1996

64 T Angel, Formation of martensite in austenitic stainless steels, Journal iron and steel Inst, 1954

65 H Birnhaum, H Wadley, Hydrogen embrittlement of molybdenum, Scripta Metallurgica, 1975

66 S Hecker, D Rohr and E Stein, Metall. Trans. A, 1978

67 R Liu, N Narita, C Altstetter, H Birnbaum, E Pugh, Studies of the orientations of fracture surfaces produced in austenitic stainless steels by stress-corrosion cracking and hydrogen embrittlement, Metallurgical Transactions A, 1980

68 S Mandl, B Rauschenbach, Concentration dependent nitrogen diffusion coefficient in expanded austenite formed by ion implantation, Journal of Applied Physics, 2002

69 P Santos, W Jackson, Trap-limited hydrogen-diffusion in α-Si:H, Physical Review B, 1992

70 S Suresh, Crack Deflection: Implications for the Growth of Long and Short Fatigue Cracks, Metallurgical Transactions A, 1983

71 S. Kalnaus, Y. Jiang, Fatigue of AL6XN Stainless Steel, Journal of Engineering Materials and Technology 130(3) Article Number 031013 JULY 2008

72 R. DeWit, Diffraction elastic constants of a cubic polycrystal, Journal of Applied Crystallography 30: 510–511 AUG 1997